

THERMAL MODELING OF AN ION THRUSTER

by

Jonathan Lee Van Noord

A dissertation submitted in partial fulfillment
of the requirements for the degree of
Doctor of Philosophy
(Aerospace Engineering)
in The University of Michigan
1999

Doctoral Committee:

Associate Professor Alec D. Gallimore, Chair
Professor William J. Anderson
Associate Professor James P. Holloway
Professor Yue Ying Lau

© Jon Van Noord 1999
All Rights Reserved

This dissertation is dedicated to my family:
my dad, Phil Van Noord
my mom, Betty Van Noord
and my siblings, spouses and their kids:
Dave, Nancy, Dan and Tom Van Noord
Tim Van Noord
Steve, Elise, Blake and Laurel Van Noord
Beth and Greg Hess
Mike Van Noord

Also to my fiancée Annabel Cutland.

You have been a true blessing through this whole experience.
Dedicated foremost to God, you have designed an amazing universe.

ACKNOWLEDGMENTS

Several people have helped me with this work. Many friends and colleagues have helped me with support, encouragement and suggestions. I would like to thank first and foremost, my advisor, Professor Alec Gallimore. I have spent countless hours in your office learning and discussing electric propulsion. Thank you for the opportunity to be involved in such an exciting field. I would also like to thank my committee members for reviewing my thesis, Professors William J. Anderson (fellow volleyball enthusiast), James P. Holloway and Yue Ying Lau.

I would also like to thank the “lab guys” for your support and suggestions. Thanks Matt for commiserating with me over the difficulty of the hollow cathode. Thanks to the other “lab guys” for putting up with a non-experimentalist like me: George, Tim, James, Rich, Colleen, Frank and Sang.

I want to thank all the NASA Glenn Research People who have helped me also. Vince Rawlin, you were always quick to answer my myriad of questions. Jim Sovey, thanks for the support of me. Thanks also to Roger Myers, who told me to not forget the end prize and gave me much support (I’m almost there!). Thanks also to Frank Curran, Mike Patterson and the many others who have helped me.

I also want to thank the NSTAR people out at the Jet Propulsion Laboratory. I really enjoyed my summer with you guys. Thank you Jack Stocky for inviting me out there. Thanks also to Carl, Bob, Henry, Mike, John, Ray and Leota. Carl thanks for you advice. Bob thanks for taking me in as one of your own and introducing me to people spanning the fields from the Galileo project, to science fiction and SETI. I’ll always think

of you as Meg Ryan's co-star. Thanks Leota for taking me under your wing and looking out for me. Thanks also to Glen for answering all of my thermal modeling questions.

I especially want thank my family for their constant support. My mom and dad have continually encouraged me. Mom, thanks for challenging me to say "why not" when it came to my dreams. My siblings are my best friends who I love to laugh with. Thanks also to Annabel, you have lit up my life and encouraged me.

This work has been supported by the National Aeronautics and Space Administration under contracts NAG3-1572 and NAG3-2148.

TABLE OF CONTENTS

ACKNOWLEDGMENTS.....	III
LIST OF FIGURES.....	VII
LIST OF TABLES.....	IX
LIST OF APPENDICES	X

CHAPTER

I.	INTRODUCTION.....	1
	<i>1.1 Background.....</i>	<i>1</i>
	<i>1.2 Operation of an Ion Thruster.....</i>	<i>3</i>
	<i>1.3 Motivation</i>	<i>7</i>
	<i>1.4 Prior Work.....</i>	<i>9</i>
	<i>1.5 Thesis Outline</i>	<i>14</i>
II.	DERIVATION OF PLASMA DEPOSITION POWER EQUATIONS	16
	<i>2.1 Cathode</i>	<i>16</i>
	2.1.1 Energy Exchange Components.....	18
	2.1.2 Energy Balance Equation.....	26
	<i>2.2 Discharge Chamber</i>	<i>28</i>
	2.2.1 Power Deposition Equations	30
	2.2.2 Currents	33
	2.2.3 Discharge Chamber and Plasma Parameters.....	36
	<i>2.3 Power Deposition Equation Derivation Conclusion.....</i>	<i>42</i>
III.	COMPARISON OF ANALYTICAL RESULTS TO PREVIOUS WORK	43
	<i>3.1 Cathode</i>	<i>43</i>
	3.1.1 Solution Method.....	43
	3.1.2 Varying Cathode Parameters.....	45
	<i>3.2 Discharge Chamber</i>	<i>64</i>
	3.2.1 Baseline Plasma Ion Energy Cost, ϵ_p^*	64
	3.2.2 Variation of Uncertain Parameters	65
	3.2.3 Comparison of Model Results to a SERT II-Type (Culham) Mercury Thruster	82
IV.	COMPUTER THERMAL MODEL OF AN NSTAR ION THRUSTER	87
	<i>4.1 Model Description</i>	<i>87</i>
	4.1.1 Thermal Model.....	87
	4.1.2 Self-Heating due to Plasma Interaction	99
	<i>4.2 Model Results And Discussion.....</i>	<i>103</i>
	4.2.1 Cold-Soak Case.....	103
	4.2.2 Transient Analysis.....	105
	4.2.3 Thruster Operating at Throttling Points of 0.5, 1.3 and 2.3 kW	109
	4.2.4 Model Prediction for Directional Heat Dissipation.....	112
	<i>4.3 Computer Model Conclusions</i>	<i>115</i>

V.	EVALUATING THE NSTAR ION THRUSTER WITH VARIOUS MODELS..	117
	<i>5.1 Independent Variables Used for Thruster Test Cases.....</i>	<i>117</i>
	<i>5.2 Comparison of Results</i>	<i>119</i>
	5.2.1 Discharge Chamber Particle Parameters	119
	5.2.2 Analytical Prediction of Particle Currents and Power Depositions	120
	5.2.3 Comparison between SINDA model and Analytical Prediction.....	123
	5.2.4 Temperature Profiles Predicted from Analytical Model	127
VI.	CONCLUSION AND FUTURE WORK RECOMMENDATIONS	129
	<i>6.1 Conclusion.....</i>	<i>129</i>
	<i>6.2 Future Work Recommendations.....</i>	<i>131</i>
	BIBLIOGRAPHY	134

LIST OF FIGURES

Figure 1.1. NSTAR Ion Thruster Layout	4
Figure 1.2. Hollow Cathode Layout.....	4
Figure 1.3. Cusped Magnetic Field.....	6
Figure 1.4. Divergent Magnetic Field.....	6
Figure 2.1. Hollow Cathode Heat Transfer Mechanisms.....	17
Figure 2.2. Differential Elements along the Tube (Cathode)	18
Figure 2.3. Potentials on an Ion Thruster	28
Figure 2.4. Maxwellian Electron Rate Factor for Xenon.....	39
Figure 3.1. Cathode Temperatures for Varying Plasma Densities.....	49
Figure 3.2. Cathode Temperature for Different Work Functions and $I_{CE}=10A$	50
Figure 3.3. Cathode Temperature Profile for Different Ohmic Heating Values.....	51
Figure 3.4. Cathode Temperature with Different Convection Terms.....	54
Figure 3.5. Cathode Temperature Profile for Different Conductivities	55
Figure 3.6. Cathode Temperature Profiles for Different Emissive Terms.....	60
Figure 3.7. Temperature Profiles of a Cathode with a 1.9 eV Work Function Insert for Various Cathode Emission Currents (Salhi's Error $\pm 50^{\circ}C$).....	61
Figure 3.8. Temperature Profiles of a Cathode with a 2.0 eV Work Function Insert for Various Cathode Emission Currents (Salhi's Error $\pm 50^{\circ}C$).....	62
Figure 3.9. Thermionic and Ion Current as a Function of Cathode Emission Current	63
Figure 3.10. Plasma Heating and Cooling Mechanism as Function of Cathode Emission Current	63
Figure 3.11. Baseline Plasma Ion Energy Costs for Xenon	65
Figure 3.12. Change in Plasma Interaction Current with a Change in the Volume of the Ion Production Region	68
Figure 3.13. Change in the Power from Plasma Deposition with a Change in the Volume of the Ion Production Region	68
Figure 3.14. Change in Plasma Interaction Current with a Change in the Extracted Ion Fraction	70
Figure 3.15. Change in the Power from Plasma Deposition with a Change in the Extracted Ion Fraction	70
Figure 3.16. Change in Plasma Interaction Current with a Change in the Primary Electron Length	72
Figure 3.17. Change in Power from Plasma Deposition with a Change in the Primary Electron Length	72
Figure 3.18. Change in Plasma Interaction Current with a Change in the Anode Fall	74
Figure 3.19. Change in Power from Plasma Deposition with a Change in the Anode Fall	74
Figure 3.20. Change in Plasma Interaction Current with a Change in the Transparency of the Screen Grid to Ions	76
Figure 3.21. Change in Power Deposition from Plasma with a Change in the Transparency of Screen Grid to Ions.....	76

Figure 3.22. Change in Plasma Interaction Current with a Change in the Effective Transparency of the Grids to Neutrals	78
Figure 3.23. Change in the Power from Plasma with a Change in the Effective Transparency of the Grids to Neutrals	78
Figure 3.24. Variation of the Maxwellian Electron Temperature with the Changes in Various Parameters	79
Figure 3.25. Variation of the Maxwellian Electron Density for Changes in Various Parameters	81
Figure 3.26. Variation of the Primary Electron Density for Changes in Various Parameters	81
Figure 3.27. Variation of the Ion Density for Changes in Various Parameters	82
Figure 4.1. NSTAR Ion Thruster Thermal Model Nodal Layout	91
Figure 4.2. NSTAR Cathode Thermal Model Layout	91
Figure 4.3. Experimental Setup of Cooling Shroud in Vacuum Tank	93
Figure 4.4. Model Layout of Thruster in Cooling Shroud	94
Figure 4.5. NSTAR Thruster Layout	95
Figure 4.6. Perforated Surfaces on Ion Thruster	97
Figure 4.7. Modeling Approximation of Ion Optics used in TRASYS	99
Figure 4.8. NSTAR Thruster Steady State Temperatures under Cold Soak Conditions	104
Figure 4.9. Transient Temperatures of Shroud in Cold Soak Experiment (Experiment Temperatures $\pm 5^{\circ}\text{C}$)	106
Figure 4.10. Transient Cold Soak Experiment Compared to SINDA model of NSTAR Thruster for Plasma Screen Nodes (Experiment Temperatures $\pm 5^{\circ}\text{C}$)	106
Figure 4.11. Transient Cold Soak Experiment Compared to SINDA model of NSTAR Thruster for Discharge Chamber Nodes (Experiment Temperatures $\pm 5^{\circ}\text{C}$)	107
Figure 4.12. Transient Cold-Soak Experiment Compared to SINDA model of NSTAR Thruster (Experiment Temperatures $\pm 5^{\circ}\text{C}$)	107
Figure 4.13. NSTAR Thruster Steady State Temperatures for Throttling at 2.3 kW ...	110
Figure 4.14. NSTAR Thruster Steady State Temperatures for Throttling at 1.3 kW ...	110
Figure 4.15. NSTAR Thruster Steady State Temperatures for Throttling at 0.5 kW ...	111
Figure 4.16. Heat Flux from NSTAR Thruster to Box Sides with Space Conditions ...	113
Figure 5.1. NSTAR Thruster Steady State Temperatures for Throttling at 0.5 kW	125
Figure 5.2. NSTAR Thruster Steady State Temperatures for Throttling at 1.3 kW	126
Figure 5.3. NSTAR Thruster Steady State Temperatures for Throttling at 2.3 kW	126
Figure 5.4. NSTAR Main Cathode Temperatures Predicted from Analytical Model ...	127
Figure 5.5. NSTAR Neutralizer Cathode Temperatures Predicted from Analytical Model	128

LIST OF TABLES

Table 3-1 Comparison of Two $I_{CE}=5$ A Predicted Cases by Varying Different Plasma Properties	47
Table 3-2 Cathode Properties Corresponding to Figure 3	50
Table 3-3 Cathode Properties Corresponding to Figure 3.2	51
Table 3-4 Cathode Properties Corresponding to Figure 3.3	52
Table 3-5 Cathode Properties Corresponding to Figure 3.4	54
Table 3-6 Cathode Properties Corresponding to Figure 3.5	55
Table 3-7 Cathode Properties Corresponding to Figure 3.6	60
Table 3-8 Cathode Properties Corresponding to Figure 3.7	61
Table 3-9 Cathode Properties Corresponding to Figure 3.8	62
Table 3-10 Parameters Held Constant while the Volume of the Ion Production Region was Varied.....	67
Table 3-11 Parameters Held Constant While the Extracted Ion Fraction was Varied.....	69
Table 3-12 Parameters Held Constant While the Primary Electron Length was Varied .	71
Table 3-13 Parameters Held Constant while the Anode Fall was varied	73
Table 3-14 Parameters Held Constant While the Transparency of the Screen Grid to Ions was Varied.....	75
Table 3-15 Parameters Held Constant while the Transparency of the Screen Grid to Neutrals was Varied.....	77
Table 3-16 Values Used in Model of the Culham Thruster	83
Table 3-17 Comparisons of Ion and Electron Losses in the Culham Thruster.....	84
Table 3-18 Comparison of Experimentally Derived Plasma Power Deposition to Modeled Values.....	86
Table 4-1 Assumed Physical Properties Of Ion Thruster Materials.....	96
Table 4-2 Self-Heating Values used For Wen and Oglebay’s Ion Thrusters	102
Table 4-3 A Priori Values Based on Wen and Oglebay’s Values and Final Adjusted Values	102
Table 4-4 Energy Interchange between Plasma Screen, Discharge Chamber and Environment for the Cold-Soak Experiment	109
Table 4-5 Energy Interchange Between Plasma Screen, Discharge Chamber and Environment for the 2.3 kW Throttling Level.....	113
Table 5-1 Discharge Chamber Independent Variables.....	118
Table 5-2 Main and Neutralizer Independent Variables	118
Table 5-3 Predicted Discharge Chamber Particle Parameters.....	120
Table 5-4 Main Cathode Particle Currents and Powers.....	121
Table 5-5 Neutralizer Cathode Particle Currents and Powers	121
Table 5-6 Predicted Discharge Chamber Currents and Power Depositions.....	122
Table 5-7 Comparisons of Power Deposition Based on SINDA Model and Analytical Predictions	124

LIST OF APPENDICES

Appendix

CHAPTER I

INtroduction

1.1 Background

Electric propulsion is an expanding field in spacecraft propulsion offering many prospects for advancement. While most electric propulsion devices offer lower thrust than traditional chemical rockets, electric propulsion offers substantial savings in propellant and hence, spacecraft mass. If electric propulsion is operated for an extended period of time a spacecraft can attain a high velocity for a fraction of the amount of propellant it would have taken using chemical means. Electric propulsion offers to open even more of the heavens at a lower cost. In fact, Wernher von Braun once stated, “I wouldn’t be a bit surprised if one day we flew to Mars electrically! [1]”

There have been several types of electric propulsion devices developed ever since R. H. Goddard wrote down in his notebook in 1906 that electrostatically repelled particles might give high exhaust velocities at bearable temperatures[2]. The different electric propulsion devices can be divided into three main fields: 1) electrothermal, 2) electrostatic, and 3) electromagnetic.

Electrothermal propulsion uses electrical means to produce the heating and expansion of a propellant. Two such propulsion units are the arcjet and the resistojet. These use a nozzle similar to chemical rockets to gain the thrust from expanding gases. The specific impulses (Isp) of these two electrothermal propulsion rockets range from 300 seconds with storable propellant to 2000 seconds with hydrogen [3]. Arcjets used on communications satellites have Isp’s between 500-650 seconds. This compares to chemical propellant systems that could have an Isp of up to 470 seconds [4, 5, 6].

Electrostatic propulsion uses electric fields to accelerate ionized gas. The ion thruster is one example of this type. This thruster, the subject of this thesis, currently can produce an Isp of 3300 seconds [4, 7]. A description of this engine will be provided later.

Electromagnetic propulsion consists of accelerating ionized gas with electromagnetic body forces enabled by magnetic fields which are either self-induced or from an outside source. Two thrusters which fit this category are the magnetoplasmadynamic (MPD) thruster and the Hall thruster. The specific impulse of these thrusters is from 1000 to over 4000 seconds [4, 8,9].

There are a variety of missions which best fit each type of device depending on their individual size, complexity, Isp, thrust and other concerns. Electric propulsion's winning elements are its high exhaust velocities and fuel efficiency. This allows electric propulsion thrusters to become mission enabling for several missions that would require too much fuel using chemically produced thrust. These missions range from satellite station keeping to exploring deep space. The spacecraft using electric propulsion would be cheaper to launch since the spacecraft's launch weight would be drastically lowered because of the reduction in its fuel mass, and in the case of deep space missions, the reduced excess hyperbolic velocity that the launch vehicle must provide.

The ion thruster stands out with its specific impulse of 3300 seconds. Both the ion thruster and the MPD thruster are promising for use on a piloted mission to Mars. Multimegawatt solar electric propulsion or nuclear electric propulsion using these thrusters provide significant improvements in trip time to Mars and initial mass in low earth orbit over the chemical systems [5].

Several other missions can benefit from ion thrusters. For near Earth missions this includes north-south station-keeping for geostationary satellites which could have lifetimes up to 18 years [10, 11]. Ion thrusters would also be useful for orbit transfers near Earth [6, 10] and science missions such as mapping the Earth's magnetosphere[6], measuring Earth's gravity field[12], and Earth observing missions where drag would need to be

compensated for[13]. Many missions for exploration of the solar system could also profit from the ion thruster as well as the piloted Mars mission. These include an Europa Orbiter, Solar Probe, Comet Nucleus Sample Return, Jupiter multiprobe, Mercury orbiter, and many others[7].

Several countries have been developing different versions of the ion thruster. Some of the countries include the U.S.[14], the U.K.[11, 12], and Italy[13]. The U.S. launched Deep Space 1 in October of 1998 with an ion thruster developed by the NASA Solar Electric Propulsion Technology Application Readiness (NSTAR) program. This mission is to validate the ion thruster and fly by an asteroid and comet in 1999[14].

Several different propellants have been investigated for the thruster from mercury[16] to noble gases such as xenon[14] and argon to fullerene vapor[15]. The designs have varied from using cathodes to produce electrons to bombard neutral gases to using radio frequency microwaves to create ions. The designs also vary in size, with grid diameters ranging between 1.5 m to a proposed 6 cm [14, 16].

1.2 Operation of an Ion Thruster

The electron bombardment ion thruster can be divided into 3 stages. The first stage involves the production of electrons. The second stage uses the electrons produced to collide with neutral propellant molecules to create ions. These ions are then accelerated through an electric field to produce the thrust. Kaufman gave a substantial overview of the technology behind the electron-bombardment ion thruster in 1974 [17]. The layout of the most current electron-bombardment ion thruster being developed by NASA, the NSTAR ring-cusp ion thruster, is shown in Figure 1.1 and largely retains much of the features found on earlier engines.

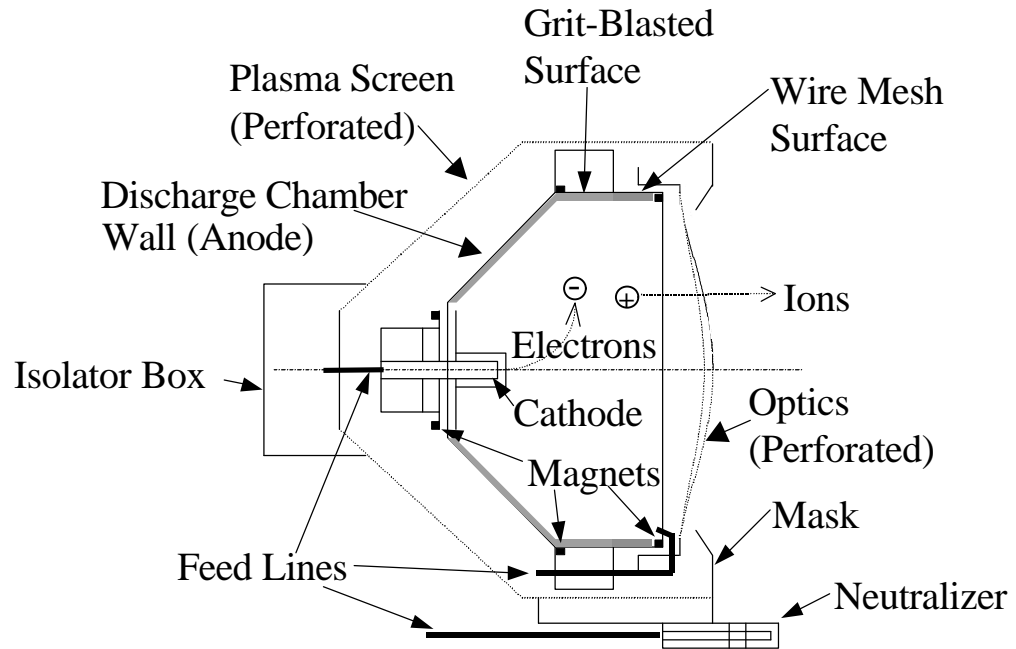


Figure 1.1. NSTAR Ion Thruster Layout

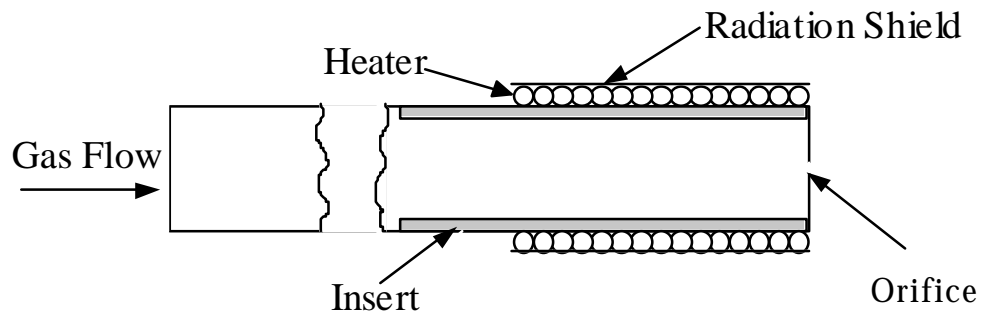


Figure 1.2. Hollow Cathode Layout

The electron source of past thrusters was a wire filament cathode, but today hollow cathodes are used. The layout of a typical hollow cathode is shown in Figure 1.2. Hollow cathodes are ignited by heating the impregnated porous tungsten insert to around

1000 °C, allowing the gas to flow through the cathode, and then applying a discharge voltage between the cathode and an external electrode. This causes thermionic emission of electrons along the insert. These electrons then interact with the gas flowing through the cathode to form the plasma. Once the plasma has fully developed, the cathode can be self-sustaining and the heater is no longer needed. The ions in the plasma will recombine on the surface of the insert to deposit their energy and sustain the temperature necessary for thermionic emission. The electrons are then drawn out through the orifice towards the anode.

The discharge chamber of the ion thruster is the region in which ions are produced. A 30-50 V potential difference draws electrons from the cathode to the anode. In addition to electric fields, magnetic fields are produced by permanent magnets located circumferentially around the thruster. The arrangement of magnets as shown in Figure 1.1 produces a magnetic field referred to as a cusped magnetic field (Figure 1.3). Previous thruster designs used a divergent magnetic field (Figure 1.4). Cusped fields were found to improve the ionization efficiency in the discharge chamber.

When the electrons leave the cathode, they follow the magnetic field lines and spiral due to their interaction with the electric and magnetic fields. This effectively increases the path length they travel before being collected at the anode. The path length that a primary electron would travel without an inelastic collision and then be collected at the anode is referred to as the primary electron containment length.

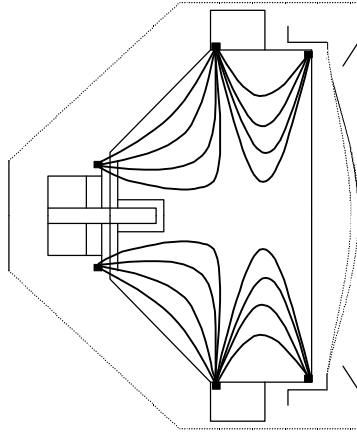


Figure 1.3. Cusped Magnetic Field

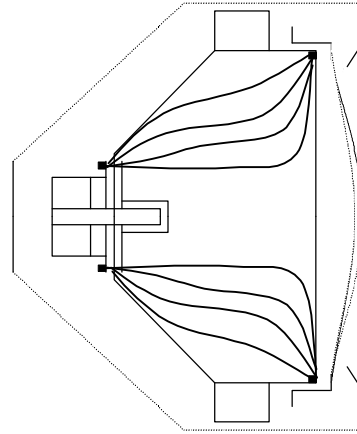


Figure 1.4. Divergent Magnetic Field

The critical field line is defined as the innermost magnetic field line that intercepts the anode. This line is important because an energetic electron crossing this line will be collected by the anode since the potential drop in the anode sheath is not able to reflect these electrons. (Note: In ion thrusters, the plasma assumes a potential of a few volts positive to the anode, resulting in a slightly electron retarding anode sheath [41].) The region contained by the critical field line is referred to as the primary electron region or the ion production region. It is here that the collisions of interest take place.

In the discharge chamber, there are two types of electrons present: primary electrons and Maxwellian electrons. Primary electrons are those produced by the cathode which have not undergone inelastic collisions in the discharge chamber. As such, their energy is determined by the potential difference between the cathode and the anode. Maxwellian electrons have had inelastic collisions in the discharge chamber resulting in a lower-energy Maxwellian velocity profile [41]. Generally, the ions are produced from collisions between both types of electrons and neutral gas atoms, which are introduced into the discharge chamber. The propellant gas used for the NSTAR thruster was xenon.

The ions created in the discharge chamber are then drawn towards the two acceleration grids (the so-called ion optics). The screen grid is the discharge chamber side of the optics and is kept at cathode potential. When the ions reach the screen grid, they are accelerated out of the accelerating grid, which is spaced less than a millimeter from the screen grid and about 1100 V below the screen grid potential. This gives the ions a very high exhaust velocity (~30 km/s). To obtain a screen grid with that high of a voltage, the entire discharge chamber and cathode have a potential difference of over 1000 V above space ground (see Figure 2.3 below).

Once the ion beam leaves the thruster, it needs to be neutralized so that it doesn't reverse direction and impinge on the thruster and bias the thruster and spacecraft negatively. This process is done by the neutralizer, which is a hollow cathode located on the outside of the thruster close to the beam. Thus an electron is emitted parallel to the beam for each ion. The accelerator grid is biased negatively with respect to space ground a few hundred volts to keep neutralizer electrons from backstreaming into the discharge chamber.

1.3 Motivation

Despite its many advantages, the application of ion propulsion to scientific, military, and commercial spacecraft was hampered in the past by perceived high engine development costs and the inability of spacecraft manufacturers to reliably identify potential integration and thruster lifetime issues. The primary concerns that spacecraft manufacturers had in regard to using ion propulsion included the likely impact of thruster operation on spacecraft design and operations, electromagnetic compatibility, spacecraft contamination from thruster efflux, spacecraft damage from the plume, thruster reliability, and thermal loading of the spacecraft from the thruster. Ion propulsion will continue to

become more attractive as more tools are developed (e.g., plume PIC codes[18]) to help spacecraft manufacturers identify potential spacecraft integration issues associated with this technology.

Given the wide range of thermal environments an ion thruster on a deep-space mission or in geostationary orbit will likely encounter, it is essential that computer tools be developed to predict the temperatures of thruster components over the expected range of operating and thermal conditions. Some critical areas of concern include the degaussing of permanent magnets from excess heating, freezing of xenon in propellant lines[19], distortion of the ion optics from thermal gradients[20], and spacecraft integration issues in general (e.g., thermal soakback).

Tied very closely with thermal analysis is efficiency. Generally, the excessive deposition of energy and the corresponding increase in temperature represents a loss. Ideally, all of the power added to the system is desired for use in creating and accelerating the ions. One of the few cases where power deposition is beneficial is with the cathode. This power deposition is used to maintain a temperature sufficient for thermionic emission. However, some of this power deposited is lost because imperfect insulation of the insert allows some energy to escape and not be used for electron emission.

The work presented here was motivated by the need to develop a tool which could be used for both thruster design and spacecraft integration activities. The model presented here will be useful in evaluating different thruster throttling levels, different size thrusters, different propellants and many other parameters. If an accurate means of predicting internal power deposition, power expelled from the thruster and thruster temperatures can be attained, the thruster and its integration into a spacecraft can be improved.

1.4 Prior Work

Although work has been done in the past to predict the temperatures of 20-cm-diameter [21] and 30-cm-diameter [22] divergent-field ion thrusters utilizing mercury propellant, no such model has been developed to predict temperatures for modern ring-cusp xenon thrusters like the NSTAR engine. Wen *et al.* [21] started by predicting electron and ion fluxes to various thruster surfaces to determine a priori estimates of the power deposited on a 20-cm-diameter thruster. They then adjusted these numbers after statistically fitting the temperatures of their thermal model to experimental results. Oglebay then scaled the values he used from Wen *et al.* to fit the 30-cm thruster and proceeded to adjust those values to obtain a temperature fit between his model and experimental data[22]. The same approach as Oglebay was used initially to determine the self-heating terms on the NSTAR thruster [23]. The starting values used with the NSTAR thruster were derived from Wen *et al.* and Oglebay's power deposition model. The tests used for calibrating this model were based on experiments performed at NASA Lewis Research Center (now the John Glenn Research Center) in June and July of 1996[24].

Once adjusted to match experiments, these models can be used to investigate other operating conditions. The NSTAR model has already been used to alert of the possible dangers of overheating the magnets at certain thruster settings. Other issues investigated with the NSTAR model but not presented here include enclosing the thruster in an adiabatic surface, changing materials on the thruster, and the influence of ambient conditions in space on the thruster.

A more direct method of determining the temperatures that the ion thruster will be experiencing is by testing the thruster in an experimental environment. This has been done

for many designs of the ion thruster. Mirtich simulated the coldness of space on a 30-cm mercury ion thruster (Hughes 400 series thruster) using liquid nitrogen cooled shielding and he simulated the radiation from 2.5 suns intensity using carbon arc lamps [25].

Mirtich then performed several similar tests on the Hughes 700 series ion thruster [26]. This thruster differed from the 400 series thruster because some of the material that was aluminum and stainless steel on the 400 series engine was changed to titanium.

The next generation ion thruster, the J series ion thruster, was again tested under several conditions [27]. The J series thruster had significant changes in the optics from the 700 series. The open area of the accelerator grid went from 43 percent for the 700 series to only 23 percent for the J series. This decrease in open area increased the temperatures in the thruster. The concern that the increase in temperature might result in outgassing of organic materials such as the wire insulation was the reason additional thermal testing was done on this thruster.

The most recent version of the ion thruster tested at NASA is the NSTAR ion thruster [24]. This thruster also has significant changes from the previous thrusters. The previous thrusters were divergent-field thrusters instead of cusped-field design of the NSTAR thruster. This also resulted in a change in the shape of the thruster. The previous thrusters were mainly cylindrical in shape, while the NSTAR thruster is conical on the rear half of the thruster (see Figure 1.1).

An important point to modeling the thermal response of the thruster is to understand the power deposited from the plasma. The ion thruster has four predominant areas where the plasma generated in a thruster interacts with various surfaces. They are

the main cathode, the neutralizer cathode, the anode, and the ion optics. The plasma deposits its energy on these components resulting in a heat flux.

The hollow cathode is among the most complex of the components to determine its heat flux since the amount of net heating is a balance between cooling from thermionic emission and heating due to the ions depositing their energy onto the cathode. In order to predict the net heat flux into the cathode, it is necessary that a model simultaneously predict the cathode temperatures, net heat flux, and the thermionic emission current level, which is highly dependent on the temperature of the cathode.

Several studies have examined the hollow cathode discharges by both experimental and analytical means [28, 29, 30, 31, 32]. Many of these investigations yield the temperature profiles of the cathode [28, 29, 30, 32]. Salhi reported these profiles along with measured plasma traits in the cathode [29]. A comprehensive model has not previously been presented in literature that incorporates many of the plasma and heat transfer characteristics in the cathode.

Siegfried summarizes several of the key hollow cathode equations in the appendix of a paper on ion thruster research by Wilbur [33]. However, there is still a degree of uncertainty as to the exact mechanics present. A significant factor of the uncertainty is due to the difficulty in experimentally determining several plasma properties over a small section of the cathode. Siegfried [30] showed that up to 90% of the current emission occurs in the first 2 mm of the insert. Capacci *et al.* [31] also list several equations that give the current to the cathode surface.

In order to determine the temperature profile and heat flux in the cathode, a model handling both the plasma energy and the heat transfer along the cathode needed to be

developed. Siegel *et al.* derived an equation for the temperature profile in a tube that included forced convection, internal radiation exchange and axial wall heat conduction [34, 35]. Siegel *et al.* also determined how to include gray body radiation in the equation [35, 36]. These equations were used as starting points to which the energy from the plasma interaction and additional heat transfer considerations were included. Two different numerical solution methods were examined for this equation. One was a Runge-Kutta method [37], and the other was by another finite difference approach [34].

In order to predict the power deposited into the anode, a comprehensive understanding of the plasma properties in the discharge chamber is required. Wells *et al.* examined several of the losses to surfaces on a Culham thruster [38]. This thruster was based on the SERT II thruster, the thruster version NASA was developing around 1970. He measured the current to several of the surfaces and then used a Langmuir probe and other probes to determine many of the plasma parameters such as the plasma potential, the electron temperature, and plasma density. From the probe data, he then determined the amount of current that was attributed to ions and electrons moving to the surfaces and the amount of power they deposit into the surfaces.

Masek determined a way of predicting ion and electron fluxes to various surfaces based on the velocity of the particle, and its density [39, 40]. He showed that it is valid to determine the velocity of the particle to a surface using the Bohm sheath criterion. He also presented plasma properties for a 15 and 20-cm-diameter mercury divergent-field thruster.

Brophy then presented an ion thruster performance model for cusped magnetic field thrusters [41]. Brophy's model enables the prediction of primary electron density,

Maxwellian electron density, and the Maxwellian electron temperature. These terms are shown to be available from only four thruster configuration dependent parameters (the primary electron utilization factor, the baseline plasma ion energy cost, the extracted ion fraction, and the cathode potential surface ion fraction) and two operating parameters (propellant flow rate and discharge voltage).

Understanding how the power is deposited into the optics is critical for an ion thruster. The optics are generally the limiting factor on the life of an ion thruster. The impingement of ions gradually degrades the grids to the point of structural failure [42]. The distortion of grids is also another concern. Misalignment of grids at a minimum causes a loss in thrust and life due to increased ion impingement. A severe distortion of the grids could result in contact between the screen and accelerating grids that would lead to an electrical breakdown [17]. These concerns have been addressed by using dished grids [43] and investigating the use of composite material grids [44, 45].

Monheiser developed a model to predict the ion impingement on the accelerator grids [46]. He determined that a majority of the ions impinging on the accelerator grid are charge-exchange ions produced in the immediate vicinity of the grid on both sides. He also measured the plasma potential through the openings in the grid.

MacRae *et al.* outfitted the 900 and J-series thruster optics with several thermocouples to measure temperatures at various discharge powers [20]. The displacements of the grids were also measured. However, no beam was extracted, so it is uncertain how well the results on the accelerator grid can be extrapolated to the case when the beam is extracted.

Thrusters prior to the NSTAR thruster have had a considerable amount of experimentation performed on them. There is a need for modeling thrusters while minimizing the amount of experimentation necessary. One useful model would be to predict the power deposited into the thruster. This will be useful for predicting the thruster temperatures for various conditions and showing where losses occur.

1.5 Thesis Outline

There has been a substantial amount of research on the ion thruster, so much so that this technology has advanced enough to currently be used in spaceflight. However, improvements continue to be made to these thrusters and there are many mechanisms not fully understood yet. This dissertation intends to:

1. Develop a model to predict the temperatures of the NSTAR thruster.
2. Produce a method for predicting the power deposited to the ion thruster for different operating levels and design changes.

Chapter II of the dissertation will develop the equations used to determine the power deposited into the anode, optics (screen and accelerator grids), and cathode. The power deposition in the discharge chamber will be based on Brophy's model to determine the plasma characteristics. The power deposition into the cathode will involve solving a heat transfer problem since the rate at which electrons are emitted is temperature dependent.

Chapter III will then compare results of the derived equations to previous models and experiments. The plasma properties of the discharge chamber will be evaluated. Temperature and previously reported energy fluxes will also be used for comparison.

Chapter IV will contain the model of the NSTAR ion thruster created using the thermal code SINDA. This model will be compared to experimental data. The operating conditions include cold-soaking a non-operating thruster in a liquid nitrogen cooled

shroud, and operating the thruster at three throttling points within the shroud (0.5 kW, 1.3 kW, and 2.3 kW). Values for the power deposited on the surface based on the thruster temperatures will be presented for each of the throttling points.

Chapter V will compare the power deposition rates using the SINDA model and the analytically determined ones for the same three throttling point cases used in Chapter IV. It will also include using the analytical values in the SINDA model to compare predicted temperature results to the Chapter IV SINDA model and experiments.

Chapter VI will present the summary, conclusions, and recommendations for future research.

Appendix A shows the derivation of the radiation shape functions used to develop the solution for the cathode heat transfer problem. Appendix B contains the solution routines used for solving the analytical equations. Appendix C presents the FORTRAN code written to solve the analytical equations along with a description of the program and sample input and output files. Appendix D contains the nomenclature used in the main body of this dissertation.

CHAPTER II

DERIVATION OF PLASMA Deposition Power Equations

In order to understand the thermal characteristics of an ion thruster it is important to model the power deposition into the thruster from the plasma. There are two primary regions of plasma deposition in an ion thruster: the cathode (main or neutralizer) and the discharge chamber region. To model the plasma interaction on the cathode, a heat transfer equation will have to be developed. This type of equation is necessary since the thermionic emission of electrons, which is a cooling factor, is temperature dependent.

The discharge chamber region will require modeling the plasma in the chamber. This model can then be used to determine the ion and electron currents to various surfaces and other plasma parameters that are necessary to determine the power, like the electron temperature.

2.1 Cathode

To determine a comprehensive thermal model of the hollow cathode, several heat transfer and plasma characteristics need to be examined. There are seven major energy exchange components present in the hollow cathode: 1) Radiation, 2) Conduction, 3) Convection, 4) Ohmic Heating of the Cathode, 5) Thermionic Emission, 6) Ionic Recombination, and 7) Electron Backstreaming. Each of these terms will be detailed in the following section. The electron backstreaming and ohmic heating of the cathode will be shown to have minimal impact on the cathode. Figure 2.1 depicts these on the hollow cathode and provides a picture of the cathode assembly.

Siegel *et al.* derived an equation that includes internal radiation, axial wall conduction, convection, and a term for ohmic heating [34]. His equation was used as a

starting point of the equation derived here. Several terms are added to his equation to account for processes such as external radiation, gray body radiation internally and externally, parameters such as inner diameter, emissivity, and conductivity varying along the length of the cathode, boundary conditions besides the insulated ones, and the plasma interaction. The equation is derived in a dimensional form since its specific application does not lend itself to nondimensionalization.

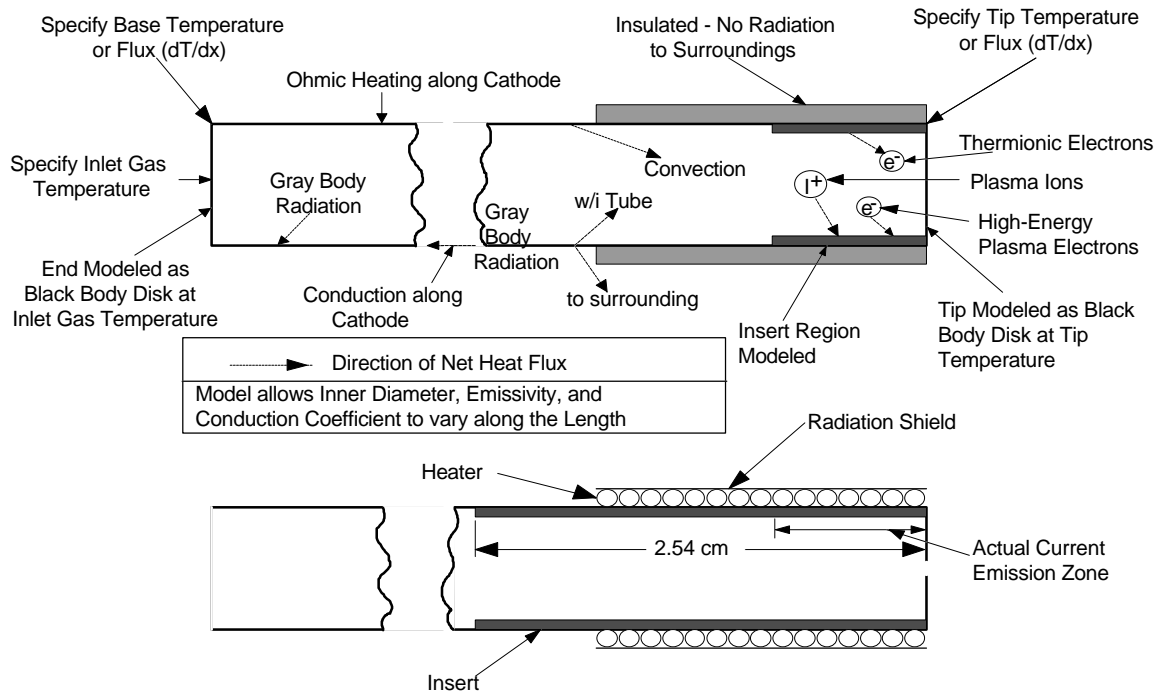


Figure 2.1. Hollow Cathode Heat Transfer Mechanisms

The derivation is accomplished by examining the heat flux present in a differential ring element of length dx . Figure 2.2 shows this differential element within the hollow cathode setup. The final step in deriving the equation describing the energy exchange divides out $\pi D_x dx$ (differential ring surface area) on each term to get an overall equation.

The following section details each of the energy exchange components and how they fit into the overall energy equation.

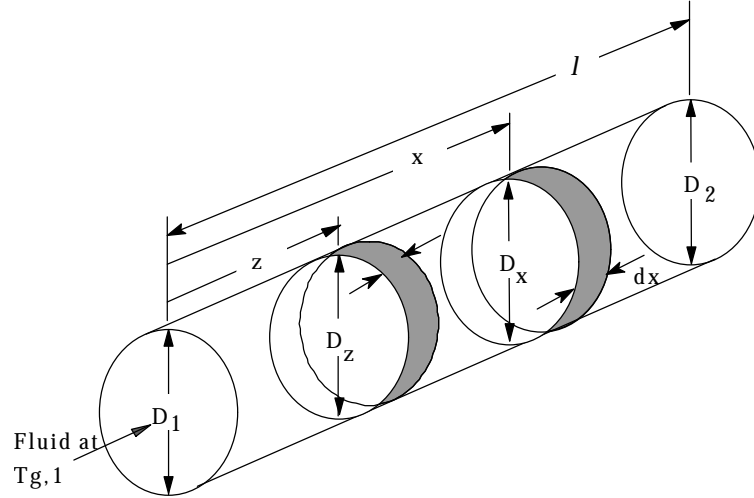


Figure 2.2. Differential Elements along the Tube (Cathode)

2.1.1 Energy Exchange Components

2.1.1.1 Radiation

The term for the heat flux from the radiation coming from all the differential dz elements shown in Figure 2.2 at a temperature of $T(z)$ to differential element dx and summed up is given by:

$$\int_{z=0}^l \sigma T_w^4(z) dF_{dz-dx}(|z-x|) \pi D_z dz \quad . \quad (2.1)$$

where σ is Stephan-Boltzmann's constant and dF is the differential shape function from differential element dz to dx . When reciprocity is used, Equation 2.1 can be written with $\pi D_x dx$ to be:

$$\int_{z=0}^l \sigma T_w^4(z) dF_{dx-dz}(|x-z|) \pi D_x dx \quad (2.2)$$

where for a constant inner diameter D and $X=|x-z|$, the differential view factor is

$$dF_{dx-dz}(X) = \left[\frac{1}{D} - \frac{2X^3 + 3XD^2}{2D(X^2 + D^2)^{3/2}} \right] dz \quad (2.3)$$

or for differing inner diameters at dx (D_x) and dz (D_z) the differential shape function is given in Equation 2.4.

$$dF_{dx-dz}(X) = \left[\frac{A(C + \frac{B}{2}) - 32C(C + B)X^2}{16B(C^2 + CB)^{3/2}} + \frac{1}{B} \right] D_z dz. \quad (2.4)$$

In Equation 2.4, $A=2B^2 - D_x^4 - D_z^4 + 16X^4$ and $B=D_x D_z$ and $C=(D_x^2+D_z^2)/4 - B/2 + X^2$ (derivation shown in Appendix A).

The term for the heat flux due to the radiation coming from the ends of the cathode to the differential element dx is given as:

$$s T_{r,1}^4(x) dF_{1-dx}(x) \frac{\rho D_1^2}{4} + s T_{r,2}^4(x) dF_{2-dx}(l-x) \frac{\rho D_2^2}{4} \quad (2.5)$$

where $T_{r,1}$ is the temperature at the entrance region of the cathode and $T_{r,2}$ is the temperature at the tip region. Equation 2.5 with reciprocity then gives:

$$\sigma T_{r,1}^4(x) F_{dx-1}(x) \pi D_x dx + \sigma T_{r,2}^4(x) F_{dx-2}(l-x) \pi D_x dx \quad . \quad (2.6)$$

The view factor in Equation 2.6 for constant inner diameter D and $X=|z_{1(or2)}-x|$ is:

$$F_{dx-1(2)}(X) = \frac{X^2 + \frac{D^2}{2}}{D\sqrt{X^2 + D^2}} - \frac{X}{D} \quad (2.7)$$

or for different diameters between the end ($D_{1(or2)}$) and dx (D_x),

$$F_{dx-1(2)}(X) = \left(\frac{A}{\sqrt{A^2 - \frac{D_{1(2)}^2 D_x^2}{4}}} - 1 \right) \frac{X}{D_x} \quad \text{where} \quad A = X^2 + \frac{D_{1(2)}^2 + D_x^2}{4} \quad (2.8)$$

(derivation shown in Appendix A).

The final terms for the radiation heat flux from the sections dx emitting into the tube and outside to the environment are given in Equation 2.9.

$$s T_w^4(x) \rho D_x dx + s \frac{D_o}{D_x} (T_w^4(x) - T_\infty^4) \rho D_x dx \quad (2.9)$$

Emissivity will be added to the over-all equation later in the derivation.

Radiation can come not only from the walls of the cathode, but also from the plasma within the cathode. Krall *et al.* [47] give the minimum radius necessary to contain enough plasma such that the black body radiation will be significant in the equation:

$$R_{bb} = \frac{10^{23} T^{7/2}}{Z^2 n_i n_e} \text{ cm.} \quad (2.10)$$

The temperature in Equation 2.10 is in degrees Kelvin, Z is the integer charge state, and the ion and electron densities are per cubic centimeter. If the calculated radius is much larger than the actual dimensions containing the plasma, the plasma is considered to emit minimal black body radiation. That is, in order for black body radiation from the plasma to be a factor, the plasma must occupy a volume with its radius on the order of the minimum radius calculated. For the cathode examined the plasma temperature T is around 17400 °K, and the densities are around $10^{15} / \text{cm}^3$, which results in R_{bb} to be around 6.95×10^7 cm, much larger than any dimension of the cathode.

Since black body radiation is insignificant, Bremsstrahlung radiation must now be considered. This radiation is emitted from particle collisions. It is given as:

$$P_{BR} = 1.69 \times 10^{-32} n_e T_e^{1/2} \sum Z^2 n(Z) \quad \text{W/cm}^3 \quad (2.11)$$

where Z refers to the ion charge state present [48]. Singly and doubly ionized atoms were assumed present in order to determine the maximum amount of radiation present. Each set of ionized atoms was then given a percent of the maximum reported density from Salhi at $10^{15} / \text{cm}^3$ ($n_i^+ / n_i^{\text{total}}$ for percent of singly ionized atoms and $n_i^{++} / n_i^{\text{total}}$ or $1 - n_i^+ / n_i^{\text{total}}$ for percent of doubly ionized atoms). This then gives the power as:

$$2.0698 \times 10^{-17} (1 \times 10^{15} (\frac{n_i^+}{n_i^{\text{total}}}) + 4 \times 10^{15} (1 - (\frac{n_i^+}{n_i^{\text{total}}}))) = 0.0828 - 0.0621 (\frac{n_i^+}{n_i^{\text{total}}}) \quad \text{W/cm}^3 \cdot (2.12)$$

The maximum value would be if the plasma contained no singly ionized xenon atoms and all doubly ionized atoms. The power density would be 0.0828 W/cm^3 . The first centimeter of the cathode more than contains the region where the plasma is located

and results in a volume of 0.114 cm³. This gives the power emitted from the plasma through Bremsstrahlung radiation to be 0.009 W. This value is insignificant in comparison with the total amount of power deposited into the cathode wall so the effect can be ignored.

2.1.1.2 Conduction

The heat transfer along the cathode wall due to conduction was taken from Siegel, who derived the expression for a tube of constant diameter [35]:

$$K_w \frac{D_o^2 - D_x^2}{4D_x} \frac{d^2 T_w}{dx^2} \pi D_x dx \quad (2.13)$$

where K_w is the conduction coefficient and D_o is the outer diameter of the tube.

If a cathode does not have a constant inner diameter, the diameter is assumed locally constant. Interface elements are derived where the diameters change. This is described in Appendix B.

2.1.1.3 Convection

The term given for the heat flux leaving the ring element from convection (see Figure 2.2) is given by standard heat transfer analysis:

$$h[T_w(x) - T_g(x)] \pi D_x dx \quad (2.14)$$

where h is the convection coefficient.

The function to determine the temperature of the neutral gas with a fully developed laminar flow in a tube is given by:

$$T_g(x) = St e^{-Stx} \int_{z=0}^x e^{Stz} T_w(z) dz + e^{-Stx} T_{g,i} \quad (2.15)$$

where St is the Stanton Number for the gas, and $T_{g,i}$ is the inlet gas temperature. Equation 2.15 is derived from:

$$\frac{dT_g}{dx} = St(T_w - T_g) \quad (2.16)$$

which relates the mean temperature of a gas in a tube with its wall temperature [49].

2.1.1.4 Ohmic Heating of Cathode Wall

Another source of heating is from the current running through the cathode wall. In order to determine Ohmic heating, its total heat flux must be related to the differential surface area. This is the form of the equation needed in order to divide out $\pi D_x dx$, which is necessary in the final step of deriving the overall heat flux equation. The Ohmic heating is given as:

$$Q_{total/dx} = q\pi D_x dx = i^2 R = i^2 \rho \frac{\text{length}}{\text{cross sectional area}} = i^2 \frac{\rho dx}{\pi \frac{D_o^2 - D_x^2}{4}}. \quad (2.17)$$

The term q will be the part that is left in the final equation after the internal surface area is divided out. To get the correct form to divide out the $\pi D_x dx$ term, $Q_{total/dx}$ is multiplied by $(\pi D_x dx)/(\pi D_x dx)$ to give:

$$Q_{total/dx} = \frac{I_{CE}^2 \rho}{\pi^2 D_x \frac{D_o^2 - D_x^2}{4}} \pi D_x dx \quad (2.18)$$

where ρ is the resistivity and I_{CE} is the emission current.

2.1.1.5 Thermionic Emission

The primary source of electrons for the hollow cathode is through thermionic emission [30,50]. Thermionic emission of electrons is the result of the cathode being sufficiently heated so that electrons can be “boiled” off. The electron emission has a cooling effect on the cathode from a release of energy. To accurately predict the current that is emitted from the cathode, the effect of the electric field must also be taken into account (so-called field-enhanced thermionic emission). This affects the work function of the insert by effectively lowering it. The emission current is determined mainly by the

temperature of the cathode, the work function of the insert, and the electric field present.

The thermionic current density is given by the Richardson-Dushman [29] equation:

$$J_{th} = A_R T^2 \exp\left[-\frac{e\phi_{eff}}{kT}\right]. \quad (2.19)$$

Where in Equation 2.19, the Richardson coefficient, $A_R=60 \text{ A/cm}^2 \text{ K}^2$, is based on empirical data presented in Fomenko's "Handbook of Thermionic Properties" [51] and used by Goodfellow in his thesis on cathode processes [52]. Many have used $A_R = 120 \text{ A/cm}^2 \text{ K}^2$ which is based on simplifying assumptions [29, 30, and 53]. It is important to use accurate terms for the work function, ϕ , and the Richardson coefficient since the thermionic emission is very sensitive to these terms [52]. Since the work function is in the exponential term, the thermionic current can vary dramatically with small changes in the value of the work function. Therefore, it will be important to include factors that could affect the work function, like the electric field.

As will be shown later, the work function can change around 0.1 eV because of the electric field. This can be compared to a temperature change in the wall of 300 °C, which only results in a 0.03 eV change of the temperature term in the exponent of Equation 2.19. The change in the work function from the electric field will have a significant effect in determining the current. A 0.1 eV change in the effective work function will have about the same effect as a 1000 °C change in cathode temperature.

The electric field effect, known as the Schottky effect, is then important to account for since it can lower the work function by tenth's of an electron volt. The effective work function is then given by [33]:

$$\phi_{eff} = \phi_s - \sqrt{\frac{e|E_c|}{4\pi\epsilon_o}}. \quad (2.20)$$

The electric field in the hollow cathode is a result of the plasma and sheath near the surface. The electric field at the cathode surface, E_c , can then be estimated by double sheath analysis to be [33]:

$$E_c \approx \left[\frac{n_e k T_e}{\epsilon_o} \right]^{1/2} \left[2 \left(1 + 2 \frac{e V_p}{k T_e} \right)^{1/2} - 4 \right]^{1/2} \quad (2.21)$$

where V_p is the plasma potential and ϵ_o is the permittivity constant, $8.85 \times 10^{-12} \text{ C}^2/\text{N m}^2$.

The net heat flux lost from the cathode is determined by the energy it takes to free an electron and its initial kinetic energy [54, 55, 56]. For the differential ring element of the cathode where emission takes place on the inside, this energy loss is given by the Equation 2.22.

$$J_{th} \left(\phi_{eff} + \frac{5kT_w}{2e} \right) \pi D_x dx \quad (2.22)$$

In Equation 2.22 the energy loss that takes place when an electron is freed from the wall surface is a function of its effective work function, ϕ_{eff} , and the kinetic energy present in the electron, $5kT_w/2e$ [57].

2.1.1.6 Ionic Recombination

The primary source of input cathode power is from the ions, created in the plasma, contacting the cathode surface [58]. The ion current can be determined from the plasma characteristics within the cathode. The ions are assumed to contact the surface of the cathode at a rate equal to the Bohm current. This is consistent with a Maxwellian plasma and a negatively charged surface. The Bohm current density is given by [59]:

$$J_i \approx 0.6 n_e e \sqrt{\frac{k T_e}{m_i}} . \quad (2.23)$$

Each ion pulls an electron off the insert in the cathode and deposits its kinetic and neutralization energy [29, 50, 54, 55]. This heat flux for a ring element is represented in Equation 2.24.

$$J_i \left(V_{fall} + \frac{5}{2} \frac{kT_i}{e} + U_+ - \phi \right) \pi D_x dx \quad (2.24)$$

The different terms in Equation 2.24 account for the kinetic and potential energies that are deposited on the cathode wall when recombination occurs. The term V_{fall} is the energy from the ion accelerating through the sheath near the wall. V_{fall} is the voltage potential between the edge of the sheath and the wall. The $5kT_i/2e$ term is the plasma ion kinetic energy at the sheath edge. U_+ is the ionization energy that is given up when the ion takes an electron from the wall surface and becomes a neutral atom. In the process of an ion becoming neutral, it frees an electron from the wall. This is a cooling term and is determined by the work function, ϕ .

2.1.1.7 Electron Backstreaming

Another possible power source could be from the energetic electrons at the tail of the Maxwellian curve coming back to the insert and depositing their energy. This appears to be a small fraction of the energy deposited, but rather than neglect it, it will be included and its impact can be evaluated later. The current density, which is a result of these electrons, is expressed by:

$$J_e = e n_e \left(\frac{kT_e}{2p m_e} \right)^{1/2} \exp \left(- \frac{eV_{fall}}{kT_e} \right) . \quad (2.25)$$

The energy from these electrons is due to the electrons being incorporated back into the surface given by the work function, ϕ , and the thermal energy present in the free electron, $5kT_e/2e$. This heat flux can be given for a ring element as:

$$J_e \left(\frac{5}{2} \frac{kT_e}{e} + \phi \right) \pi D_x dx . \quad (2.26)$$

2.1.2 Energy Balance Equation

2.1.2.1 Black Body Radiation

To derive the final equation based on energy, Equations 2.2, 2.6, 2.9, 2.13, 2.14, 2.18, 2.22, 2.24, and 2.26 are added together with the power in on the left-hand side and the power out on the right hand side. Then the equation is divided by $\pi D_x dx$ to give Equation 2.27. This equation gives a second order integral-differential temperature equation for a tube (hollow cathode) which includes plasma interaction, black body radiation inside and outside of the tube, conduction, convection and ohmic heating along the tube wall from an electric current.

$$\begin{aligned}
& \int_{z=0}^l \sigma T_w^4(z) dF_{dx-dz}(|x-z|) + \sigma T_{r,1}^4(x) F_{dx-1}(x) + \sigma T_{r,2}^4(x) F_{dx-2}(l-x) + K_w \frac{D_o^2 - D_x^2}{4D_x} \frac{d^2 T_w}{dx^2} \\
& + \frac{I_{CE}^2 \rho}{\pi^2 D_x (D_o^2 - D_x^2)/4} + J_i \left(V_{fall} + \frac{5 k T_i}{2 e} + U_+ - \Phi \right) + J_e \left(\frac{5 k T_e}{2 e} + \Phi \right) = \\
& \sigma T_w^4(x) + \sigma \frac{D_o}{D_x} (T_w^4(x) - T_\infty^4) + h \left[T_w(x) - S t e^{-S t x} \int_{z=0}^x e^{S t z} T_w(z) dz + e^{-S t x} T_{g,i} \right] \\
& + J_{th} \left(\Phi_{eff} + \frac{5 k T_w}{2 2e} \right)
\end{aligned} \tag{2.27}$$

2.1.2.2 Gray Body Radiation

Since the cathode surface varies from being a black body, it is important to determine a form of Equation 2.27 that accounts for the emissive terms corresponding to the inside and outside of the hollow cathode. For the term involving radiation on the exterior of the cathode with the environment, the black body radiation term will simply need to be multiplied by the outer emissivity to change the form in Equation 2.27 as shown in 2.28.

$$\sigma \frac{D_o}{D_x} (T_w^4(x) - T_\infty^4) \quad \Rightarrow \quad \epsilon_o \sigma \frac{D_o}{D_x} (T_w^4(x) - \epsilon_\infty T_\infty^4) \tag{2.28}$$

where ε_o is the emissivity on the outside of the cathode and ε_∞ and T_∞ are the emissivity and temperature of the environment.

For simplicity sake, the ends will still be assumed to be black bodies. A procedure outlined by Siegel is used to determine the radiation between finite diffuse gray areas [35]. This will give the influence of the gray surfaces on the inside of the cathode.

Equation 2.27 will now be represented in the form that states that the heat flux without the internal radiation terms equals the difference in radiation heat flux leaving the surface and impacting the internal surface. This is shown by:

$$q_k \pi D_x dx = (q_{ex,k} - q_{inc,k}) \pi D_x dx \quad (2.29)$$

In Equation 2.29 the subscript k refers to the kth surface (differential ring element). Note that $\pi D_x dx$ can be divided out. The terms that correspond to the heat flux without the internal radiation, q_k , are given as:

$$q_k(x) = K_w \frac{D_o^2 - D_x^2}{4D_x} \frac{dT_w}{dx^2} + \frac{I_{CE}^2 \rho}{\pi^2 D_x \frac{D_o^2 - D_x^2}{4}} + J_i \left(V_{fall} + \frac{5kT_i}{2e} + U_+ - \phi \right) + J_e \left(\frac{5kT_e}{2e} + \phi \right) - \varepsilon_o \sigma \frac{D_o}{D_x} (T_w^4(x) - \varepsilon_\infty T_\infty^4) - h \left[T_w(x) - St e^{-St x} \int_{z=0}^l e^{St z} T_w(z) dz + e^{-St x} T_{g,i} \right] - J_{th} \left(\phi_{eff} + \frac{5kT_w}{2e} \right) \quad (2.30)$$

Siegel then goes on to show that the radiation leaving the surface is:

$$q_{ex,k}(x) = \mathbf{s} T_{w,k}^4(x) - \frac{1 - \mathbf{e}_{in}(x)}{\mathbf{e}_{in}(x)} q_k(x) \quad (2.31)$$

which then makes the incoming radiation for the problem with the tube to be:

$$q_{inc,k}(x) = \int_{z=0}^l q_{ex,k}(z) dF_{dx-dz}(|x-z|) + \mathbf{s} T_{r,1}^4(x) F_{dx-1}(x) + \mathbf{s} T_{r,2}^4(x) F_{dx-2}(l-x) \quad (2.32)$$

where the terms represent the radiation from the rest of the tube and the ends.

So substituting Equation 2.31 and 2.32 into Equation 2.29 gives the energy balance for a gray body tube and is given in Equation 2.33.

$$\begin{aligned}
 q_k(x) + e_{in}(x) \int_{z=0}^l \frac{1 - e_{in}(z)}{e_{in}(z)} q_k(z) dF_{dx-dz}(|x-z|) &= e_{in}(x) \mathbf{s} T_{w,k}^4(x) \\
 - e_{in}(x) \int_{z=0}^l \mathbf{s} T_{w,k}^4(z) dF_{dx-dz}(|x-z|) - e_{in}(x) \mathbf{s} T_{r,1}^4(x) F_{dx-1}(x) - e_{in}(x) \mathbf{s} T_{r,2}^4(x) F_{dx-2}(l-x) &
 \end{aligned} \quad . \quad (2.33)$$

The method for solving Equation 2.33 is described in Appendix B.

2.2 Discharge Chamber

Once the cathode produces the electrons, they are ejected into the discharge chamber after interaction with plasma in the orifice of the cathode. A number of hollow cathodes use keepers. The keeper is generally a number of volts above the cathode and millimeters from the cathode tip. In the discharge chamber, one of its primary purposes is to protect the cathode from particles streaming back to the cathode. However, for the neutralizer it is used to extract current necessary to sustain emission. In order to determine the power from the charged particles on the different thruster surfaces, it is important to know what potential the various surfaces are. Figure 2.3 shows the typical potentials of an ion thruster.

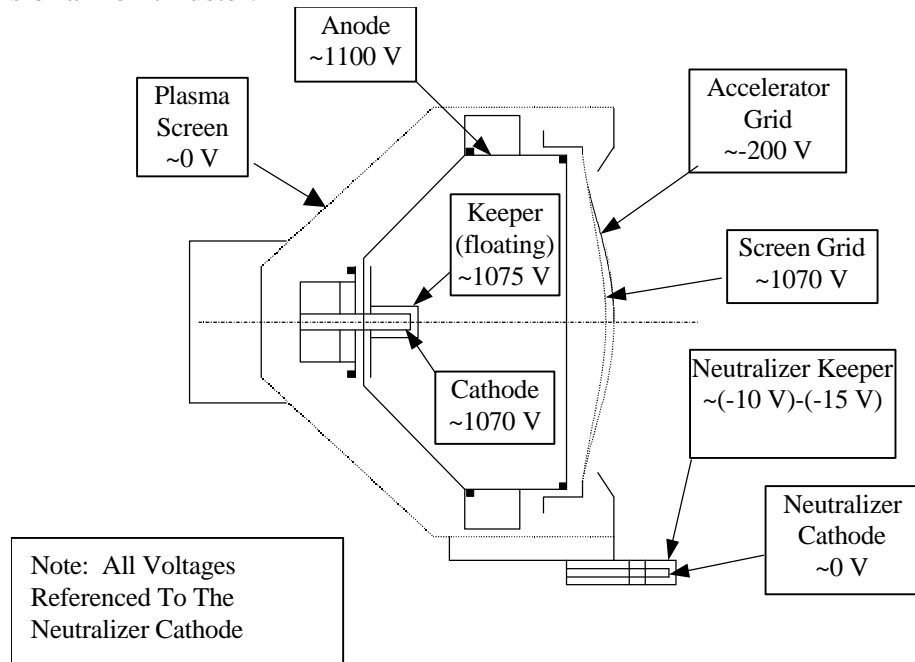


Figure 2.3. Potentials on an Ion Thruster

The main keeper receives energy from the ions that are born in the discharge chamber and from cathode electrons, which balance the current from the ions and some additional electrons that are lost through the keeper current. The neutralizer keeper does not have any significant ion heating, but the electron heating is significant since the keeper must draw a much higher current to sustain emission.

Once the electrons in the discharge chamber pass by the keeper, they either are involved in collisions or are collected directly by the anode. The primary electrons are collisionless and deposit all of the energy on the anode that results from passing through the potential difference between the cathode region and the anode. The electrons involved in the collisions form a Maxwellian distribution. The Maxwellian electrons are in the plasma, which is a few volts positive of the anode [41].

The ions created in the plasma will be drawn out in the beam or will deposit their energy into the various surfaces. The ions not drawn out in the beam will migrate more to the lower potential surfaces of the screen grid or the main cathode keeper. However, some will also travel to the anode. The ions that interact with the accelerator grid are created in the immediate vicinity of the grid from charge exchange or acceleration of some downstream electrons towards the grids [46]. The ions from the discharge chamber have significant energy and tend to be accelerated out of the thruster and not to the accelerator grid.

The effect of radiation from the plasma can be determined in the same manner as it was for the cathode. The temperature of the plasma in the discharge chamber is 2-5 eV (23,000-58,000 K) [60]. The ion and electron density is around 1×10^{11} per cubic centimeter [60]. Using Equation 2.10 the minimum radius for black body radiation to be considered is 1.9×10^{16} cm. Since the diameter of these thrusters is around 30 cm, there clearly will be minimal effect from black body radiation. Equation 2.11 is used to find the power from Bremsstrahlung radiation. Assuming singly and doubly ionized plasma, the maximum radiation occurs when the plasma is entirely doubly ionized. This would result

in a power of about $9.6 \times 10^{-10} \text{ W/cm}^3$. A discharge chamber having a volume of approximately 4000 cm^3 results in a power of $3.8 \times 10^{-6} \text{ W}$ deposited to the walls. This is also an insignificant amount of power to consider.

The power deposited into the different surfaces will then be found similarly to the terms that handle the charged particle interaction in the cathode model. The power is related to the current of the particles and the kinetic and potential energy they have. The surfaces will be broken down as the anode, the keeper, the screen grid, and the accelerator grid.

2.2.1 Power Deposition Equations

2.2.1.1 Anode

The power deposited into the anode comes from the primary electrons, Maxwellian electrons, and the ions. The power from the primary electrons is determined by the change in potential from where the electrons were born to the anode and the energy absorbed onto the surface. This power is described in Equation 2.34.

$$I_L (\phi_A + [V_D - V_C]) \quad (2.34)$$

I_L is the primary electron current to the anode. ϕ_A is the work function of the anode. V_D is the discharge voltage, which is the potential difference between the cathode and the anode. V_C is the potential relative to the cathode at which the primary electrons are produced. Vaughn [61] suggests V_C to be equal to the keeper potential, V_K , when it would more accurately be described by subtracting off the keeper sheath potential as shown in Equation 2.35.

$$V_C = V_K - V_{FK} \quad (2.35)$$

The electrons, which have undergone collisions, take a Maxwellian velocity distribution. The power that these electrons deposit into the anode is determined by their

kinetic energy. This is depicted in Equation 2.36 with a Maxwellian electron current to the anode (I_M).

$$I_M \left(\phi_A + \frac{5}{2} \frac{kT_e}{e} \right) \quad (2.36)$$

The power from the ions comes from their initial kinetic energy, their acceleration through the anode sheath, and the release of the ionization energy when they take an electron off the surface. This power is accounted for in Equation 2.37 for an ion current to the anode of I_A .

$$I_A \left(V_A + \frac{5}{2} \frac{kT_i}{e} + U_+ - \phi_A \right) \quad (2.37)$$

2.2.1.2 Keeper

The power from the ions in the discharge chamber to the main keeper is going to be of the same form as the ions to the anode. However, the ions are going to pass through a much larger potential. The plasma potential is relatively constant throughout the discharge chamber and is a few volts positive of the anode. Wells *et al.* describe the potential of the sheath on cathode potential surfaces as the difference between the plasma potential and cathode potential [38]. For an ion current to the keeper of I_K , the power is given by:

$$I_K \left(V_{DCFK} + \frac{5}{2} \frac{kT_i}{e} + U_+ - \phi_K \right) \quad (2.38)$$

where the fall the ions experience will be:

$$V_{DCFK} = V_P - V_K = V_D + V_A - V_K. \quad (2.39)$$

The electrons, which will intercept the keeper, are going to be accelerated from the region close to the orifice. Most of the electrons leaving the cathode are not produced by thermionic emission, but rather through secondary processes in the orifice region of the cathode where the density of the gas and charged particles will be quite high. Therefore,

the fall these electrons see is not going to be from the cathode potential, but from a potential closer to the keeper. The equation depicting the power is given in 2.40.

$$I_{EK} \left(V_{FK} + \frac{5}{2} \frac{kT_e}{e} + \phi_K \right) \quad (2.40)$$

The electron temperature is going to be highly dependent on the operation of the cathode. There are three operating modes of a hollow cathode: spot, plume and transition mode. In spot mode operation, the portion of the plume is only luminous in the immediate vicinity of the orifice and the electron temperatures are on the order of 0.5 eV. In plume mode, there is a luminous plume extending further out from the cathode orifice and electron temperatures are found to be 1.5-2.5 eV. The transition mode alternates between dark and luminous plumes [17]. The modes will have a significant effect on the energy deposited into the keeper since the electron temperature can vary so much. The neutralizer cathode tends to operate in spot mode and the main cathode operates in plume mode.

2.2.1.3 Screen Grid

The power deposited on the screen grid is primarily from the ions that are accelerated with the beam ions, but impact the grid instead of being extracted. The power follows that same form as the other surfaces and is given in Equation 2.41.

$$I_{SG} \left(V_{FSG} + \frac{5}{2} \frac{kT_i}{e} + U_+ - \phi_{SG} \right) \quad (2.41)$$

where I_{SG} is the ion current to the screen grid.

The fall to the screen grid is similar to the fall to the keeper. It will be the difference between the plasma potential and the screen grid potential.

$$V_{FSG} = V_P - V_{SG} \quad (2.42)$$

2.2.1.4 Accelerator Grid

The power to the accelerator grid is of the same type as the screen grid. Hence, the power equation looks the same as it does in Equation 2.43 for an ion current to the accelerator grid of I_{AG} .

$$I_{AG} \left(V_{FAG} + \frac{5}{2} \frac{kT_{ia}}{e} + U_+ - \phi_{AG} \right) \quad (2.43)$$

The major difference in the power deposited to the accelerator grid is based on where the ions are created. Since most of the ions are created in the immediate vicinity of the accelerator grid, they cannot be characterized by the ions in the discharge chamber. Monheiser showed that there is a potential hill downstream of the grids at a couple hundred volts [46]. Thus, it can be assumed that the fall is around this value.

2.2.2 Currents

In order to determine the power to various thruster surfaces, it is important to predict the amount of charged particles that are traveling to each surface. Several of these currents can be calculated through continuity. The discharge current, I_D , is the current that goes through the anode of the discharge chamber. It is equal to I_E , which is the amount of electrons being emitted from the cathode, but not collected by the keeper, plus the electrons knocked off for each ion produced, I_P , minus each electron lost from an ion recombining on the anode surface, I_A . This is summed up in Equation 2.44.

$$I_D = I_E + I_P - I_A \quad (2.44)$$

Each ion that is produced, I_P , will either go out in the beam, I_B , recombine on a cathode potential surface in the thruster, I_C , or recombine on an anode potential surface, I_A . So the ion production current can be described by Equation 2.45.

$$I_P = I_B + I_C + I_A \quad (2.45)$$

Substituting Equation 2.45 into 2.44 gives the ion current to the cathode in terms of the discharge current and beam current, which are readily available for most operating thrusters. The ion current to the cathode is then given in Equation 2.46.

$$I_C = I_D - (I_E + I_B) \quad (2.46)$$

The ion current to cathode potential surfaces is defined as the ion current to the screen grid and the cathode keeper. Although the cathode keeper is not at the same potential as the cathode, it is significantly negative with respect to the plasma and as such is included in the cathode potential surfaces.

$$I_C = I_K + I_{SG} \quad (2.47)$$

The ion current to the screen grid can be found by biasing the grids sufficiently negative to repel electrons and then can be measured directly. The relationship between the ion current to the screen grid and the beam current is usually summed up by the ratio of beam current over the beam current plus the screen grid ion current as shown in Equation 2.48.

$$\alpha = \frac{I_B}{I_B + I_{SG}} \quad (2.48)$$

The accelerating grid current, I_{AG} , is also determined directly from measurements.

The electron current to the keeper from the cathode, I_{EK} , is a sum of the current from the ions collecting an electron from the surface and the current leaving the keeper through a resistor. If the current through the resistor isn't directly available it can be determined using the voltage/resistance relation. The net electron current to the keeper would be:

$$I_{EK} = I_K + \frac{V_K(\text{across resistor})}{R(\text{resistance})} \quad (2.49)$$

The ion current to anode potential surfaces can be found by rearranging Equations 2.44 or 2.45. The ion production current is derived from a definition given by Brophy [41]. He defines the ratio of the beam current to the ion production current as the

extracted ion fraction, f_B . The extracted ion fraction is considered constant for a thruster design and shows the performance of a thruster. The ion production current is given in terms of the beam current in Equation 2.50.

$$I_p = \frac{I_B}{f_B} \quad (2.50)$$

In order to predict the various currents, the primary electron current emitted from the cathode into the discharge chamber, I_E , must be derived. Each primary electron that is emitted from the cathode and continues beyond the keeper will either be collected directly by the anode, I_L , ionize a neutral atom, I'_p , or excite a neutral atom, I'_{ex} . This balance is shown in Equation 2.51.

$$I_E = I_L + I'_p + I'_{ex} \quad (2.51)$$

The fraction of primary electrons which are emitted and make it to the anode without a collision can be given by the survival equation [62] and written in the form:

$$I_L = I_E \exp^{-\sigma'_o n_o l_e} \quad (2.52)$$

where σ'_o is the total inelastic cross section for primary electron-neutral atom collisions, n_o is the neutral atom density, and l_e is the average length a primary electron would travel in the discharge chamber before it would be collected by the anode with the assumption of no inelastic collisions.

The ion current produced from primary electrons is given by:

$$I'_p = n_o n_p e v_p V_{ipr} \sigma'_+ \quad (2.53)$$

where n_p is the primary electron density, e is the charge of an electron, σ'_+ is the ionization cross section at the primary electron energy, V_{ipr} is the volume of the ion production region, and v_p is the primary electron velocity [41].

Likewise, the rate of production of excited state atoms produced by primary electrons is given in Equation 2.54.

$$I'_{ex} = n_o n_p e v_p V_{ipr} \sum_j \sigma'_j \quad (2.54)$$

with σ'_j being the collision cross section for the j^{th} excited state at the primary electron energy [41].

The emission current is then found by substituting Equations 2.52-2.54 into Equation 2.51. The emission current can then be written as:

$$I_E (1 - \exp^{-\sigma'_o n_o l_e}) = n_o n_p e v_p V_{ipr} \left(\sigma'_+ + \sum_j \sigma'_j \right) \quad (2.55)$$

Since $\sigma'_+ + \sum_j \sigma'_j$ is the total inelastic cross section for primary electron-neutral atom collisions, Equation 2.55 can be rewritten to give the emission current in Equation 2.56.

$$I_E = \frac{n_o n_p e v_p V_{ipr} \sigma'_o}{1 - \exp^{-\sigma'_o n_o l_e}} \quad (2.56)$$

The discharge current, I_D , is made up of three components. One component is the current from the primary electrons collecting on the anode, I_L , which can be found using Equations 2.52 and 2.56. Another component is the current from the ions taking electrons from the anode, I_A , and can be determined using Equations 2.44, 2.50, and 2.56. The final component is the current from the Maxwellian electrons, I_M . This current can be calculated from a balance of the currents to the anode. It can be written to solve for I_M to be:

$$I_M = I_D + I_A - I_L \quad (2.57)$$

2.2.3 Discharge Chamber and Plasma Parameters

To predict the power deposited in the discharge chamber of the ion thruster, it will be important to predict the plasma characteristics from set thruster parameters. The equations for the charged particle currents in the thruster have been derived from several of these plasma and thruster parameters. Another important parameter to predict will be

the temperature of the Maxwellian electrons. These electrons account for significant power loss to the anode.

2.2.3.1 Neutral, Ion, and Electron Densities

Several of the currents are dependent on knowing the densities present in the discharge chamber. The propellant and electrons are present in four different total densities: neutral density, ion density, primary electron density, and Maxwellian electron density. The densities can be derived using Brophy's ion thruster performance model [41]. The average ion density (n_i) related to the beam current (I_B), the Bohm velocity (v_b), the area of the grids from which ions are extracted (A_g), and the transparency of the screen grid to ions (Φ_i). This relation is given as:

$$n_i = \frac{I_B}{0.6ev_b A_g \Phi_i} \quad . \quad (2.58)$$

The ratio of the primary electron density (n_p) to the Maxwellian electron density (n_M) is related to the Maxwellian electron rate factor for the ionization of neutral atoms (Q_o^+), the primary electron velocity (v_p), and the baseline plasma ion energy costs (ϵ_p^*). This is described in Equation 2.59.

$$\frac{n_p}{n_M} = \frac{Q_o^+}{\frac{v_p V_D \sigma'_o}{\epsilon_p^*} - \sigma'_+ v_p} \quad (2.59)$$

The Maxwellian electron density can be found from the assumption of quasi-neutrality ($n_i = n_M + n_p$). This can be rearranged to give the Maxwellian electron density:

$$n_M = \frac{n_i}{\left(1 + \frac{n_p}{n_M}\right)} \quad . \quad (2.60)$$

With the ion density and Maxwellian electron density derived, the primary electron density can be determined directly from the quasi-neutrality assumption.

Brophy derives the neutral density using the theory of free molecular flow through a sharp-edged orifice to be:

$$n_o = \frac{4(\dot{m} - I_B)}{ev_o A_g \Phi_o} \quad (2.61)$$

where \dot{m} is the mass flow rate, v_o is the neutral atom velocity, and Φ_o is the effective transparency of grids to neutrals.

2.2.3.2 Maxwellian Electron Rate Factor For Ionization of Neutral Atoms

Predicting the Maxwellian electron temperature will have to be through an iterative method. This iteration will be accomplished using the Maxwellian electron rate factor for ionization of neutral atoms, Q_o^+ , that Brophy defines as [41]:

$$Q_o^+ = \langle \sigma_{+v_e} \rangle_M \quad (2.62)$$

The symbol $\langle \rangle_M$ represents the enclosed product averaged over the Maxwellian energy distribution function which for a given collision cross section is given by Equation 2.63.

$$\langle \sigma_{+(or\ ex)} v_e \rangle_M = \frac{\int_0^{\infty} \sigma_{+(or\ ex)} v_e F(v_e) dv_e}{\int_0^{\infty} F(v_e) dv_e} \quad (2.63)$$

Where in Equation 2.63, v_e is the electron speed and $F(v_e)$ is the Maxwell-Boltzmann distribution, which is given by:

$$F(v_e) = 4\pi v_e^2 \left[\frac{m_e}{2\pi k T_M} \right]^{3/2} \exp \left(-\frac{m_e v_e^2}{2k T_M} \right) \quad (2.64)$$

This establishes a relation for Q_o^+ that is based solely on a particular gas and the Maxwellian electron temperature. This relationship is shown for xenon in Figure 2.4.

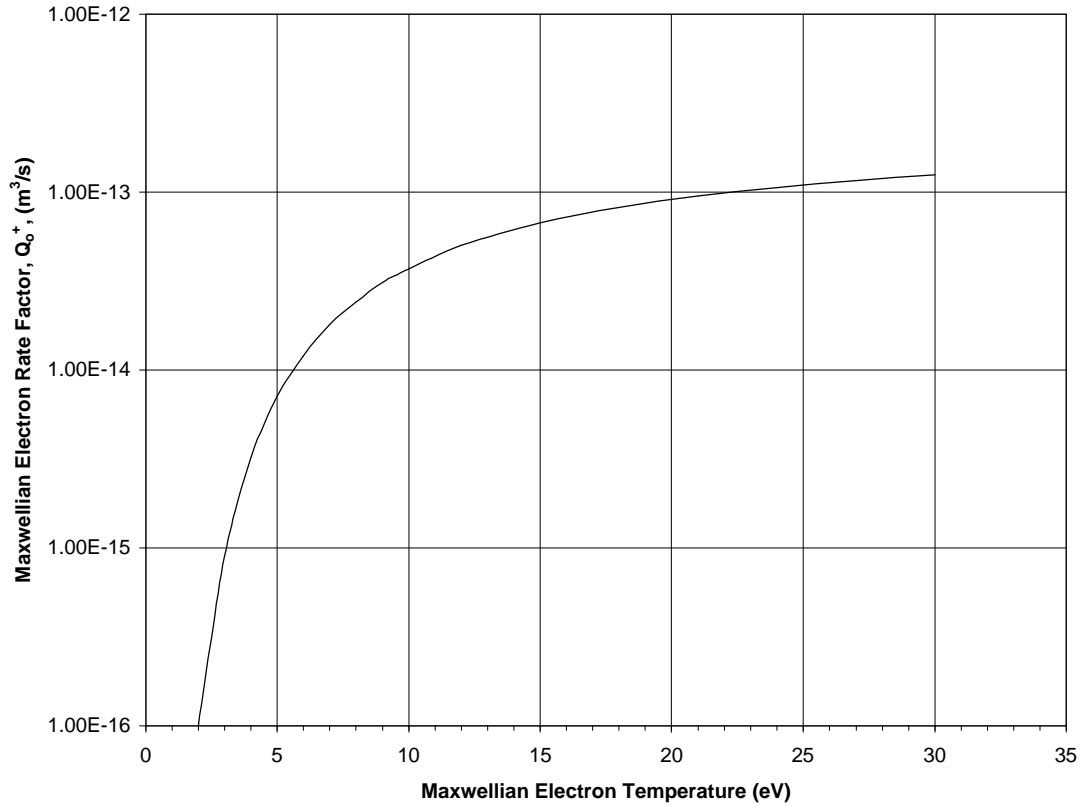


Figure 2.4. Maxwellian Electron Rate Factor for Xenon

Brophy also determines Q_o^+ in terms of the thruster and plasma parameters. The rate factor in these terms is shown in Equation 2.65.

$$Q_o^+ = \frac{v_p \sigma'_+ \left(\frac{V_D \sigma'_o}{\epsilon_p^* \sigma'_+} - 1 \right)}{\left[\frac{v_p V_D \sigma'_o f_B V_{ipr}}{0.15 \epsilon_p^* v_o v_b A_g^2 \Phi_o \Phi_i} \right] \dot{m} \left(1 - \frac{I_B}{\dot{m}} \right) - 1} \quad (2.65)$$

Equation 2.65 has the Maxwellian electron temperature included when deriving the thruster efficiency term, the baseline plasma ion energy cost - ϵ_p^* , and will be shown in Section 2.2.3.4.

2.2.3.3 Particle Velocities

The primary electron velocity, v_p , is determined by the primary electron energy, V_{PE} , attained by an electron accelerated from the cathode. This is given by the relation shown in Equation 2.66 where the temperature, T , is in degrees Kelvin and is related to the electron temperature, which for primary electrons is equal to the primary electron energy (V_{PE}), by the relation of $1\text{eV}=11,600^\circ\text{K}$.

$$v_p = \sqrt{\frac{kT}{m_e}} \quad (2.66)$$

The primary electron energy is determined by the difference in potential between the plasma from where the electron is born near the cathode to the plasma in the discharge chamber. The plasma in the discharge chamber is a few volts above the discharge voltage. The plasma near the cathode is going to be a few volts below the keeper. The respective sheath potentials are used for the differences in the plasma from the anode potential. The primary electron energy can then be described as:

$$V_{PE} = V_D + V_A - V_K + V_{FK} \quad (2.67)$$

The Bohm and neutral velocity can also be found by using Equation 2.66 except the neutral velocity uses the mass of a neutral atom. The temperature used for the Bohm velocity is equal to the Maxwellian electron temperature. Ions must enter the sheath with this speed [59]. The neutral temperature is determined by the anode wall temperature.

2.2.3.4 Baseline Plasma Ion Energy Cost

In order to calculate the Maxwellian electron rate factor it is necessary to know the baseline plasma ion energy cost, ϵ_p^* . Brophy derives two equations for computing this cost [41]. The first equation for the baseline plasma ion energy cost is given by Equation 2.68.

$$\epsilon_p^* = \frac{U_+ + \epsilon_M + \frac{\left[\frac{n_p}{n_m} \sigma'_{ex} v_p + \langle \sigma_{ex} v_e \rangle_M \right] U_{ex}}{\frac{n_p}{n_m} \sigma'_+ v_p + \langle \sigma_+ v_e \rangle_M}}{1 - \frac{(V_K - V_{FK} + \epsilon_M)}{V_D}} \quad (2.68)$$

For a particular thruster the main unknowns in Equation 2.68 are the ratio of primary to Maxwellian electron density, n_p/n_m , and the average energy of Maxwellian electrons leaving the plasma at the anode, ϵ_M . Brophy gives ϵ_M as:

$$\epsilon_M = \frac{4}{3} T_M + V_A \quad (2.69)$$

The electron density ratio is handled by deriving another form of ϵ_p^* . This is now given in the form of Equation 2.70.

$$\epsilon_p^* = \frac{V_D \frac{\sigma'_o}{\sigma'_+}}{1 + \frac{n_m \langle \sigma_+ v_e \rangle_M}{n_p \sigma'_+ v_p}} \quad (2.70)$$

Equation 2.70 is then rearranged and substituted into Equation 2.68 to give the baseline plasma ion energy cost in Equation 2.71 without a dependence on the electron density ratios.

$$\epsilon_p^* = \frac{U_+ + \epsilon_M + \frac{\langle \sigma_{ex} v_e \rangle_M}{\langle \sigma_+ v_e \rangle_M} U_{ex}}{1 - \frac{V_K - V_{FK} + \epsilon_M}{V_D} + \left[\frac{\sigma'_o \langle \sigma_{ex} v_e \rangle_M}{V_D \sigma'_o \langle \sigma_+ v_e \rangle_M} - \frac{\sigma'_{ex}}{V_D \sigma'_o} \right] U_{ex}} \quad (2.71)$$

2.2.3.5 Maxwellian Electron Temperature

The Maxwellian electron temperature can be found by an iterative method. An estimate of the electron temperature can be used to find ϵ_M in Equation 2.69. ϵ_M can then be substituted into ϵ_p^* in Equation 2.71. ϵ_p^* next will be used to find the Maxwellian electron rate factor in Equation 2.65. That value of Q_o^+ can then be used in the relationship in Equation 2.62, which is shown in Figure 2.4, to determine a new Maxwellian electron temperature. The new T_M can be used to find a new ϵ_M and repeat

the process. After a few iterations, the Maxwellian electron temperature will settle on the appropriate value.

2.3 Power Deposition Equation Derivation Conclusion

The equations have now been derived to predict the plasma power deposition in the cathode and anode from minimal experimental input. The cathode model consists of an integral-differential equation that is solved through a numerical method outlined in Appendix B. The discharge chamber model uses currents that are measured during a typical operation to predict the power deposited to the anode, keeper, and grids. The results from these equations can now be compared to previous work.

CHAPTER III

COMPARISON OF ANALYTICAL results to previous work

Before the model derived in Chapter II can be applied to new cases, it is important first to apply it to previously obtained data. The cathode and the rest of the thruster have frequently been examined separately. The cathode will be compared to dissertation work done by Salhi [29]. While there is minimal power deposition data for comparison, there are cathode temperature profiles available. The effect of changing several model parameters will be examined to see their effect on the predicted temperature profiles compared to the experimentally determined profiles.

For the rest of the thruster, there is also a significant amount of temperature data available for various thrusters. However, there is much less work done on power deposition and particle interaction with surfaces. Wells *et al.* have done such work in determining the losses due to the charged particles interacting with the surfaces [38]. This thruster was a 15-cm diameter, mercury, divergent-field ion thruster. This thruster is slightly different from what the model was designed for, but will demonstrate the model's versatility while verifying its results.

3.1 Cathode

3.1.1 Solution Method

For validating the results of solving Equation 2.33, experimental results were examined as reported by Salhi [29]. Salhi measured several of the plasma characteristics in the hollow cathode that are needed for evaluation of Equation 2.33. These include the electron number density, plasma potential, electron temperature, cathode wall

temperature, and cathode setup. The plasma characteristics measured were along the centerline of the cathode. This may cause some variation with the values to be used in Equation 2.33 since the sheath region is where the values of concern are. However, these differences can be examined in the following section.

To determine the best correlation of the emission current, ion current, electron current and the heat flux to the cathode, several parameters, which have a degree of uncertainty, will be varied to determine which are the most sensitive in the analysis and which give the best fit to experiments. The parameters that will be varied will be the plasma density, the work function of the material, the ohmic heating along the cathode wall from the current, the convection, the conductivity and the emissivity. Then the resulting temperature profiles and emission currents will be compared to experimental data.

It should be noted that the temperatures are expected to be slightly different from the experimental data. Salhi reports the outer wall temperatures and Equation 2.33 predicts the inner wall temperatures, which include the insert. Salhi did test the internal temperatures of the cathode using a pyrometer along with external thermocouples. He surmised that there was not much difference between these two temperatures and his data show the internal temperatures being a maximum of 50° C warmer than the exterior. However, the temperature difference could easily be larger. It can be difficult to calibrate an optical temperature-measuring device since it is dependent on knowing the surface characteristics accurately.

The insert is slightly smaller than the inner wall of the cathode tube. This results in a slightly loose fit. The contact resistance will then be very high and radiation will be a predominant mechanism for transferring heat from the insert to the outer cathode wall. The approximate radiation heat transfer between two closely spaced cylinders is given in Equation 3.1.

$$q = \epsilon T_{insert}^4 - \epsilon T_{outer\ wall}^4 \quad (3.1)$$

As will be seen the heat flux is around 20 W, which needs to be transferred from the insert. The insert surface area is approximately $3.51 \times 10^{-4} \text{ m}^2$. The value for Stephan-Boltzman's constant is $5.669 \times 10^{-8} \text{ W/m}^2\text{K}^4$. This would result in a relation of the temperatures to be:

$$T_{insert} = (1 \times 10^{12} + T_{outer\ wall}^4)^{1/4} \quad (3.2)$$

For an outer wall temperature of 1050°C (1323°K) this would predict the insert temperature to be 1147°C , a net change of about 100°C . If the outer wall was measured to be 848°C and the heat flux was around 18 W the insert temperature would be 982°C , a net difference of 130°C . This is supported by Mirtich *et al.* [32] who reported that with a tip temperature of 940°C the insert was measured to be 1060°C , a difference of 120°C .

The temperature of the insert would then be expected to be $100\text{-}130^\circ\text{C}$ warmer than the thermocouple values on the outer wall with a greater difference at the lower emission currents (cooler tip). The insert region extends 2.54 cm from the tip. The region outside of the insert region will have temperatures close to the outer surface thermocouple temperatures since the cathode wall is thin and does not have any other object between it and the plasma.

3.1.2 Varying Cathode Parameters

3.1.2.1 Plasma Density

In the evaluation of the plasma, the number density is the most influential value determining the resulting currents and heat fluxes. Salhi showed the number density for an emission current of 5 A to be about half of the density present for the 10 A emission current. The other major variables for determining the currents and fluxes from the plasma, which Salhi measured, were the electron temperature and the plasma potential.

These vary such that for an emission current of 4 A the electron temperature is 1.5 eV and the plasma potential is 14 V. Then for an emission current of 15 A the electron temperature is 1.2 eV and the plasma potential is 8 V in the first few millimeters of the cathode tip.

For the current from the ionic recombination, the square root of the electron temperature is used, but the full value of density is used (Equation 2.23). Therefore, with changes of each for different emission currents, the density variation results in the most significant changes. The electron backstreaming will be shown to be insignificant for determining the emission current and heat flux. The thermionic current is most affected by wall temperatures, but a change in most of the plasma characteristics will have a small effect on changing the electric field present and hence the temperature. However, the change in plasma density plays the major role in changing the electric field.

The approach for evaluating the emission current was developed to vary only the plasma density present. This approach was used because of the uncertainty of the actual values. There is about a 50% degree of uncertainty in measuring the density. Also, the values from the experiment are *centerline* values and not *sheath* values.

A comparison was done for two cases which predicted 5 A emission currents. The first case used the plasma characteristics from the 12 A experiments and then scaled the density until a 5 A emission current was attained (resulting density was 42% of 12 A reported values). The second case used the 5 A experimental data and scaled the density until an emission current of 5 A was predicted. The 5 A case was “scaled” because the emission current predicted was slightly higher than 5 A and there is a high degree of uncertainty in the density values as previously mentioned (resulting density was 94% of 5 A reported values). Table 3-1 shows the result of this.

The difference in the energetic electron current between the two cases in Table 3-1 is a result of only the density being scaled and not the voltage fall. This has a dramatic effect on the energetic electron current since it is dependent on the exponential of the

voltage fall. However, since in either case the energetic electron current (and power) is a couple of orders of magnitude less than the ion current (and power), the energetic electron current is insignificant. This lack of scaling has a lesser effect on the rest of the plasma/wall interaction terms and the resulting heat fluxes are within 0.5% of each other.

Table 3-1 Comparison of Two $I_{CE}=5$ A Predicted Cases by Varying Different Plasma Properties

	Plasma Initially 12 A Case	Plasma Initially 5 A Case
Percent Density Scaled	42%	94%
Final Density Used at 1 mm	$6.3 \times 10^{20} / \text{m}^3$	$4.7 \times 10^{20} / \text{m}^3$
Ion Current	1.37 A	1.23 A
Energetic Electron Current	0.043A	0.004 A
Thermionic Current	3.68 A	3.77 A
Emission Current	5.0 A	5.0 A
Heating from Ions and Energetic Electrons	28.7 W	28.8 W
Thermionic Electrons Cooling	8.2 W	8.4 W
Net Heat Flux	20.5 W	20.4 W

In order to evaluate the whole cathode, an assumption about the plasma density in the first millimeter had to be made. Salhi reports all the values up until this region. However, as will be shown, most of the heating and cooling from the plasma is occurring in the first few millimeters. To fit with temperature data reported by Salhi (and also Siegfried[30] and others) the plasma density was assumed to decrease in this front region from the 1 millimeter value to approximately the values between the 2nd and 3rd millimeter.

Figure 3.1 shows the temperature profiles for various plasma densities with a work function of 1.9 eV. The plasma properties were based on the experimental case where the emission current was 12 A. The properties used for each case represented in Figure 3.1 are given in Table 3-2. Figure 3.1 demonstrates that increasing the density increases the amount of energy deposited into the cathode, which increases the temperature and the

amount of thermionic current. The "kink" in the curve around the 2.5-cm mark is due to the change in wall area from the region with the insert to the region without it. The values from 0 to 2.6 cm include the thickness of the insert while from 2.6 to 3.8 they only include the thickness of the cathode wall outside of the insert region.

With a work function of 1.9 eV, the 47% density value returns an emission current of 10.1 A. This appears reasonable; however, the actual temperature most likely will be higher than Salhi's data corresponding to the emission current of 10 A, as mentioned previously. This will be examined as many of the parameters are varied.

3.1.2.2 Work Function

The work function of a cathode is given by Salhi [29] to be 1.8-2.0 eV for a tungsten insert impregnated with barium. The work function can change with temperature and time. This is the range reported by others also [30]. Thermionic currents are quite sensitive to small changes in the work function. Figure 3.2 shows cases where the work function was varied and the plasma density was adjusted to obtain a predicted emission current of 10 A. Table 3-3 gives the corresponding properties used in Figure 3.2.

As expected, with an increase in the work function, the necessary temperature needed to produce an emission current of 10 A increases. Figure 3.2 shows the sensitivity of the temperature to just a slight change in the work function. A one-tenth of an eV change in the work function affects the peak temperature by about 50°C. The work function of 1.9 eV fits Salhi's data the closest, but as discussed earlier, the insert temperature could be 100-130 °C warmer than the reported data. With that taken into consideration, a work function of 2.0 eV would be a more appropriate choice to represent the insert. A difference in one-tenth eV for the work function also changes the heat flux to the cathode by about 2 W. For the lower work function material, more of the current is derived from thermionic emission and less from the ionic recombination.

3.1.2.3 Ohmic Heating of Cathode

Figure 3.3 and Table 3-4 give the temperature profile and cathode data for cases in which the amount of Ohmic heating of the cathode wall is varied. There are multiple values given to show the effect the error in estimating the Ohmic heating might have on the temperatures of the cathode and the heat fluxes present. These values correspond to Equation 2.18. Using a resistivity of $8 \times 10^{-8} \Omega\text{-m}$ for Molybdenum, an emission current of 11.5 A and the dimensions of the cathode, the amount of heat generated per surface area of the cathode wall is 74 W/m^2 .

Figure 3.3 shows that for heat fluxes from 1 to 1000 W/m^2 the temperature barely changes. This shows that the effect of the Ohmic heating at the stated currents is minimal.

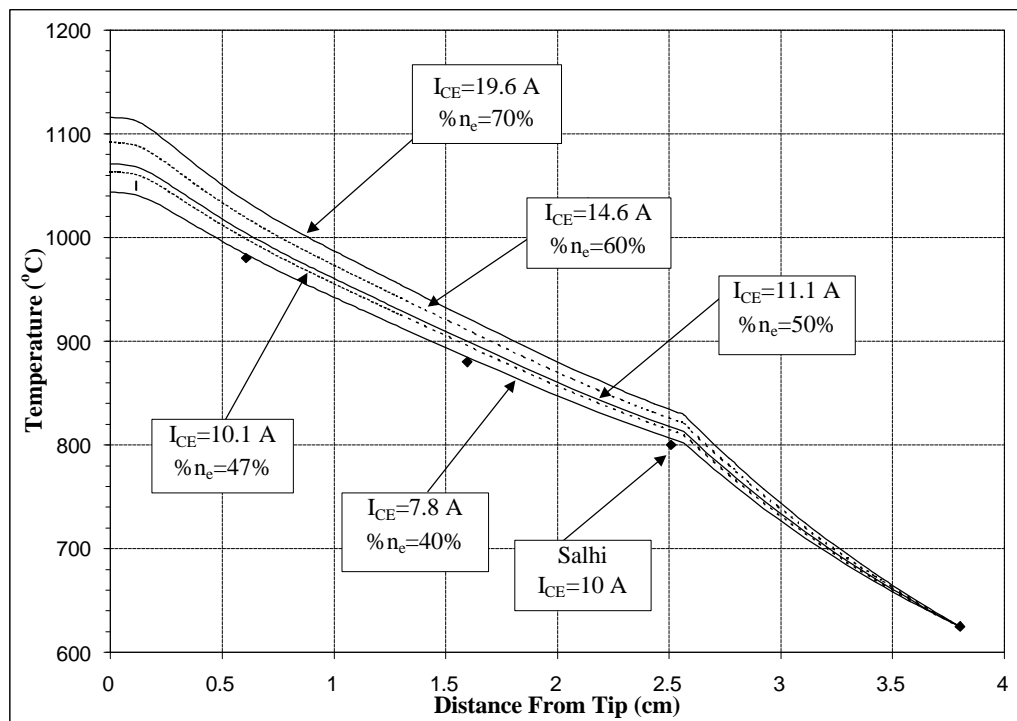
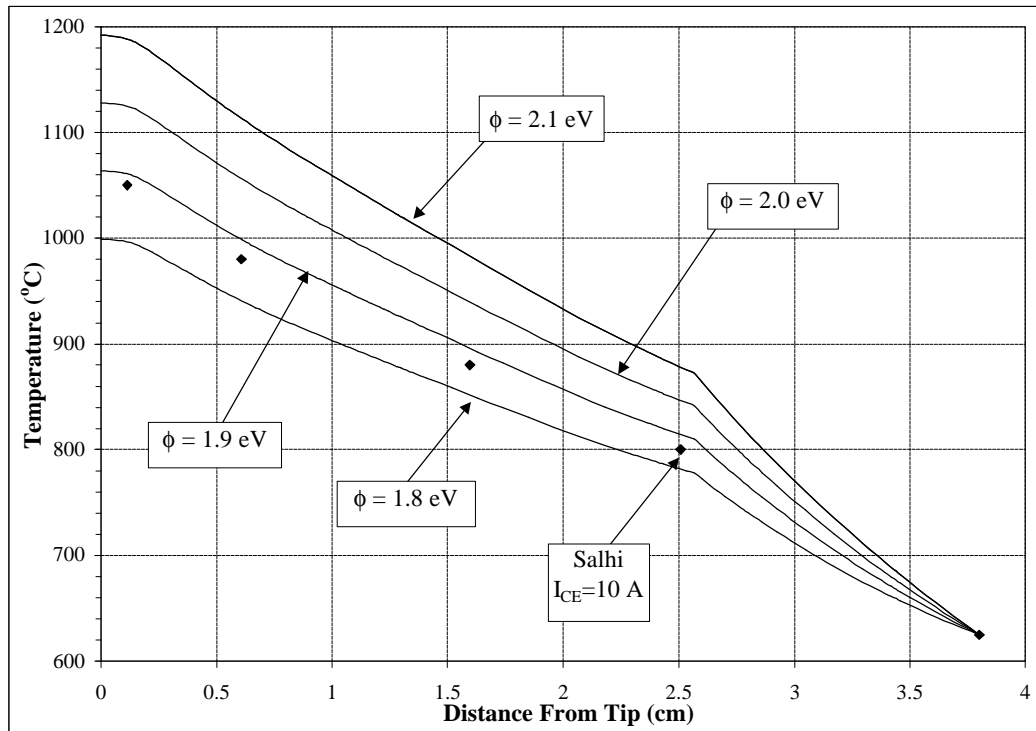


Figure 3.1. Cathode Temperatures for Varying Plasma Densities
(Salhi's Error $\pm 50^\circ\text{C}$)

Table 3-2 Cathode Properties Corresponding to Figure 3

	Case 1	Case 2	Case 3	Case 4	Case 5
Conductance, K_w , (W/m °C)	64	64	64	64	64
Inlet Gas Temp, $T_{g,i}$, (°C)	427	427	427	427	427
Convection Coefficient, h , (W/m ² °C)	21.8	21.8	21.8	21.8	21.8
Stanton Number, St	1.56	1.56	1.56	1.56	1.56
Ohmic Heating, q , (W/m ²)	100	100	100	100	100
Work Function, ϕ , (eV)	1.9	1.9	1.9	1.9	1.9
Outer Emissivity, ϵ_o	0.2	0.2	0.2	0.2	0.2
Inner Emissivity, ϵ_{in}	0.3	0.3	0.3	0.3	0.3
Percent of Ne for Id=12A	70	60	50	47	40
Ion Current, $\int J_i dA$, (A)	2.45	1.98	1.65	1.55	1.32
Energetic Electron Current, $\int J_e dA$, (A)	0.08	0.06	0.05	0.05	0.04
Thermionic Current, $\int J_{th} dA$, (A)	17.23	12.64	9.54	8.63	6.53
Total Current (Emission), I_{CE}, (A)	19.60	14.56	11.14	10.13	7.81
Energy from Ions and Electrons (W)	51.91	41.92	34.93	32.83	27.93
Thermionic Cooling (W)	36.39	26.69	20.14	18.22	13.79
Net Power Deposited (W)	15.52	15.23	14.79	14.61	14.14
Surrounding Temperature, T_∞ , (°C)	27	27	27	27	27
Tip Boundary Condition	insulated	insulated	insulated	insulated	insulated
Base Boundary Condition (°C)	625	625	625	625	625



**Figure 3.2. Cathode Temperature for Different Work Functions and $I_{CE}=10A$
(Salhi's Error $\pm 50^\circ C$)**

Table 3-3 Cathode Properties Corresponding to Figure 3.2

	Case 1	Case 2	Case 3	Case 4
Conductivity, K_w , (W/m °C)	64	64	64	64
Inlet Gas Temperature, $T_{g,i}$, (°C)	427	427	427	427
Convection Coefficient, h , (W/m ² °C)	21.8	21.8	21.8	21.8
Stanton Number, St	1.56	1.56	1.56	1.56
Ohmic Heating, q , (W/ m ²)	100	100	100	100
Work Function, ϕ, (eV)	2.1	2	1.9	1.8
Outer Emissivity, ϵ_o	0.2	0.2	0.2	0.2
Inner Emissivity, ϵ_{in}	0.3	0.3	0.3	0.3
Percent of Ne for Id=12A	55	51	47	43
Ion Current, $\int J_i dA$, (A)	1.82	1.69	1.55	1.42
Energetic Electron Current, $\int J_e dA$, (A)	0.06	0.05	0.05	0.04
Thermionic Current, $\int J_{th} dA$, (A)	8.38	8.50	8.63	8.75
Total Current (Emission), I_{CE} , (A)	10.14	10.14	10.13	10.13
Energy from Ions and Electrons (W)	38.11	35.48	32.83	30.15
Thermionic Cooling (W)	19.57	18.91	18.22	17.50
Net Power Deposited (W)	18.54	16.57	14.61	12.65
Surrounding Temperature, T_{∞} , (°C)	27	27	27	27
Tip Boundary Condition	insulated	insulated	insulated	insulated
Base Boundary Condition (°C)	625	625	625	625

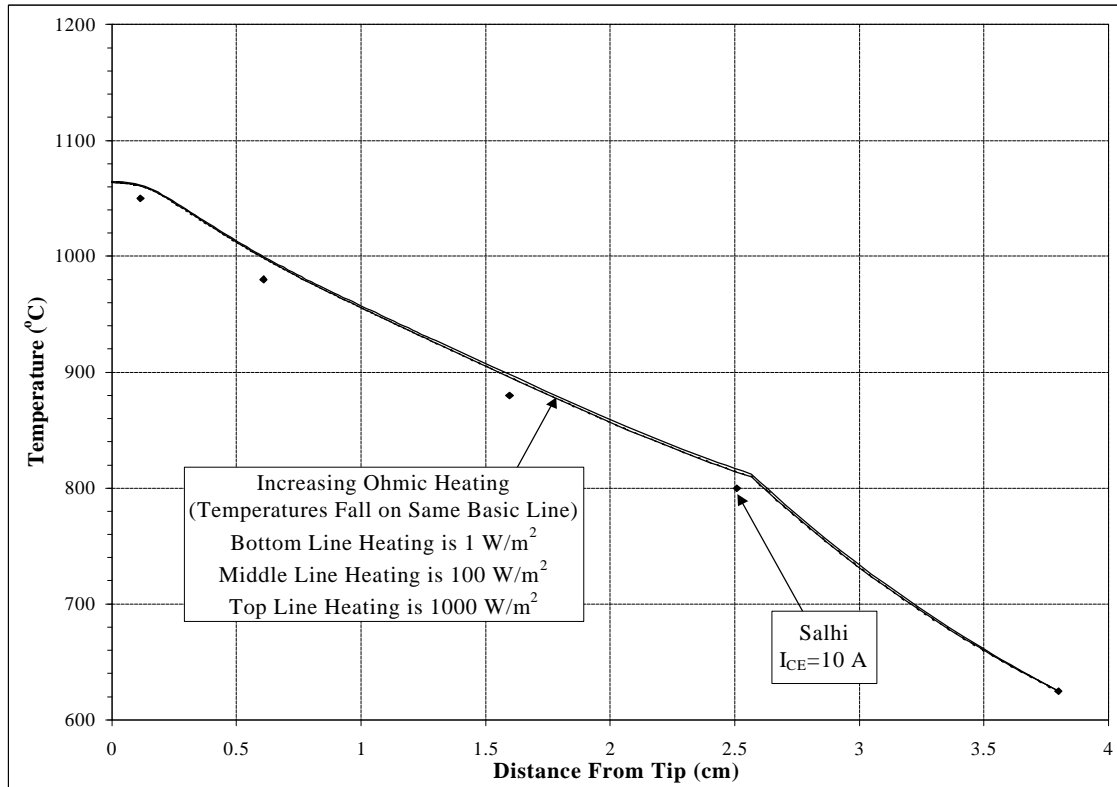


**Figure 3.3. Cathode Temperature Profile for Different Ohmic Heating Values
(Salhi's Error $\pm 50^\circ\text{C}$)**

Table 3-4 Cathode Properties Corresponding to Figure 3.3

	Case 1	Case 2	Case 3
Conductivity, K_w , (W/m °C)	64	64	64
Inlet Gas Temperature, $T_{g,i}$, (°C)	427	427	427
Convection Coefficient, h , (W/m ² °C)	21.8	21.8	21.8
Stanton Number, St	1.56	1.56	1.56
Ohmic Heating, q, (W/ m²)	1000	100	1
Work Function, ϕ , (eV)	1.9	1.9	1.9
Outer Emissivity, ϵ_o	0.2	0.2	0.2
Inner Emissivity, ϵ_{in}	0.3	0.3	0.3
Percent of Ne for Id=12A	47	47	47
Ion Current, $\int J_i dA$, (A)	1.55	1.55	1.55
Energetic Electron Current, $\int J_e dA$, (A)	0.05	0.05	0.05
Thermionic Current, $\int J_{th} dA$, (A)	8.73	8.63	8.61
Total Current (Emission), I_{CE} , (A)	10.23	10.13	10.11
Energy from Ions and Electrons (W)	32.83	32.83	32.83
Thermionic Cooling (W)	18.45	18.22	18.19
Net Power Deposited (W)	14.38	14.61	14.64
Surrounding Temperature, T_∞ , (°C)	27	27	27
Tip Boundary Condition	insulated	insulated	insulated
Base Boundary Condition (°C)	625	625	625

3.1.2.4 Convection

In order to determine the convection terms, the xenon gas was assumed to be a fully developed laminar flow. Because the mass flow rate is so low (1.27×10^{-3} g/sec in this case), the Reynold's number will be quite low also (~ 5) which is well in the laminar flow region. By using the conductivity of xenon gas and the diameter of the insert region, the convection coefficient for a cylinder is given for a uniform surface heat flux in a circular tube with laminar, fully developed conditions as [49]:

$$h = 4.36 \frac{K_g}{D} \approx 4.36 \frac{10.4 \times 10^{-3} \text{ W/m K}}{7.62 \times 10^{-3} \text{ m}} = 5.95 \text{ W/m}^2 \text{ K}$$

The Stanton Number can then be calculated using the relation:

$$St = \frac{h}{r_g u_\infty c_p} \approx \frac{5.95 \text{ W/m}^2 \text{ K}}{(0.111 \text{ kg/m}^2 \text{ s})(125.5 \text{ J/kg K})} = 0.427$$

Figure 3.4 shows the case where these values are used and cases with higher and lower values of the convection coefficient. For the case where $h=5.95$ was used and the inlet gas was estimated at $27\text{ }^{\circ}\text{C}$, the outlet gas was calculated to be $42\text{ }^{\circ}\text{C}$, which is $15\text{ }^{\circ}\text{C}$ warmer than the inlet temperature. This would support using the inlet gas temperature close to the value it would be at in storage (room temperature) since not much heating of the gas occurs.

When Case 4 on Table 3-5 ($h=5.95$) is compared to Case 3 ($h=0.39$) about 1.4 W more heat is required for the higher convection coefficient and the thermionic current is reduced by 0.6 A . This is a result of more energy being removed by convection and less available for thermionic emission. If the convection coefficient is dramatically higher as in Case 2 ($h=21.8$) it could have dramatic effects on the efficiency of the cathode.

3.1.2.5 Conduction

The conductivity reported for the molybdenum/rhenium alloy is $64\text{ W/m }^{\circ}\text{C}$ at $1000\text{ }^{\circ}\text{C}$ and $66\text{ W/m }^{\circ}\text{C}$ at $1200\text{ }^{\circ}\text{C}$ [63]. Figure 3.5 contains the temperature profiles of the cathode with conductivities from $32\text{-}128\text{ W/m }^{\circ}\text{C}$. The other parameters of the cathode can be found in Table 3-6. Other than conductivities, the other initial parameters were kept constant.

With lower conductivity, the insert temperatures increase along with the emission current. However, the amount of energy deposited into the insert decreases. The cooling from the thermionic electrons decreases with greater conductivity since more energy is lost through conduction and less is available to expel electrons. The peak temperature is also lower for this very reason. For the conductivity to decrease from 64 to $32\text{ W/m }^{\circ}\text{C}$ with the same plasma conditions, the emission current increases by over 2 A and the heat

flux decreases by 5 W. The most efficient cathode would minimize the amount of heat lost if constructed from a low thermal conductive material.

In Figure 3.5 the curve corresponding to the lowest conductivity of $32 \text{ W/m } ^\circ\text{C}$ has a profile different than the other curves. This is a result of radiation becoming a more dominant mechanism for heat transfer. As mentioned previously, the "kink" in the curves around the 2.6-cm location is a result of the change in cathode wall thickness.

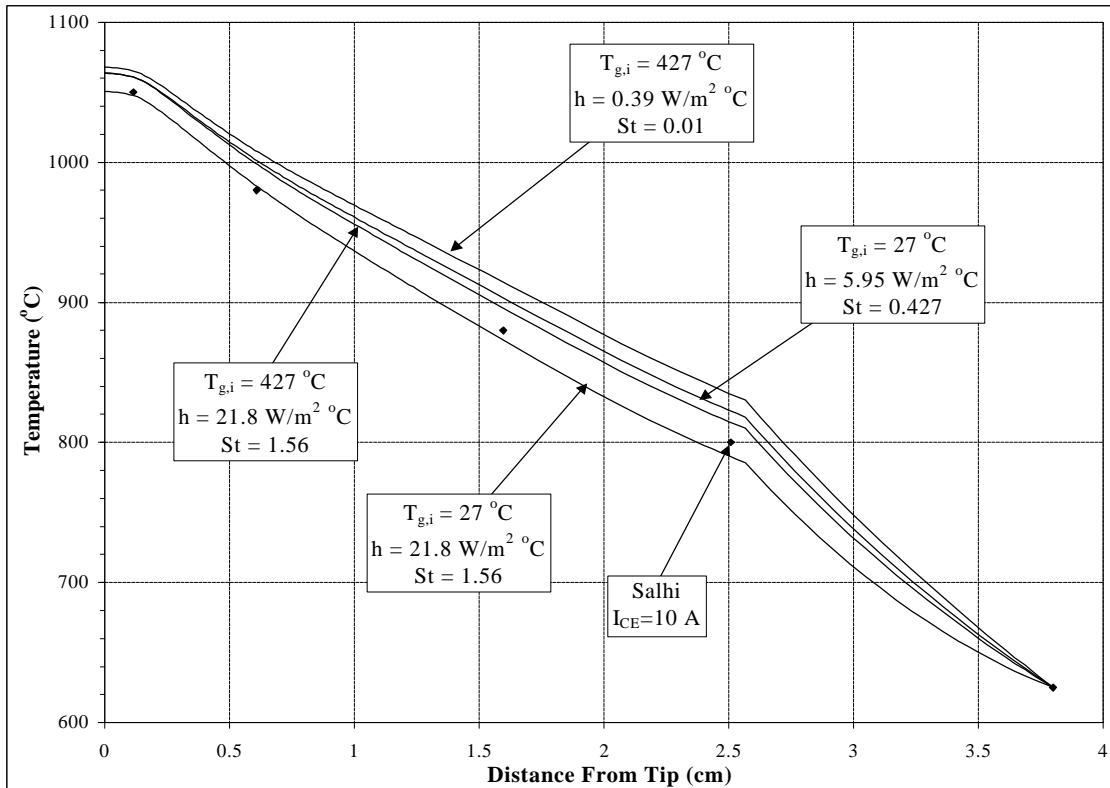


Figure 3.4. Cathode Temperature with Different Convection Terms
(Salhi's Error $\pm 50^\circ\text{C}$)

Table 3-5 Cathode Properties Corresponding to Figure 3.4

	Case 1	Case 2	Case 3	Case 4
Conductivity, K_w , ($\text{W/m } ^\circ\text{C}$)	64	64	64	64
Inlet Gas Temperature, $T_{g,i}$, ($^\circ\text{C}$)	427	27	427	27
Convection Coefficient, h, ($\text{W/m}^2 \text{ } ^\circ\text{C}$)	21.8	21.8	0.39	5.95
Stanton Number, St	1.56	1.56	0.01	0.427
Ohmic Heating, q , (W/ m^2)	100	100	100	100
Work Function, ϕ , (eV)	1.9	1.9	1.9	1.9
Outer Emissivity, ϵ_o	0.2	0.2	0.2	0.2
Inner Emissivity, ϵ_{in}	0.3	0.3	0.3	0.3

Percent of Ne for Id=12A	47	47	47	47
Ion Current, $\int J_i dA$, (A)	1.53	1.53	1.53	1.53
Energetic Electron Current, $\int J_e dA$, (A)	0.05	0.05	0.05	0.05
Thermionic Current, $\int J_{th} dA$, (A)	8.63	7.07	9.37	8.73
Total Current (Emission), I_{CE} , (A)	10.11	8.55	10.85	10.21
Energy from Ions and Electrons (W)	32.83	32.25	32.26	32.26
Thermionic Cooling (W)	18.22	14.91	19.81	18.43
Net Power Deposited (W)	14.61	17.34	12.45	13.83
Surrounding Temperature, T_∞ , ($^\circ\text{C}$)	27	27	27	27
Tip Boundary Condition	insulated	insulated	insulated	insulated
Base Boundary Condition ($^\circ\text{C}$)	625	625	625	625

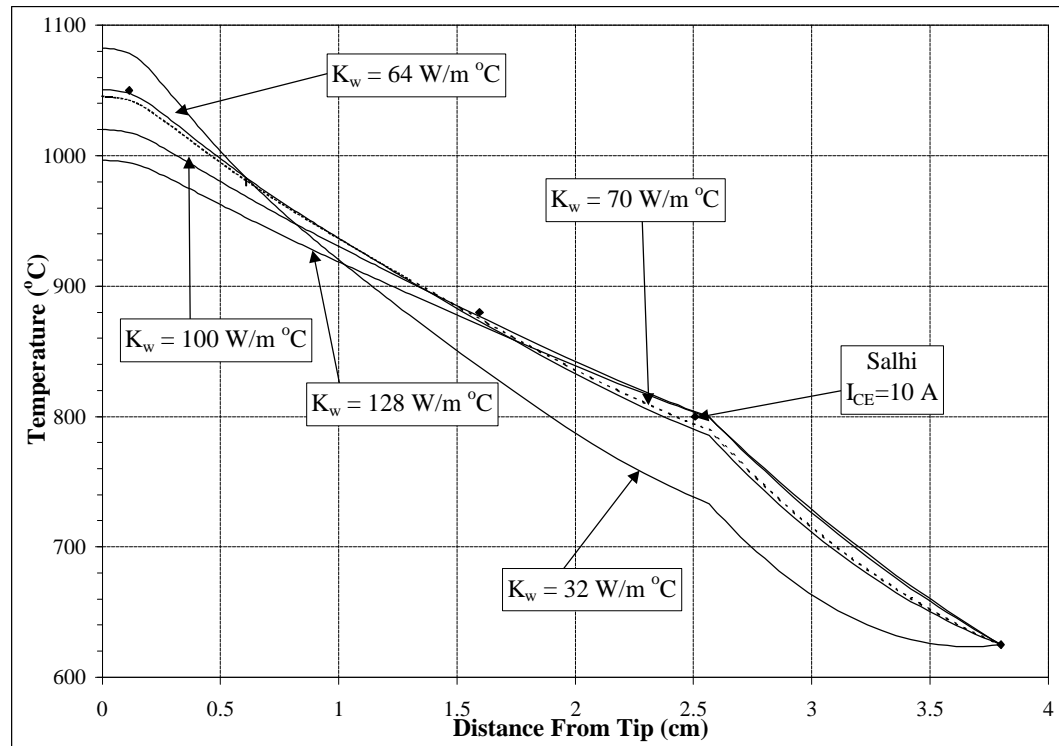


Figure 3.5. Cathode Temperature Profile for Different Conductivities
(Salhi's Error $\pm 50^\circ\text{C}$)

Table 3-6 Cathode Properties Corresponding to Figure 3.5

	Case 1	Case 2	Case 3	Case 4	Case 5
Conductivity, K_w, (W/m $^\circ\text{C}$)	32	64	70	100	128
Inlet Gas Temperature, $T_{g,i}$, ($^\circ\text{C}$)	27	27	27	27	27
Convection Coefficient, h , (W/m 2 $^\circ\text{C}$)	21.8	21.8	21.8	21.8	21.8
Stanton Number, St	1.56	1.56	1.56	1.56	1.56
Ohmic Heating, q , (W/ m 2)	100	100	100	100	100
Work Function, ϕ , (eV)	1.9	1.9	1.9	1.9	1.9
Outer Emissivity, ϵ_o	0.2	0.2	0.2	0.2	0.2
Inner Emissivity, ϵ_{in}	0.3	0.3	0.3	0.3	0.3
Percent of Ne for Id=12A	47	47	47	47	47

Ion Current, $\int J_i dA$, (A)	1.53	1.53	1.53	1.53	1.53
Energetic Electron Current, $\int J_e dA$, (A)	0.05	0.05	0.05	0.05	0.05
Thermionic Current, $\int J_{th} dA$, (A)	9.39	7.07	6.69	4.99	3.68
Total Current (Emission), I_{CE} , (A)	10.87	8.55	8.17	6.47	5.16
Energy from Ions and Electrons (W)	32.26	32.25	32.25	32.24	32.24
Thermionic Cooling (W)	19.83	14.91	14.11	10.51	7.74
Net Power Deposited (W)	12.43	17.34	18.14	21.73	24.50
Surrounding Temperature, T_∞ , ($^\circ\text{C}$)	27	27	27	27	27
Tip Boundary Condition	insulated	insulated	insulated	insulated	insulated
Base Boundary Condition ($^\circ\text{C}$)	625	625	625	625	625

3.1.2.6 Emissive Terms

The emissivity expected for molybdenum is between 0.1-0.3 [49]. It is difficult to know the emissivity of the insert region since the material composition can change through its lifetime, so for this analysis, it will just be assumed the same throughout the inner region.

Figure 3.6 depicts several cathode temperature profiles with varying emissivities on the inside and outside. Table 3-7 has the corresponding cathode properties. The cathode is much more sensitive to the emissivity values on the exterior of the cathode than it is on its interior. The internal emissivity has a minimal impact on cathode temperatures and can be considered black body for small diameter cathodes. Figure 3.6 shows an interior emissivity varying from 0.05 to 1.0 and an exterior emissivity of 0.2 with only a slightly noticeable difference on the temperature profile. It would be expected that with an increase in the internal diameter of the cathode the interior emissivity would become more of a factor.

By varying the exterior emissivity, a noticeable difference takes place as shown in Figure 3.6. A black body analysis on the exterior of the cathode would be wrong as demonstrated by the temperature profiles that vary considerably from experimental values. A more efficient cathode will have the exterior surface polished to minimize heat loss. For the same plasma conditions and in an environment of 27°C the heat flux decreases by close to 5 W and the emission current increases by approximately 2.5 A.

For the cathode Salhi was using, an exterior emissivity of 0.2 appears appropriate and the interior emissivity is insensitive to any value between 0.05 to 1.0.

3.1.2.7 Discharge Voltages

The analysis in previous sections used Salhi's data for an emission current of 10 A to evaluate the variation of possible parameters for the cathode he used. These values can now be used to predict temperature profiles and heat fluxes for different emission currents. It is difficult to know and measure the actual work function of the insert surface, so values of 1.9 eV and 2.0 eV will be presented here. It is also assumed, as mentioned before, that temperatures in the insert region are 100-130 °C higher than Salhi's thermocouple measurements for higher emission currents and up to 150°C higher for lower emission currents.

Figure 3.7 shows the temperature profiles for a work function of 1.9 eV for various emission currents. Table 3-8 contains the related information about the cathode for Figure 3.7. Figure 3.8 contains the temperature profiles for the same emission currents as in Figure 3.7 except for an insert work function of 2.0 eV. Table 3-9 contains the cathode property information for Figure 3.8.

The temperatures corresponding to the 1.9 eV work function fit the thermocouple data better, but the temperatures for the 2.0 eV work function better fit the temperature discrepancy that would be expected between the insert and the cathode wall.

Figure 3.9 shows the relationship between the thermionic current, ion current and the cathode emission current. For slight changes in ion current, there is a dramatic change in the current from thermionic emission. As the emission current increases, the amount of thermionic emission current increases. Goldstein estimates the ion current to be 20-30% of the emission current [50]. This is approximately the amount found here. However, for emission currents of 2 A and lower this percentage is higher and for emission currents larger than 8 A this percentage is smaller. It is important to note that Goldstein only

examined the emission currents in the range of 5-9 A. The thermionic current is insensitive to change in work function. For a particular cathode emission current, the work function has a dramatic effect on the temperature, but the thermionic and ionic current ratio remains about the same. Generally, for a higher work function, a larger amount of ion flux is needed to provide the necessary energy.

Figure 3.10 reflects the relationship between the heat fluxes present from the plasma and the emission current. Surprisingly, there is not much change predicted in the amount of net heat flux present for varying emission currents. For a mercury cathode, Goldstein predicts a greater change in the heat flux as the emission current varies. He predicts 15-41 W net power to the cathode with the emission currents varying from 5.4-9 A, respectively. However, the cathode he examined had significant differences, with the use of mercury being a predominant one (changing the amount of energy an ion deposits).

Other discrepancies which make Goldstein's model difficult to compare to are certain assumptions he made. One assumption he made was that the coolest part of the cathode tip would have the most thermionic emission since it was a cooling mechanism. However, this is contrary to the fact that thermionic emission is highly dependent on the temperature such that with higher temperatures there is greater emission. The temperature curve he uses for calibration has its peak temperature approximately 3 mm from the tip of the cathode. Then there is a 25-50°C drop in the first two millimeters. This phenomenon has not been found in other literature.

He also concludes that the electrons are coming from low work function material being deposited in the orifice region. This theory is not supported for the xenon cathodes [64].

Further investigation would need to be done in the material properties of the cathode, and more accurate testing of cathode temperatures would help resolve the uncertainty in the heat flux to the cathode. The initial base temperatures have a significant factor in determining the amount of heat flux that will be needed for a given emission

current. Since roughly the same temperature is needed in the insert for a particular emission current, the more the other heat losses can be minimized (*ie.* lower conductivity and emissivities in cathode) the less ion heat flux is needed to maintain a particular temperature and current. The heat flux necessary for a particular emission current is going to be highly dependent on all the energy loss mechanisms present.

3.1.2.8 Conclusion

A model has been developed which predicts the heat flux present for varying emission currents. This heat flux is highly dependent on the loss characteristics in a cathode. These include conductive, radiative, and some convective losses. The heat flux needed is also highly dependent on the work function of the insert material. For a certain work function, the temperature the insert needs to reach is constant with some small variations based on the electric field present. So minimizing the thermal losses should increase cathode efficiency.

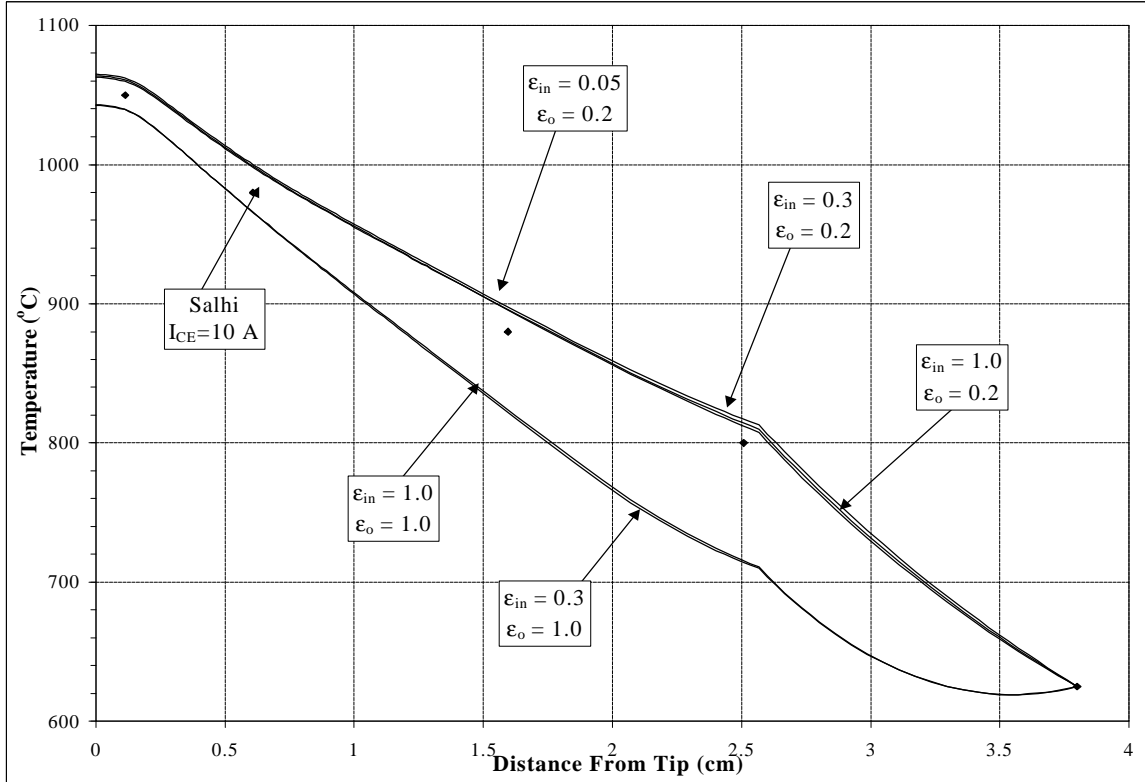


**Figure 3.6. Cathode Temperature Profiles for Different Emissive Terms
(Salhi's Error $\pm 50^{\circ}\text{C}$)**

Table 3-7 Cathode Properties Corresponding to Figure 3.6

	Case 1	Case 2	Case 3	Case 4	Case 5
Conductivity, K_w , (W/m $^{\circ}\text{C}$)	64	64	64	64	64
Inlet Gas Temperature, $T_{g,i}$, ($^{\circ}\text{C}$)	427	427	427	427	427
Convection Coefficient, h , (W/m 2 $^{\circ}\text{C}$)	21.8	21.8	21.8	21.8	21.8
Stanton Number, St	1.56	1.56	1.56	1.56	1.56
Ohmic Heating, q , (W/ m 2)	100	100	100	100	100
Work Function, ϕ , (eV)	1.9	1.9	1.9	1.9	1.9
Outer Emissivity, ϵ_o	1	1	0.2	0.2	0.2
Inner Emissivity, ϵ_{in}	1	0.3	1	0.3	0.05
Percent of Ne for $I_d=12\text{A}$	47	47	47	47	47
Ion Current, $\int J_i dA$, (A)	1.55	1.55	1.55	1.55	1.55
Energetic Electron Current, $\int J_e dA$, (A)	0.05	0.05	0.05	0.05	0.05
Thermionic Current, $\int J_{th} dA$, (A)	6.04	6.06	8.52	8.63	8.78
Total Current (Emission), I_{CE} , (A)	7.54	7.56	10.02	10.13	10.28
Energy from Ions and Electrons (W)	32.82	32.82	32.83	32.83	32.83
Thermionic Cooling (W)	12.72	12.76	17.98	18.22	18.54
Net Power Deposited (W)	20.10	20.06	14.85	14.61	14.29
Surrounding Temperature, T_{∞} , ($^{\circ}\text{C}$)	27	27	27	27	27
Tip Boundary Condition	insulated	insulated	insulated	insulated	insulated
Base Boundary Condition ($^{\circ}\text{C}$)	625	625	625	625	625

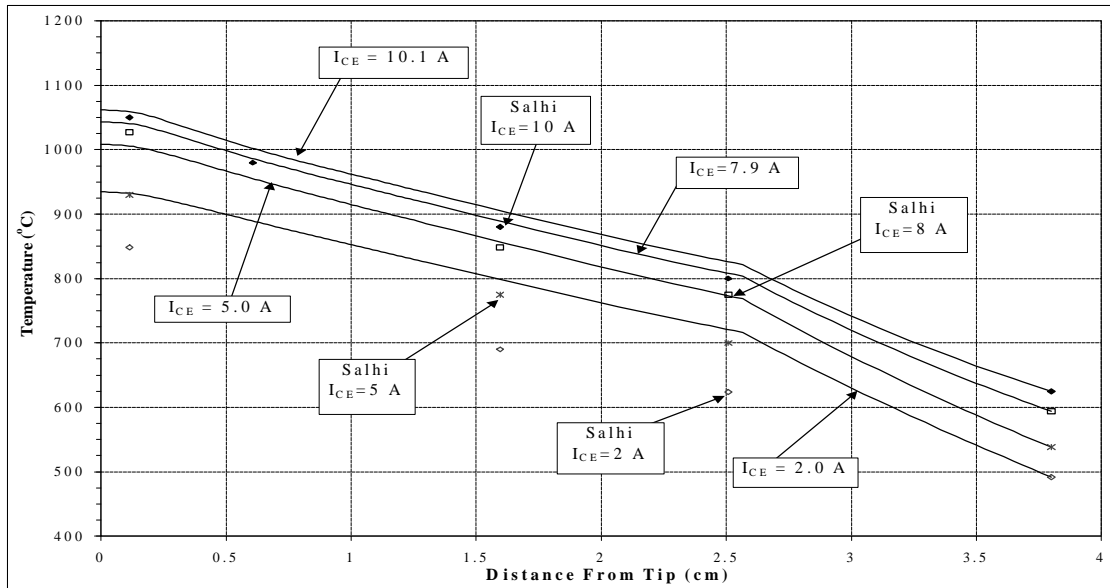


Figure 3.7. Temperature Profiles of a Cathode with a 1.9 eV Work Function Insert for Various Cathode Emission Currents (Salhi's Error $\pm 50^\circ\text{C}$)

Table 3-8 Cathode Properties Corresponding to Figure 3.7

	Case 1	Case 2	Case 3	Case 4
Conductivity, K_w , (W/m °C)	70	70	70	70
Inlet Gas Temperature, $T_{g,i}$, (°C)	27	27	27	27
Convection Coefficient, h , (W/m ² °C)	5.95	5.95	5.95	5.95
Stanton Number, St	0.427	0.427	0.427	0.427
Ohmic Heating, q , (W/ m ²)	100	100	100	100
Work Function, ϕ, (eV)	1.9	1.9	1.9	1.9
Outer Emissivity, ϵ_o	0.2	0.2	0.2	0.2
Inner Emissivity, ϵ_{in}	0.3	0.3	0.3	0.3
Percent of Ne for $I_d=12A$	48	42	34	24
Ion Current, $\int J_i dA$, (A)	1.56	1.37	1.11	0.78
Energetic Electron Current, $\int J_e dA$, (A)	0.05	0.04	0.03	0.02
Thermionic Current, $\int J_{th} dA$, (A)	8.62	6.62	3.94	1.22
Total Current (Emission), I_{CE}, (A)	10.13	7.95	5.02	1.98
Energy from Ions and Electrons (W)	32.94	28.82	23.32	16.45
Thermionic Cooling (W)	18.21	13.97	8.30	2.57
Net Power Deposited (W)	14.73	14.85	15.02	13.88
Surrounding Temperature, T_∞ , (°C)	27	27	27	27
Tip Boundary Condition	Insulated	insulated	insulated	insulated
Base Boundary Condition (°C)	625	595	538	492

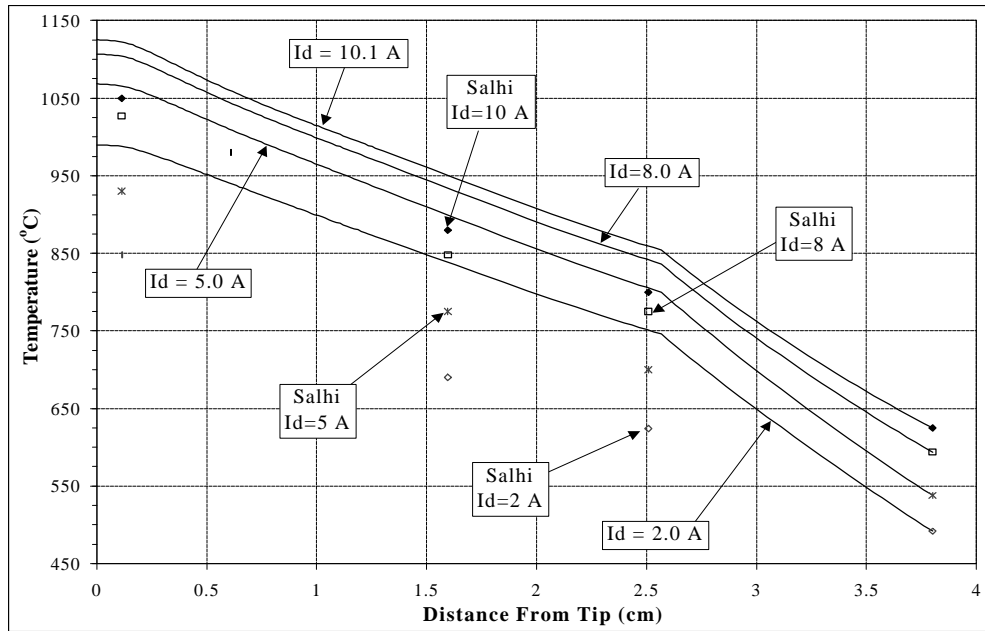


Figure 3.8. Temperature Profiles of a Cathode with a 2.0 eV Work Function Insert for Various Cathode Emission Currents (Salhi's Error $\pm 50^{\circ}\text{C}$)

Table 3-9 Cathode Properties Corresponding to Figure 3.8

	Case 1	Case 2	Case 3	Case 4
Conductivity, K_w , (W/m $^{\circ}\text{C}$)	70	70	70	70
Inlet Gas Temperature, $T_{g,i}$, ($^{\circ}\text{C}$)	27	27	27	27
Convection Coefficient, h , (W/m 2 $^{\circ}\text{C}$)	5.95	5.95	5.95	5.95
Stanton Number, St	0.427	0.427	0.427	0.427
Ohmic Heating, q , (W/ m 2)	100	100	100	100
Work Function, ϕ, (eV)	2.0	2.0	2.0	2.0
Outer Emissivity, ϵ_o	0.2	0.2	0.2	0.2
Inner Emissivity, ϵ_{in}	0.3	0.3	0.3	0.3
Percent of Ne for $I_d=12A$	52	46	37	26.5
Ion Current, $\int J_i dA$, (A)	1.69	1.50	1.20	0.86
Energetic Electron Current, $\int J_e dA$, (A)	0.05	0.05	0.04	0.03
Thermionic Current, $\int J_{th} dA$, (A)	8.48	6.59	3.81	1.16
Total Current (Emission), I_{CE}, (A)	10.12	8.04	4.97	1.99
Energy from Ions and Electrons (W)	35.55	31.44	25.28	18.09
Thermionic Cooling (W)	18.85	14.64	8.44	2.56
Net Power Deposited (W)	16.70	16.80	16.84	15.53
Surrounding Temperature, T_{∞} , ($^{\circ}\text{C}$)	27	27	27	27
Tip Boundary Condition	insulated	insulated	insulated	insulated
Base Boundary Condition ($^{\circ}\text{C}$)	625	595	538	492

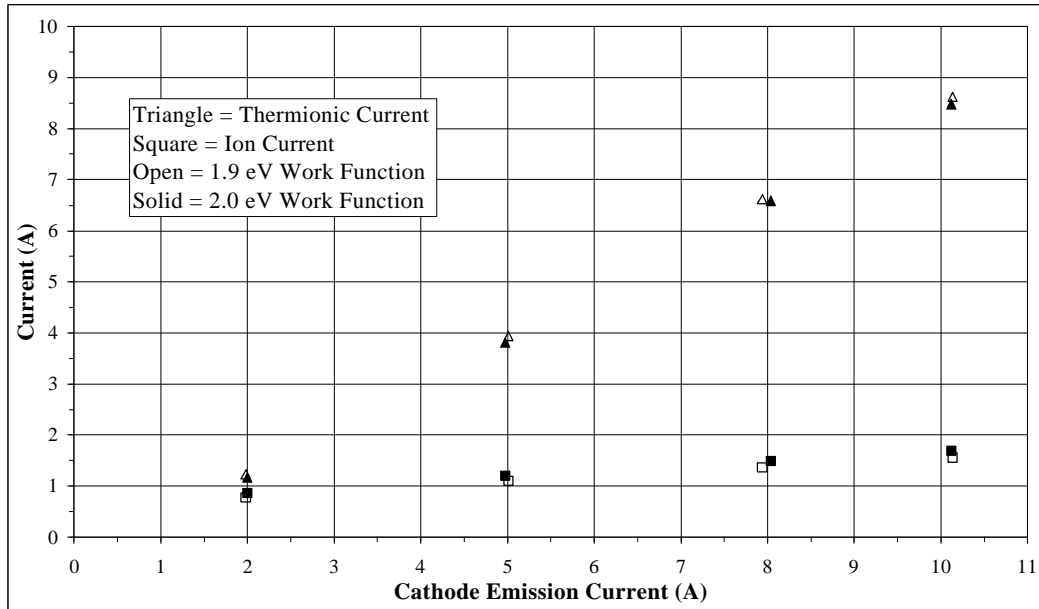


Figure 3.9. Thermionic and Ion Current as a Function of Cathode Emission Current

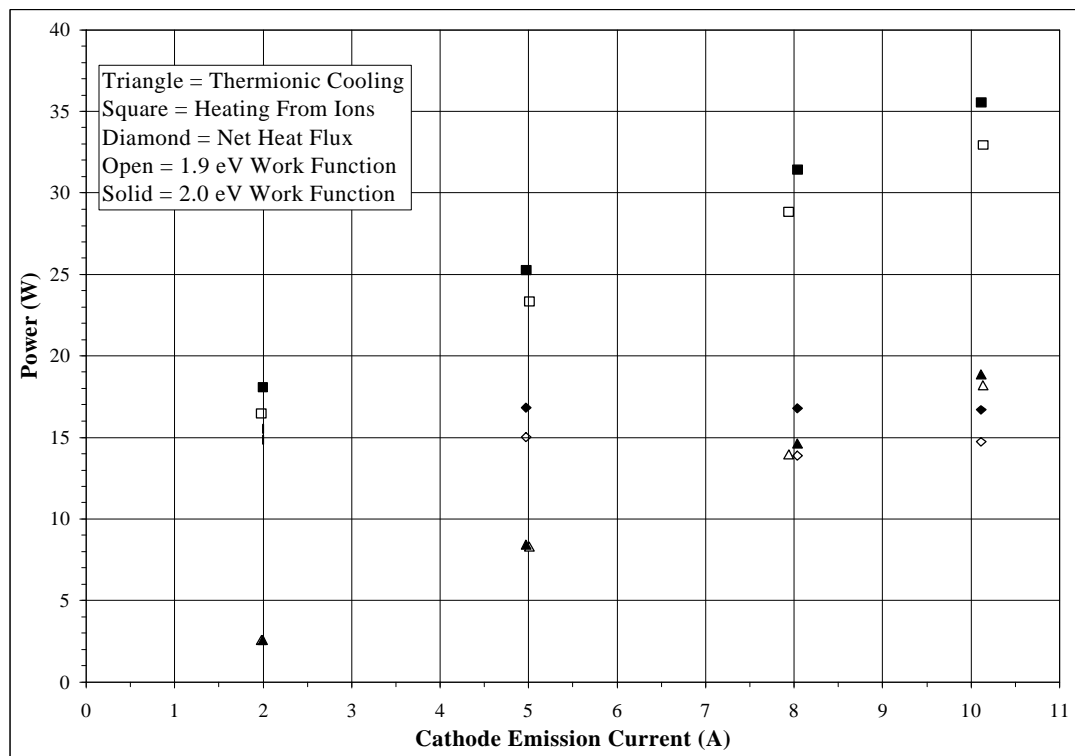


Figure 3.10. Plasma Heating and Cooling Mechanism as Function of Cathode Emission Current

3.2 Discharge Chamber

Much of the model for determining the plasma characteristics in the ion thruster is based on the ion thruster performance model presented by Brophy, which is the prominent model for high flux density, cusped magnetic field thrusters [41]. In order for a comparison to his model and the model presented here to be accomplished, the values of the baseline plasma ion energy costs, ϵ_p^* , will have to be evaluated. This will demonstrate the compatibility between the models.

To compare the model to previous estimations of heat flux to surfaces, comparison will be done to a SERT II-type thruster presented by Wells, *et al.* [38]. Most studies previously reported have focused on temperatures of thrusters and very few on the heat flux present.

3.2.1 Baseline Plasma Ion Energy Cost, ϵ_p^*

The comparison between Brophy's work and this model is based on Equation 2.71 (Equations 2.68 and 2.70 are the equations Brophy plotted). The thruster examined used xenon propellant and did not have a keeper on the cathode. It was operated at a discharge voltage, V_D , of 40 V and the keeper voltages would be zero since no keeper was present. Brophy reports the anode sheath, V_A , to be 2 V. The ionization potential from published data is taken to be 12.13 eV for xenon [19]. The lowest excitation energy is calculated to be 9.230 eV, but observed as 8.315 eV [65]. The collision cross section data for the ionization [66] and total excitation [67] for xenon are taken from the same sources as reported by Brophy. The enclosed product averaged over the Maxwellian energy distribution function shown in Equation 2.63 was determined numerically using a 20-term Gaussian integration scheme. Figure 3.11 shows this comparison between Brophy's model and the one presented here.

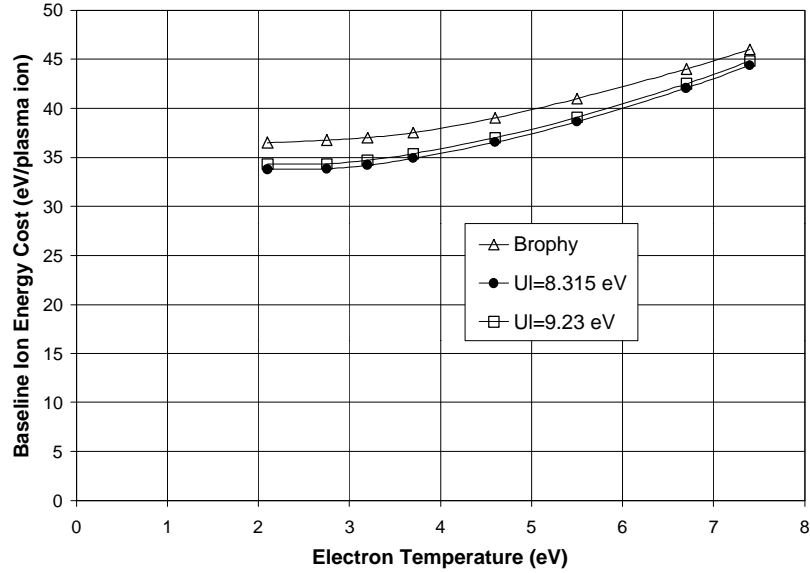


Figure 3.11. Baseline Plasma Ion Energy Costs for Xenon

The two models show a good correlation. However, the reason for the discrepancy between the two models is uncertain. The values of Brophy were determined graphically to within 1 eV. The discrepancy could be a result of using differing data or differing solution methods for the integration. Using a 40-term Gaussian integration instead of a 20-term Gaussian integration for the $\langle \epsilon \rangle_M$ term changes the value by less than 1%. The value predicted by the model here is consistent with Brophy's model.

3.2.2 Variation of Uncertain Parameters

In order to determine the various currents present in the discharge chamber and the associated heat fluxes, several terms are used which have a significant amount of uncertainty associated with them. These terms are found in Equations 2.62-2.71. A comparison will be done between the results of this model and what Wells *et al.* predicted for their SERT II-type thruster [38]. In order to accomplish this several of the more uncertain terms will be varied to determine their effect on the results. These parameters are the volume of the ion production region, the anode fall, the extracted ion fraction, the

primary electron length, the transparency of the screen grids to ions, and the effective transparency of the grids to neutral atoms.

The values used for the total ionization cross section of atomic mercury are given in a paper by Kieffer and Dunn [68]. These values vary up to 35% between different experiments. The total inelastic cross section for mercury is given by Walker [69]. The total excitation cross section was then determined by subtracting the ionization cross section from the total inelastic cross section.

3.2.2.1 Volume of the Ion Production Region

The volume of the ion production region, V_{ipr} , is the volume in the thruster where the ions are produced. It is defined by the magnetic field. Energetic electrons that cross the critical field line are collected by the anode. The critical field line is defined to be the innermost magnetic field line to intercept the anode [70]. Another form of the definition of the V_{ipr} is that it is defined by the outermost contour that contains 95% of the total ionization occurring inside the discharge chamber [71].

There are no magnetic field maps to determine this parameter for the mercury thruster examined. An estimate of the volume in the discharge chamber of this 15-cm diameter thruster would be $2.6 \times 10^{-3} \text{ m}^3$. This gives an upper bound on V_{ipr} , which will likely be considerably smaller.

Figure 3.12 and Figure 3.13 show the plasma surface currents and power deposition respectively for V_{ipr} 's that vary from 9×10^{-6} to $7 \times 10^{-5} \text{ m}^3$. Table 3-10 contains the other parameters held constant while V_{ipr} was varied. It can be seen from the figures that the current and power change drastically below the volume of $1 \times 10^{-5} \text{ m}^3$. The ion current to the keeper cannot be negative so the expected current is going to lie between the volumes of 1.5×10^{-5} and $2.1 \times 10^{-5} \text{ m}^3$. These values are a couple of order of magnitudes smaller than the volume of the discharge chamber, but are in a reasonable range.

It is important to note that negative ion current and correspondingly negative power to the keeper or anode are a result of mathematical solutions that are not physically obtainable conditions for a thruster. The condition that gives these results specifies that for every ion produced, each is accounted for by leaving the plasma via the beam, anode potential surfaces or cathode potential surfaces. This relation is shown in Equation 2.45. In order for that relation to be valid, there cannot be any negative ion flow from a surface. A negative ion flow would mean the surface contributed an ion to the plasma in order to maintain ion continuity by balancing those ions that are produced with those that leave the discharge plasma. This is not a mechanism present in impact ionization thrusters. Further, in this situation, a negative ion flow is not the same thing as an electron being deposited into a surface. If that were the case, there would be fewer ions produced than those that left the plasma and continuity would not be maintained. The results that dictate a negative ion flow from the keeper or anode then are not realistic conditions and can be neglected. As such, the valid results lie in the region where ion current to the keeper and anode are both positive.

Table 3-10 Parameters Held Constant while the Volume of the Ion Production Region was Varied

Parameters Held Constant	Respective Values
Discharge Voltage	44 V
Keeper Voltage	15 V
Discharge Current	2.02 A
Beam Current	0.256 A
Ion Current to Accelerator Grid	0.001 A
Flow Rate	4.241 sccm
Effective Neutral Transparency to Grids	0.12
Screen Grid Ion Transparency	0.6
Area of Grid Beam is Extracted through	0.006642 m ²
Anode Fall	2 V
Accelerator Fall	150 V
Extracted Ion Fraction	0.45
Primary Electron Length	0.5 m
Screen Grid Ion Current	0.17 A
Accelerator Grid Ion Current	0.001 A
Power from Ions to Accelerator Grid	0.16 W

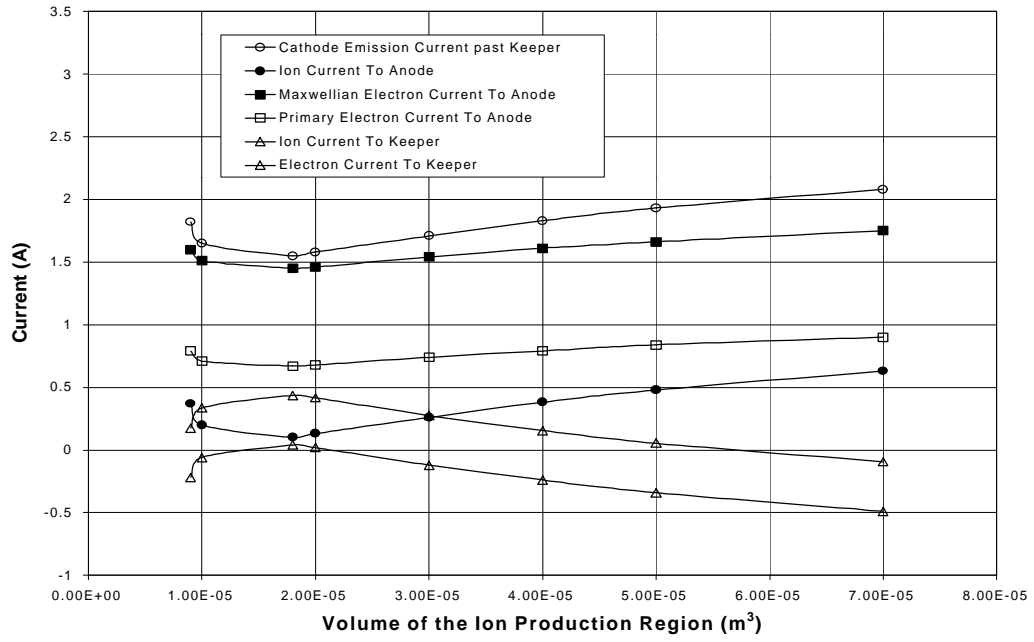


Figure 3.12. Change in Plasma Interaction Current with a Change in the Volume of the Ion Production Region

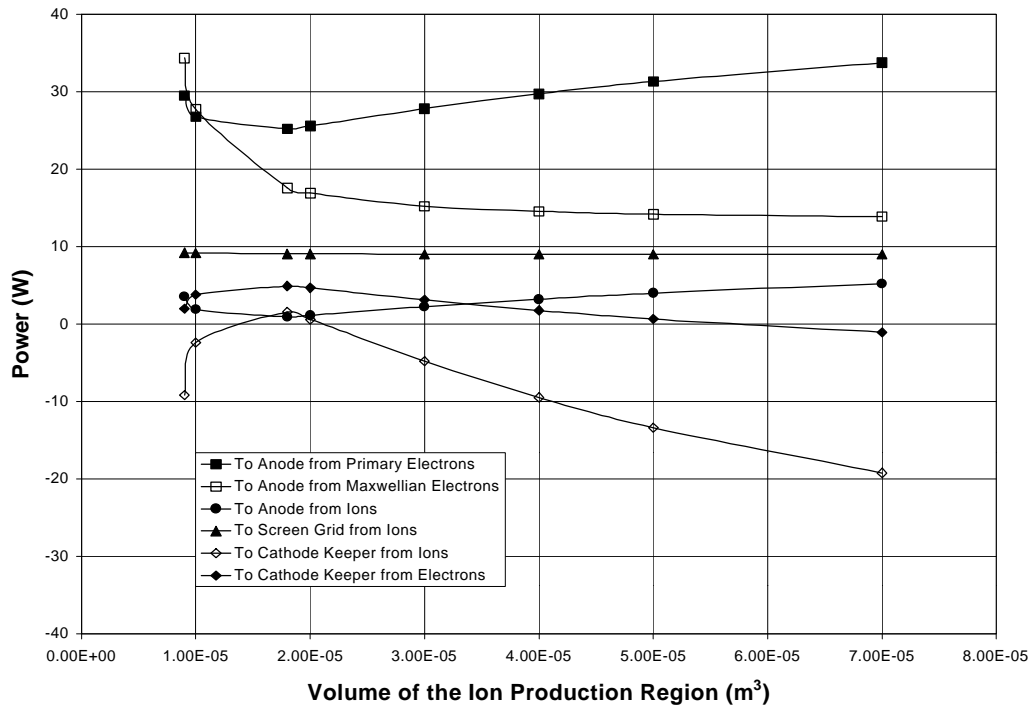


Figure 3.13. Change in the Power from Plasma Deposition with a Change in the Volume of the Ion Production Region

3.2.2.2 Extracted Ion Fraction

The extracted ion fraction, f_B , is the fraction of the total beam ions to the total ions produced in the discharge chamber. Vaughn reports values of 0.15 to 0.35 for the thruster he examined [61]. However, engines that are more efficient could have up to twice those values. Beam currents are readily available for a thruster so the amount of ions lost to surfaces in the thruster can be easily determined from f_B .

Figure 3.14 and Figure 3.15 show the plasma surface currents and power deposition respectively for extracted ion fractions from 0.35 to 0.6. Table 3-11 contains the related parameters used to produce these figures.

The ion current to the keeper and anode are simultaneously positive in only a small region of f_B . For the parameters used, f_B falls in the range of 0.44-0.47.

Table 3-11 Parameters Held Constant While the Extracted Ion Fraction was Varied

Parameters Held Constant	Respective Values
Discharge Voltage	44 V
Keeper Voltage	15 V
Discharge Current	2.02 A
Beam Current	0.256 A
Ion Current to Accelerator Grid	0.001 A
Flow Rate	4.241 sccm
Effective Neutral Transparency to Grids	0.12
Screen Grid Ion Transparency	0.6
Area of Grid Beam is Extracted through	0.006642 m ²
Anode Fall	2 V
Accelerator Fall	150 V
Volume of the Ion Production Region	1.8x10 ⁻⁵ m ²
Primary Electron Length	0.5 m
Screen Grid Ion Current	0.17 A
Power from Ions to Accelerator Grid	0.16 W

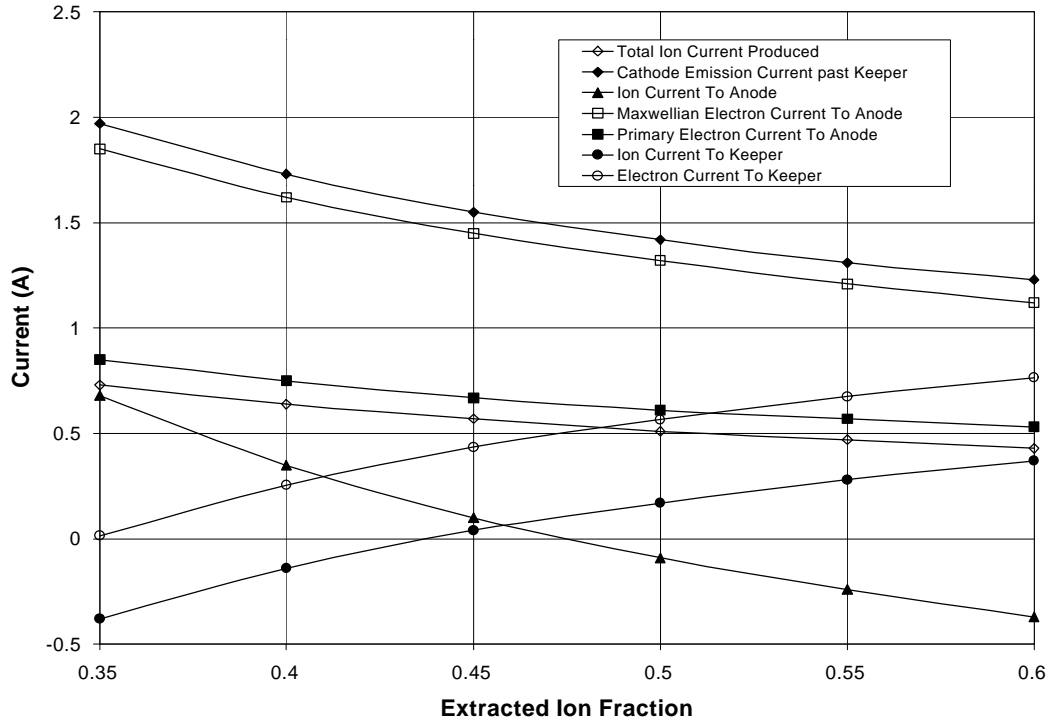


Figure 3.14. Change in Plasma Interaction Current with a Change in the Extracted Ion Fraction

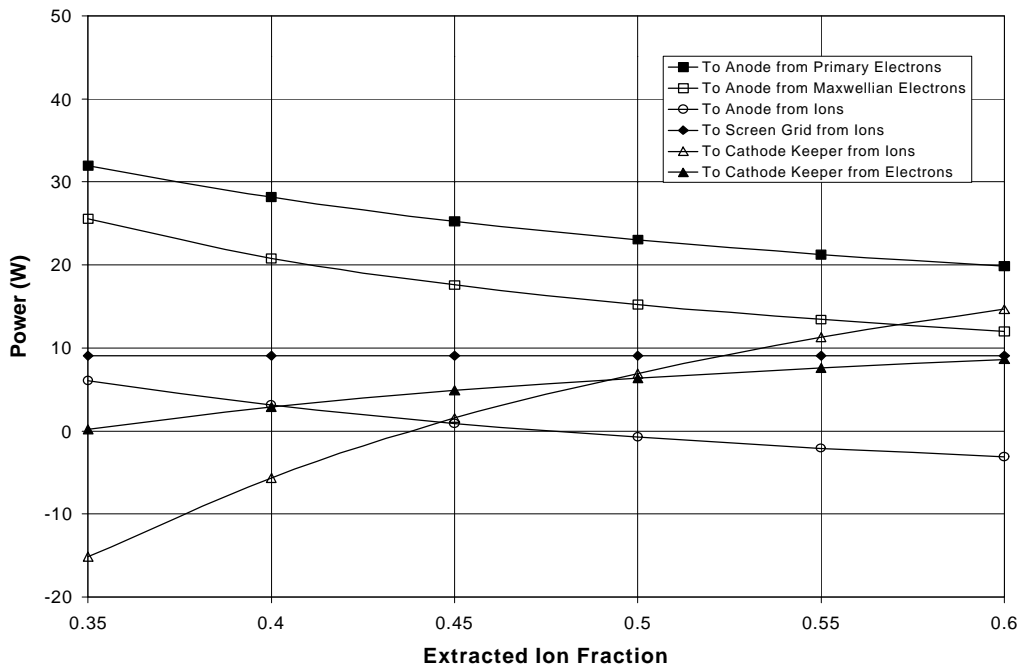


Figure 3.15. Change in the Power from Plasma Deposition with a Change in the Extracted Ion Fraction

3.2.2.3 Primary Electron Length

The primary electron length, l_e , is the average length a primary electron without an inelastic collision would travel to the anode. This is determined for an electron by its interaction with the magnetic and electric field, its velocity, and the thruster geometry. This length can be used to determine the probability of primary electron loss to the anode (this is a loss of energy). A rule of thumb for a thruster is that l_e is about 4 times the diameter of the thruster [72]. A 15-cm diameter thruster would then be about 60 cm.

Figure 3.16 and Figure 3.17 show the plasma surface currents and power deposition respectively for l_e from 0.3-1.0 m. Table 3-12 contains the values used to determine the figures for the primary electron length. The ion current to the keeper and the anode again determine that the reasonable range for l_e is from 0.48-0.56 m.

Table 3-12 Parameters Held Constant While the Primary Electron Length was Varied

Parameters Held Constant	Respective Values
Discharge Voltage	44 V
Keeper Voltage	15 V
Discharge Current	2.02 A
Beam Current	0.256 A
Ion Current to Accelerator Grid	0.001 A
Flow Rate	4.241 sccm
Effective Neutral Transparency to Grids	0.12
Screen Grid Ion Transparency	0.6
Area of Grid Beam is Extracted through	0.006642 m ²
Anode Fall	2 V
Accelerator Fall	150 V
Volume of the Ion Production Region	1.8x10 ⁻⁵ m ²
Extracted Ion Fraction	0.45
Screen Grid Ion Current	0.17 A
Power from Ions to Accelerator Grid	0.16 W

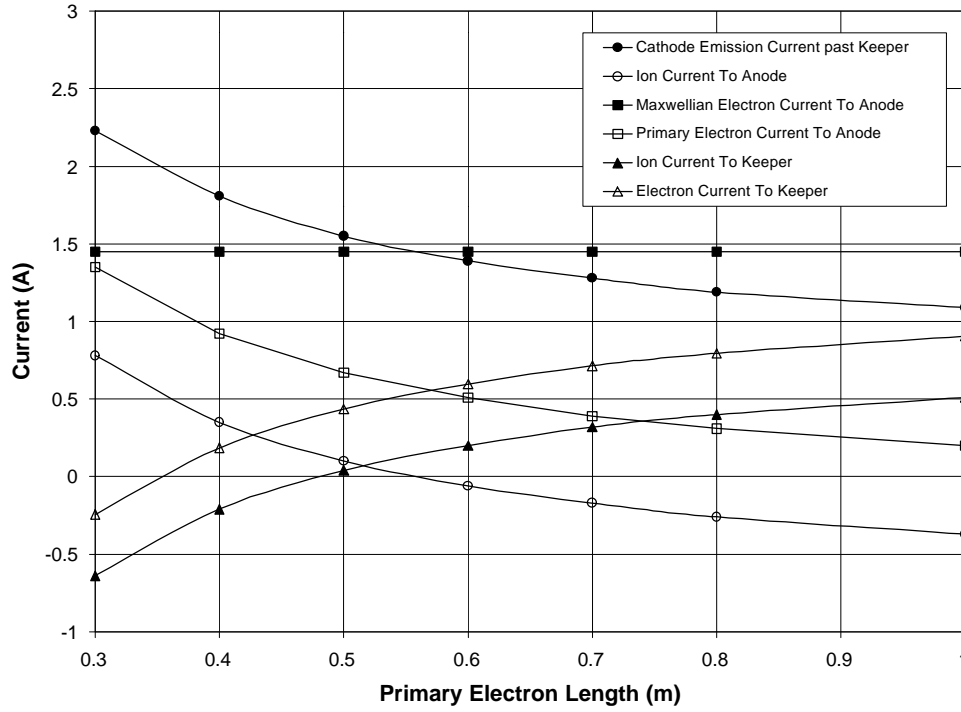


Figure 3.16. Change in Plasma Interaction Current with a Change in the Primary Electron Length

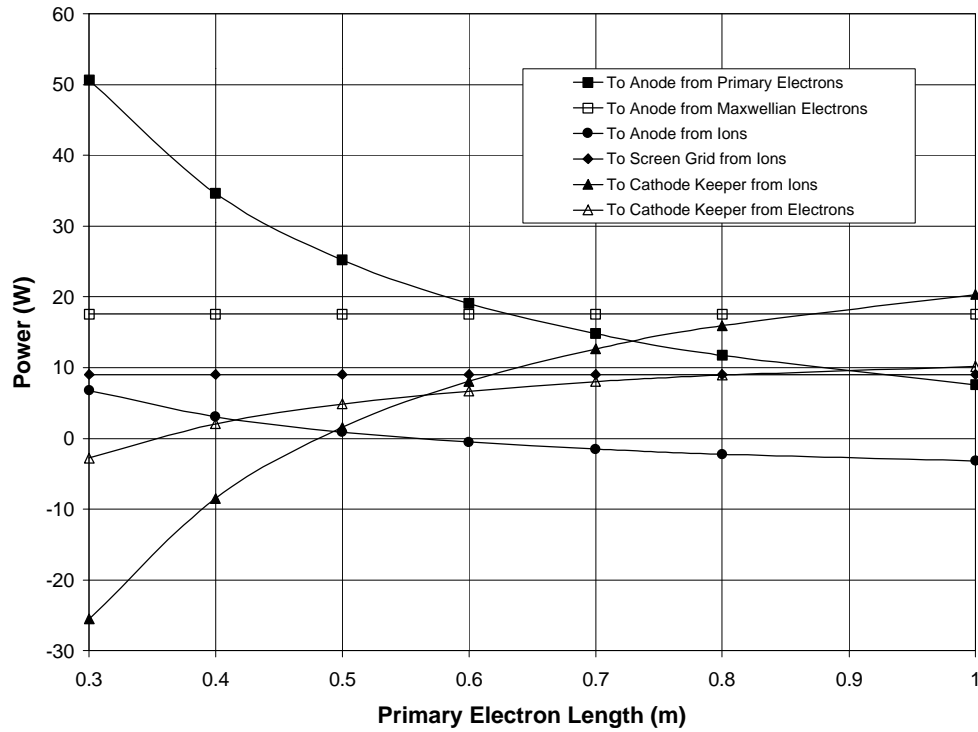


Figure 3.17. Change in Power from Plasma Deposition with a Change in the Primary Electron Length

3.2.2.4 Anode Fall

The anode fall on a thruster is determined by the potential present across the sheath at the anode. This sheath usually is a few volts positive of the anode. Brophy measured the sheath in his thruster to be 2 V [41].

Figure 3.18 and Figure 3.19 show the plasma surface currents and power deposition respectively for anode falls from 1 to 3 V. Table 3-13 contains the other values used to create these figures.

The positive value of the ion current to the keeper determines the maximum reasonable anode fall to be around 2.5 V. The ion current to the anode is still positive below an anode fall of 1 V, but the sheath is not expected to be lower than that value. So the anode fall lies between 1-2.5V.

Table 3-13 Parameters Held Constant while the Anode Fall was varied

Parameters Held Constant	Respective Values
Discharge Voltage	44 V
Keeper Voltage	15 V
Discharge Current	2.02 A
Beam Current	0.256 A
Ion Current to Accelerator Grid	0.001 A
Flow Rate	4.241 sccm
Effective Neutral Transparency to Grids	0.12
Screen Grid Ion Transparency	0.6
Area of Grid Beam is Extracted through	0.006642 m ²
Extracted Ion Fraction	0.45
Accelerator Fall	150 V
Volume of the Ion Production Region	1.8x10 ⁻⁵ m ²
Primary Electron Length	0.5 m
Screen Grid Ion Current	0.17 A
Power from Ions to Accelerator Grid	0.16 W

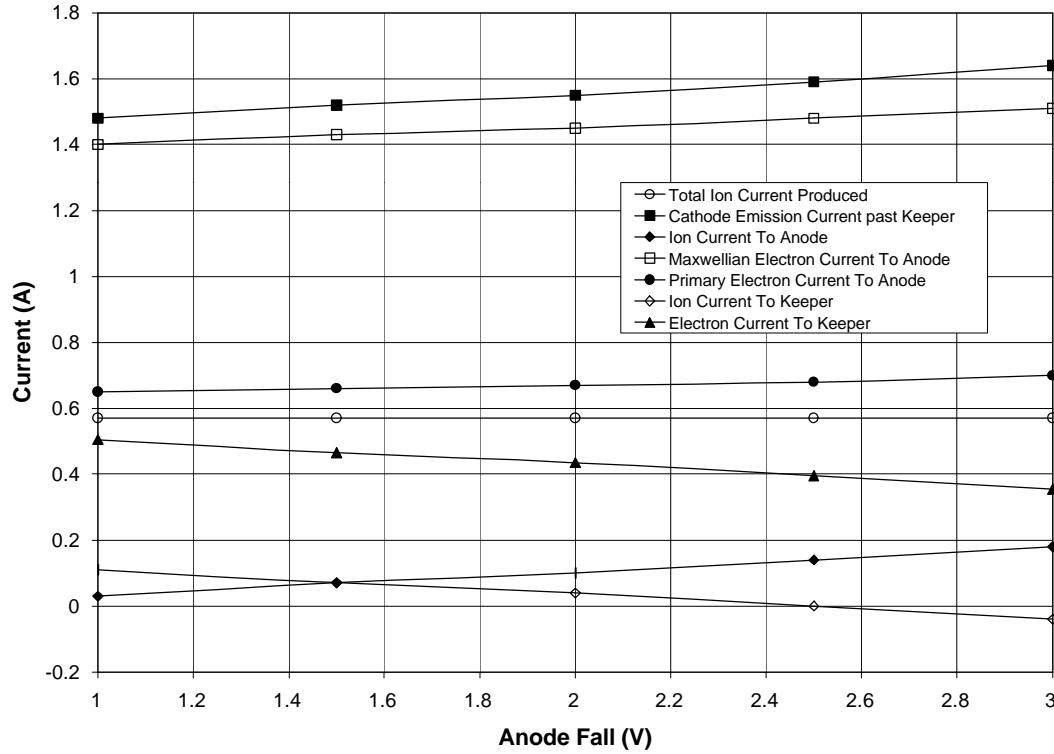


Figure 3.18. Change in Plasma Interaction Current with a Change in the Anode Fall

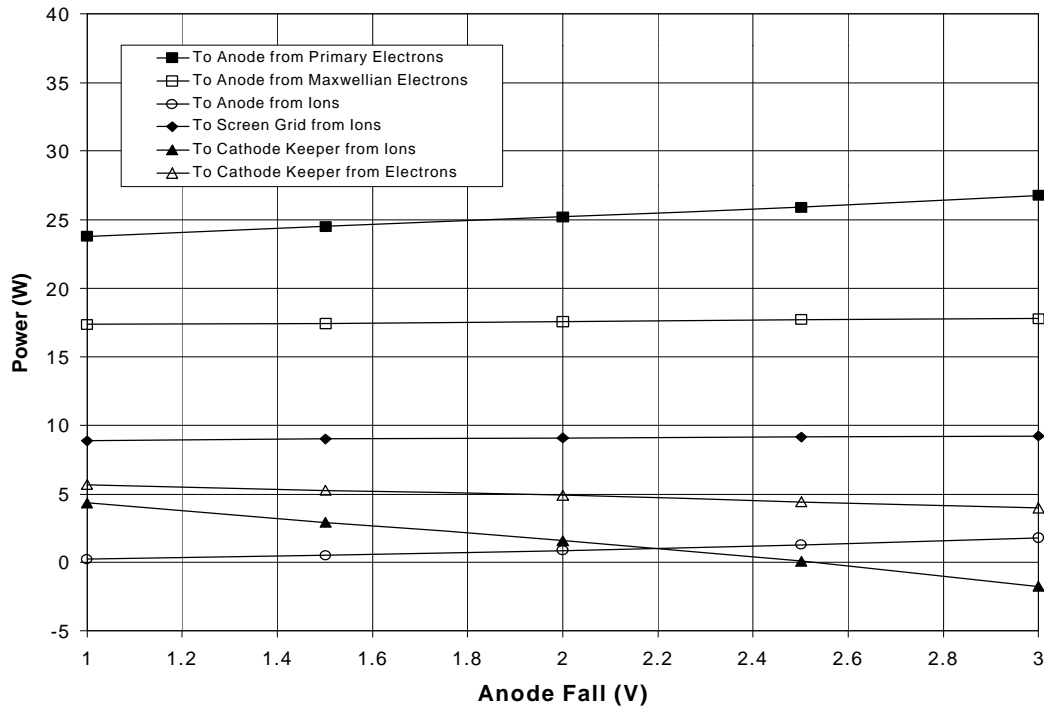


Figure 3.19. Change in Power from Plasma Deposition with a Change in the Anode Fall

3.2.2.5 Transparency of Screen Grid to Ions

The transparency of the screen grid to the ions, Φ_I , is an indicator of how well the ions accelerated in the beam direction are extracted. The ratio is the beam current over the beam current plus the ion current to the screen grid. The ratio of the open area of the screen grid to the total area is 0.59.

Figure 3.20 and Figure 3.21 show the plasma surface currents and power deposition respectively for Φ_I from 0.4-0.8. Table 3-14 contains the various parameters used for these figures.

The ion current to the keeper is negative for Φ_I 's lower than 0.57, so Φ_I 's below this value are not valid since they are not physically attainable for the thruster under these conditions. The change in transparency has the most noticeable effect on the power deposited on the screen grid. This is a result of more ions impacting the screen grid as Φ_I decreases (the screen grid becomes less transparent to ions passing through).

Table 3-14 Parameters Held Constant While the Transparency of the Screen Grid to Ions was Varied

Parameters Held Constant	Respective Values
Discharge Voltage	44 V
Keeper Voltage	15 V
Discharge Current	2.02 A
Beam Current	0.256 A
Ion Current to Accelerator Grid	0.001 A
Flow Rate	4.241 sccm
Effective Neutral Transparency to Grids	0.12
Extracted Ion Fraction	0.45
Area of Grid Beam is Extracted through	0.006642 m ²
Anode Fall	2 V
Accelerator Fall	150 V
Volume of the Ion Production Region	1.8x10 ⁻⁵ m ³
Primary Electron Length	0.5 m
Screen Grid Ion Current	0.17 A
Power from Ions to Accelerator Grid	0.16 W

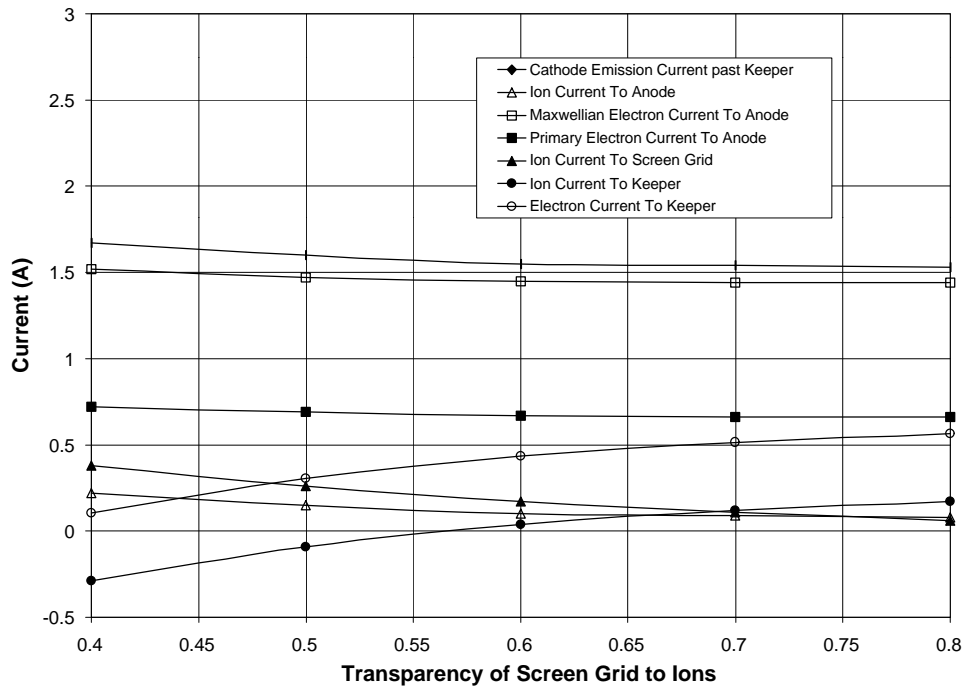


Figure 3.20. Change in Plasma Interaction Current with a Change in the Transparency of the Screen Grid to Ions

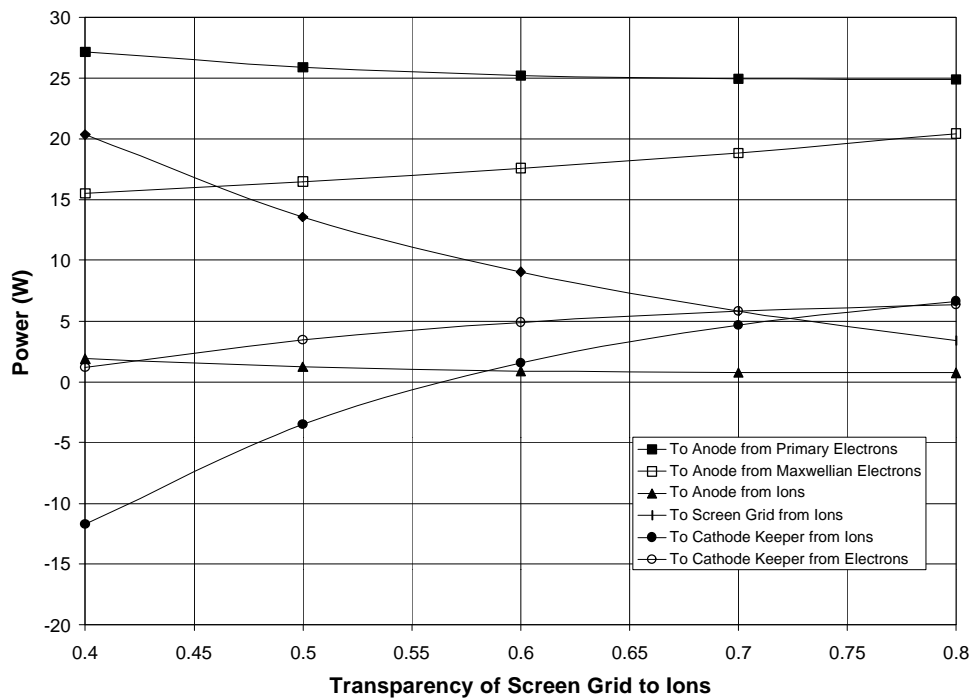


Figure 3.21. Change in Power Deposition from Plasma with a Change in the Transparency of Screen Grid to Ions

3.2.2.6 Effective Transparency of the Grids to Neutrals

The effective transparency of the grids to neutrals, Φ_o , is determined by the equation:

$$\Phi_o = \frac{\Phi_s \Phi_a}{\Phi_s + \Phi_a} \quad (3.3)$$

where Φ_a is the modified transparency of the accelerator grid to neutrals and Φ_s is the modified transparency of the screen grid to neutrals. These transparencies are based on the open area fraction.

With the open area fraction of the screen grid 0.59 and the open area fraction of the accelerator grid of 0.376, an estimate of Φ_o is 0.23. Brophy used values of 0.16 and 0.27 for the two different optics he had. Figure 3.22 and Figure 3.23 depict the plasma surface currents and power deposition respectively for Φ_o from 0.05 to 0.25. The ion current to the anode and to the keeper is concurrently positive for Φ_o between 0.11-0.125, so this is the region of physically attainable solutions for the thruster.

Table 3-15 Parameters Held Constant while the Transparency of the Screen Grid to Neutrals was Varied

Parameters Held Constant	Respective Values
Discharge Voltage	44 V
Keeper Voltage	15 V
Discharge Current	2.02 A
Beam Current	0.256 A
Ion Current to Accelerator Grid	0.001 A
Flow Rate	4.241 sccm
Extracted Ion Fraction	0.45
Screen Grid Ion Transparency	0.6
Area of Grid Beam is Extracted through	0.006642 m ²
Anode Fall	2 V
Accelerator Fall	150 V
Volume of the Ion Production Region	1.8x10 ⁻⁵ m ²
Primary Electron Length	0.5 m
Screen Grid Ion Current	0.17 A
Power from Ions to Accelerator Grid	0.16 W

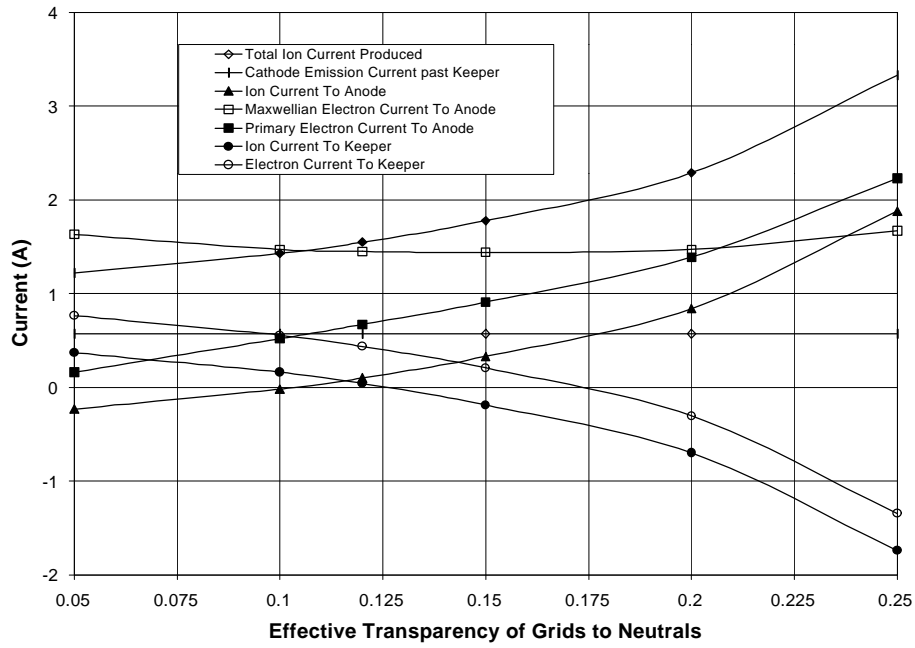


Figure 3.22. Change in Plasma Interaction Current with a Change in the Effective Transparency of the Grids to Neutrals

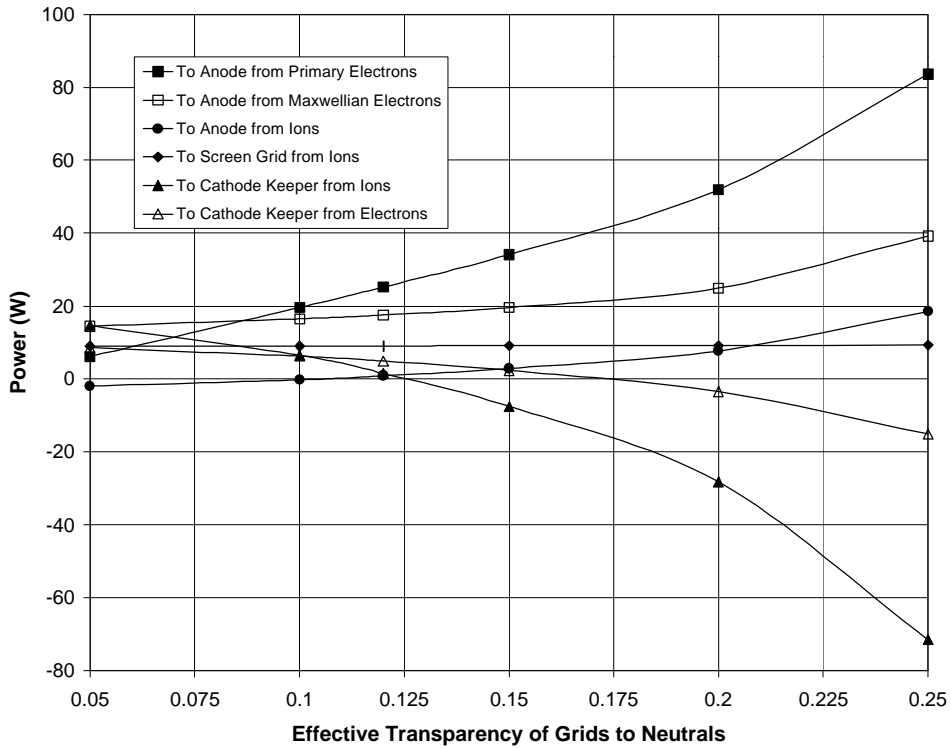


Figure 3.23. Change in the Power from Plasma with a Change in the Effective Transparency of the Grids to Neutrals

3.2.2.7 Maxwellian Electron Temperature

Figure 3.24 depicts how the Maxwellian electron temperature changes from a variation in several parameters. The change in anode fall and primary electron length has minimal effect on the Maxwellian temperature. The change in volume of the ion production region and the effective transparency of the grids to neutrals has the most significant effect on the Maxwellian temperature. However, it should be noted that a change in a thruster would not effect one parameter, but several simultaneously. Wells *et al.* determined that the Maxwellian electron temperature near the anode was around 3 eV [38].

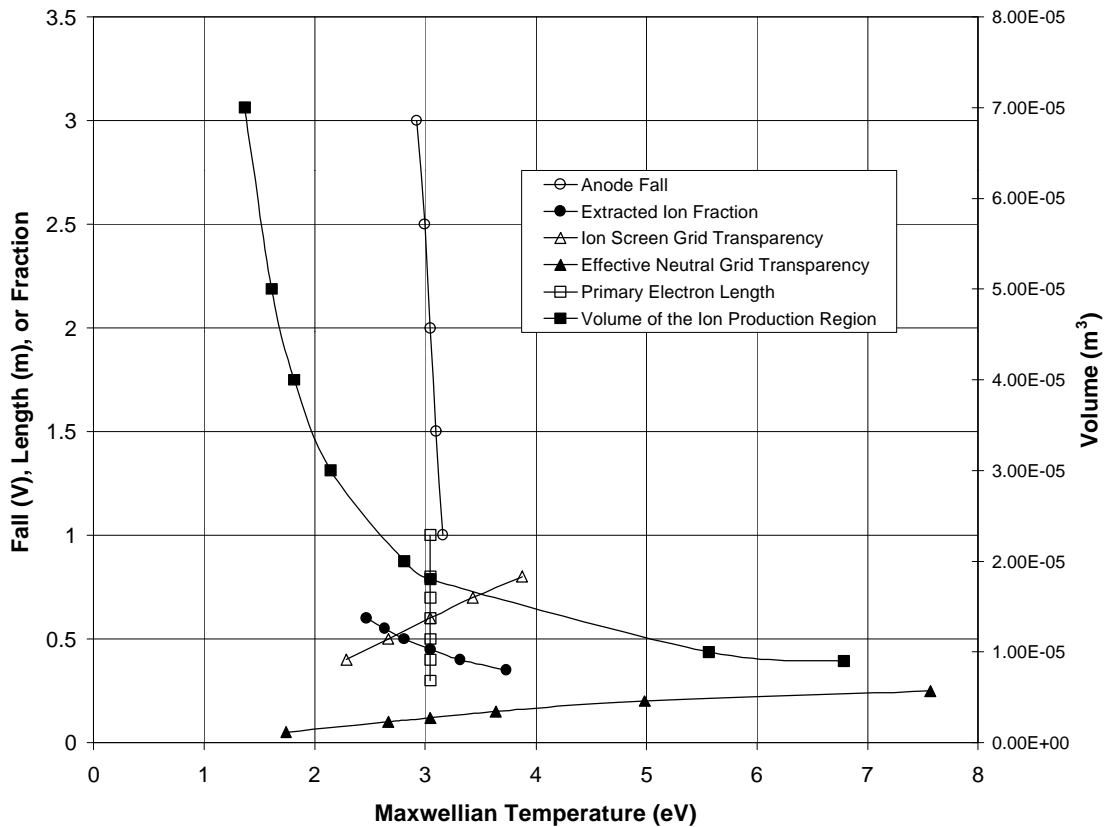


Figure 3.24. Variation of the Maxwellian Electron Temperature with the Changes in Various Parameters

3.2.2.8 Neutral, Ion and Electron Densities

The neutral density is fairly remains constant at $4.44 \times 10^{18} \text{ m}^{-3}$ for all the parameters except one. The change in the effective transparency of grids to neutrals (Φ_0), from 0.05 to 0.2, was the only parameter to vary the density from 1.06×10^{19} to $2.66 \times 10^{18} \text{ m}^{-3}$.

The Maxwellian electron density and the primary electron density determined for various parameters are shown in Figure 3.25 and Figure 3.26. Figure 3.27 then shows the average ion or total electron density. For the change in anode fall and primary electron length, the densities change very little. Changing these variables affects the amount of electrons that are necessary from the cathode. Fewer electrons are needed from the cathode to provide the same Maxwellian electron density.

It should be noted again that the parameters are not going to vary independently as shown here, but a change in one parameter will affect another. For example, changing the volume of the ion production region will also change the primary electron length and vice versa since both are a factor of the magnetic field present and physical dimensions of the discharge chamber.

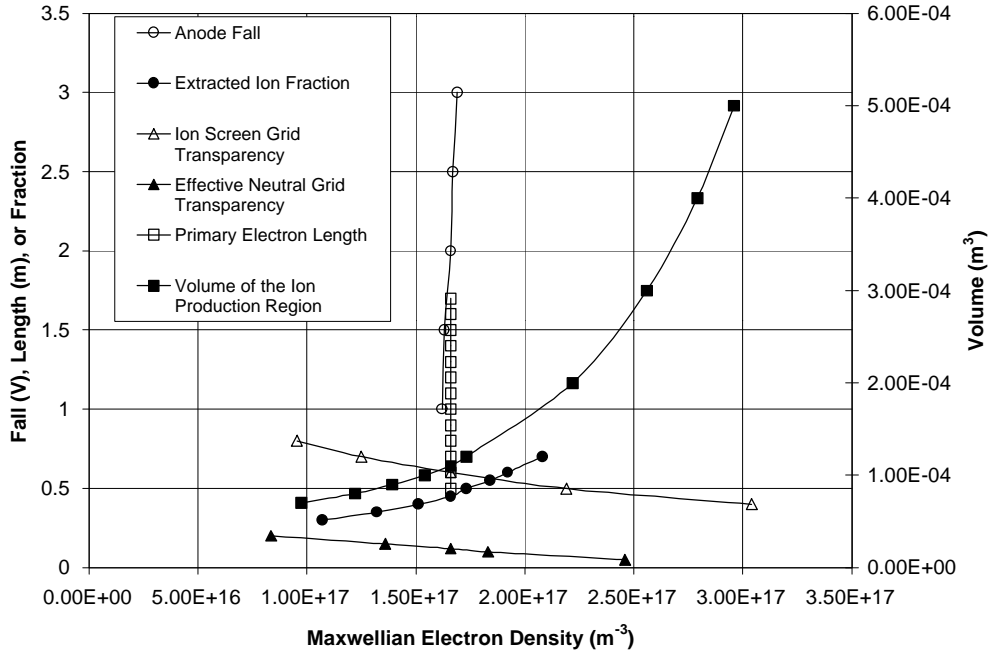


Figure 3.25. Variation of the Maxwellian Electron Density for Changes in Various Parameters

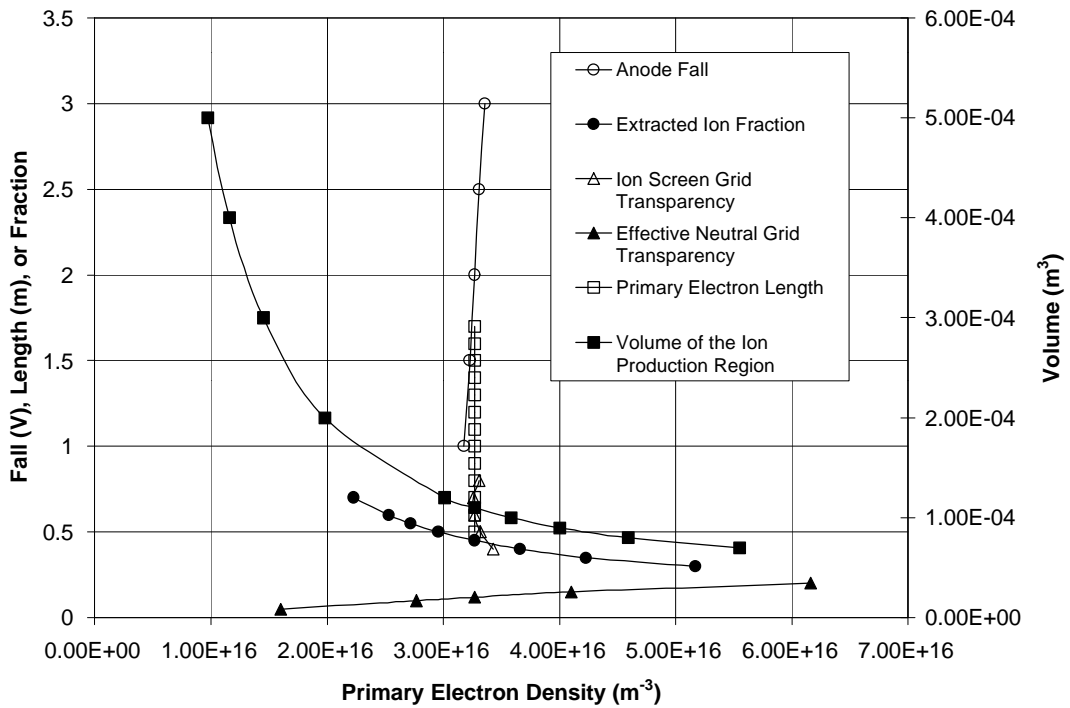


Figure 3.26. Variation of the Primary Electron Density for Changes in Various Parameters

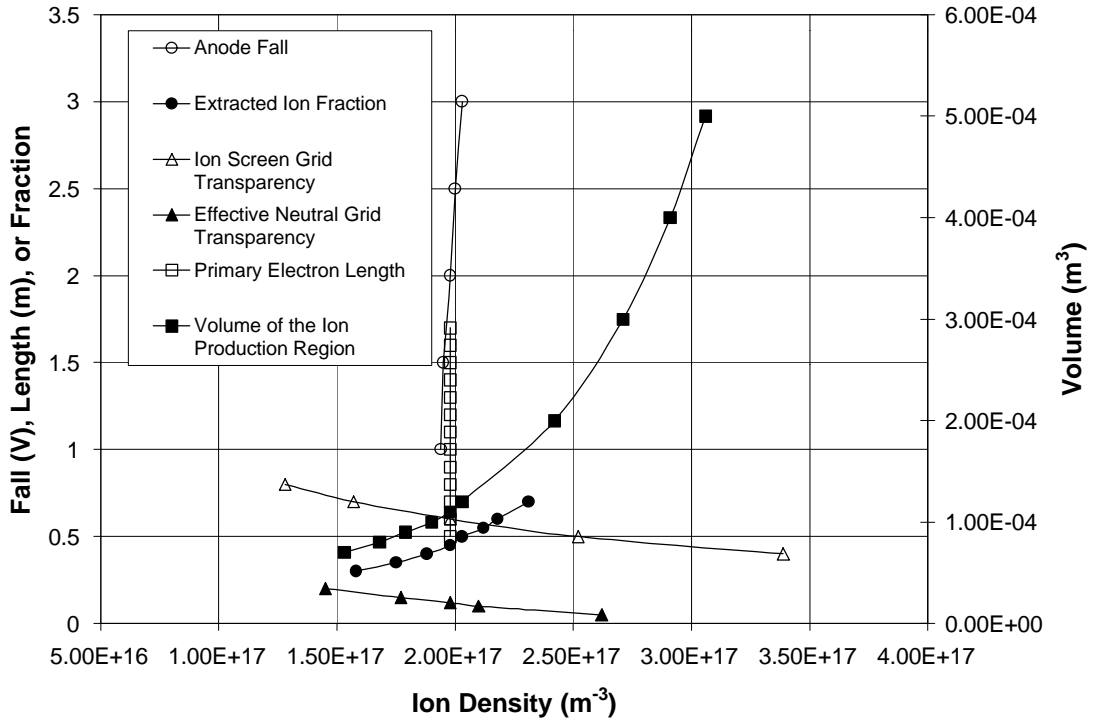


Figure 3.27. Variation of the Ion Density for Changes in Various Parameters

3.2.3 Comparison of Model Results to a SERT II-Type (Culham) Mercury Thruster

In order to determine a comparison between the model predicted here and the values used by Wells *et al.* [38], the parameters were varied as shown in the previous section to attain the region of reasonable solutions. Two important parameters dictated many of the results. These were the ion current to the keeper and the ion current to the anode. If parameters were used that resulted in negative ion currents for the keeper and anode, they were considered not acceptable for the solution. Negative ion currents would require the “burning off” of ions from the surface, which is not a mechanism present in impact ionization thrusters, as mentioned prior.

It is important to note that the model used was designed for the NSTAR ion thruster which had a different configuration than the Culham thruster. In the NSTAR thruster, the anode effectively covered the whole discharge chamber region except for the

cathode and optics. The Culham thruster had the anode mounted on the body of the thruster with a circular rear region called the backplate, which was not electrically connected to the anode or cathode. The Culham thruster also had magnetic pole pieces protruding into the thruster discharge chamber near the cathode and near the optics. The NSTAR thruster has permanent magnets mounted outside of the discharge chamber. The Culham thruster also has a baffle outside of the keeper on the main cathode. This baffle consists of a small circular plate in front of the cathode opening.

While not all of these differences are included in the model presented, the model still can predict several of the values because of the thrusters' basic similarity. The model can easily account for the fact that the Culham thruster is a divergent-field thruster using mercury as a propellant, while the NSTAR thruster is a cusped-field thruster using xenon propellant. Table 3-16 shows the values used in the model of the Culham thruster.

Table 3-16 Values Used in Model of the Culham Thruster

Parameters Held Constant	Respective Values
Discharge Voltage	44 V*
Keeper Voltage	15 V*
Discharge Current	2.02 A*
Beam Current	0.256 A*
Ion Current to Accelerator Grid	0.001 A*
Flow Rate	4.241 sccm*
Extracted Ion Fraction	0.45
Effective Neutral Transparency to Grids	0.12
Screen Grid Ion Transparency	0.6
Area of Grid Beam is Extracted through	0.006642 m ² *
Anode Fall	2 V
Accelerator Fall	150 V
Volume of the Ion Production Region	1.8x10 ⁻⁵ m ²
Primary Electron Length	0.5 m
Screen Grid Ion Current	0.17 A
Power from Ions to Accelerator Grid	0.16 W

*Values taken directly from data reported by Wells *et al.*[38]

3.2.3.1 Comparison of a SERT II-type (Culham) Thruster Plasma-Surface Currents

Table 3-17 gives the ion and electron losses determined by experiment from Wells *et al.* and the losses predicted by the model presented here. The model shows good agreement with the experiment. The main discrepancies are with the electron currents to the anode and the currents to the various components unique to the Culham thruster.

The electron current to the anode was assumed composed of all Maxwellian electrons by Wells *et al.* [38]. However, the presented model accounts for the prediction of primary electrons that make it to the anode with no inelastic collisions. This is an important component to include in predictions since they deposit considerably higher energy than Maxwellian electrons. Wells *et al.* did not have a method for distinguishing between these two types of electrons in their experimentation. However, the total number of electrons to the anode for the experiment of Wells *et al.* and the model is within 3% of each other.

Table 3-17 Comparisons of Ion and Electron Losses in the Culham Thruster

	Wells <i>et al.</i> (A)	Van Noord (A)
Total Ion Current Produced	0.60*	0.57
Cathode Emission Current beyond Keeper	1.47*	1.55
Primary Electrons to Anode		0.67
Maxwellian Electrons to Anode	2.074 ± 0.026	1.45
Total Electron Current to Anode	2.074 ± 0.026	2.12
Ion Current to Anode	0.089 ± 0.009	0.10
Ion Current to Screen Grid	0.166 ± 0.003	0.17
Ion Current to Keeper		0.04
Electron Current to Keeper		0.44
Net Current to Keeper	0.395 ± 0.003	0.40
Screen Pole Electron Current	0.016 ± 0.003	
Screen Pole Ion Current	0.013 ± 0.003	
Backplate Ion Current	0.031 ± 0.003	
Cathode Pole Ion Current	0.100 ± 0.006	
Baffle Ion Current	0.052 ± 0.006	

* Determined indirectly from data

The ion current to the components not located on the NSTAR thruster (the baffle, backplate, screen pole, and cathode pole) totals 0.2 A from Wells *et al.*'s data. In the model presented here, these ions are accounted for in the ion current to the keeper, the ion current to the anode, and that slightly fewer ions are predicted to have been produced than those determined indirectly from Wells *et al.*'s data (fewer ions available to go to components). Despite the differences, the model shows good correlation overall.

It was assumed that the reported cathode current from Wells *et al.* of 1.87 A included the electron current to the keeper. So to determine the amount of electrons entering the discharge chamber these had to be subtracted off. The net current to the keeper is given as 0.395 A, so it is estimated that 0.4 A of electrons are drawn to the keeper. This results in 1.47 A of the electrons entering the discharge chamber. This compares to the 1.55 A predicted by the model.

To determine the total ions produced, one subtracts off the current of the electrons entering the discharge chamber from the total number of electrons going to the anode. Then each electron left represents one ion produced. This results in a 5% difference between the experimental value and the model value.

3.2.3.2 Comparison of Culham Plasma-Surface Power Deposition

The method for determining the power deposition from the particle interactions with the surfaces is similar between Wells' *et al.* approach and the model described in this thesis. The power was determined by currents, plasma potentials, electron temperatures and other parameters outlined in Chapter 2. Wells *et al.* determined many of these parameters experimentally.

Table 3-18 shows the results of the power deposition between the experimentally determined values and the modeled values. The values of the two methods show fair correlation. Most of the modeled values fall within the error bounds specified from the

experimental values. Again the major difference arises with the type of electrons present. If all the electrons are Maxwellian, Wells *et al.* predict a value of 23.3 ± 3.5 W and the model would predict 25.7 W. However, there are a number of primary electrons, which make it to the anode, that are not accounted for with that assumption.

Other differences that arise are a result of different assumptions about the thrusters or the different thruster configurations. The model does not account for ion loss rearward since more recent thrusters have the anode extending rearward. Some of this rearward component is picked up in the model's prediction of ion loss to the keeper. The keeper is more enclosed (by a baffle) in the experimental version than in the type of thruster the model was designed for. The model does not account for electron flux to the screen grid since that is assumed to be minimal.

Table 3-18 Comparison of Experimentally Derived Plasma Power Deposition to Modeled Values

	Wells <i>et al.</i> (W)	Van Noord (W)
Anode and Screen Pole Ion Loss	1.1±0.1	0.90
Loss to Anode from Primary Electrons	NA	25.21
Loss to Anode from Maxwellian Electrons	23.3±3.5*	17.58
Anode and Screen Pole Electron Loss	23.3±3.5*	42.79
Anode and Screen Pole Electron Loss	23.3±3.5*	25.70*
Screen Grid Ion Loss	8.4±0.8	9.06
Screen Grid Electron Loss	1.1±0.1	NA
Accelerator Grid Ion Loss	NA	0.16
Ion Loss Rearward	8.4±0.8	NA
Electron Loss Rearward	<0.4	NA
Ion Loss to Keeper	<0.1	1.55
Electron Loss to Keeper	3.2±0.5	4.89
Total Wall Losses	46.0±6.1	59.35

*Assuming no primary electrons and only Maxwellian electrons

CHAPTER IV

COMPUTER THERMAL MODEL OF An NSTAR ION THRUSTER

In order to validate predictions of the power deposition from charged particles to the surfaces of an ion thruster, it is necessary to develop a thermal model that uses those powers to predict temperatures, which are easier to acquire through experimentation. A model that can predict the temperatures of a thruster will also be very useful for studying the thruster under various conditions and configurations.

In this chapter, a model is developed using an industry program that can compute radiation and conduction heat transfer. The power deposition is applied by user-specified quantities to various nodes. These are estimated based on *a priori* knowledge and are adjusted to fit temperatures with experimental data. Four experimental cases were used for analysis. These included a cold-soak test where the thruster, while not running, is in a liquid nitrogen cooled enclosure. The thruster running at three throttling points (0.5 kW, 1.3 kW, and 2.3 kW) while within the LN₂-cooled enclosure was also examined.

The program was used to demonstrate one way the model could be used for engineering purposes. The program was used to determine the directional heat fluxes for the NSTAR thruster in outer space.

4.1 Model Description

4.1.1 Thermal Model

There are two major modes of heat transfer that take place in the NSTAR thruster. The dominant process is radiation heat transfer [22], but conduction still plays a major role in establishing thruster component temperatures. The interaction of the plasma with the thruster will be discussed later. In order to handle a model of significant size and to study the thermal response of the thruster to various steady-state and periodic external radiation loads over its full range of operating conditions, a computer model was utilized using two well-developed and popular codes.

SINDA (Systems Improved Numerical Differencing Analyzer) by COSMIC analyzes thermal systems represented in electrical analogy, lumped parameter form [73]. The "conductors" based on the conductive and radiative properties of the system are calculated between nodes and then included in a SINDA input file. The equation used for steady-state analysis in SINDA is:

$$0 = Q_i + \sum_{j=1}^{i-1} \left[G_{ji} (T_j^{k+1} - T_i^{k+1}) + H_{ji} \left\{ (T_j^{k+1})^4 - (T_i^{k+1})^4 \right\} \right] + \sum_{j=1}^N \left[G_{ji} (T_j^k - T_i^{k+1}) + H_{ji} \left\{ (T_j^k)^4 - (T_i^{k+1})^4 \right\} \right] \quad (4.1)$$

where Q_i is the heat source/sink for node i , G_{ji} and H_{ji} are the linear and radiation conductors, and T is the temperature at node i or j , and iteration k or $k+1$. This equation is solved by a "successive point" iterative method [73]. The transient equation used is based on an implicit forward-backward differencing method shown in Equation 4.2.

$$\begin{aligned} \frac{2C_i}{\Delta t}(T_i^{n+1} - T_i^n) = 2Q_i + \sum_{j=1}^N \left[G_{ji}(T_j^n - T_i^n) + H_{ji} \left\{ (T_j^n)^4 - (T_i^n)^4 \right\} \right] \\ + \sum_{j=1}^N \left[G_{ji}(T_j^{n+1} - T_i^{n+1}) + H_{ji} \left\{ (T_j^{n+1})^4 - (T_i^{n+1})^4 \right\} \right] \end{aligned} \quad (4.2)$$

In Equation 4.2, the subscripts i and j are the node numbers, and T^n and T^{n+1} are the temperatures at time t and $t+\Delta t$. C_i is the thermal capacitance. For Equations 4.1 and 4.2 the radiation terms are linearized before solution routines are initiated.

The second piece of software used is TRASYS (Thermal Radiation Analyzer SYStem) by COSMIC [74]. TRASYS uses geometry and surface characteristics to provide radiation conductors for SINDA. TRASYS computes the radiation view factors using the Nusselt Sphere and double summation techniques [74]. Both of these calculation methods are based on the equation:

$$F_{ij} = \int_{A_i} \int_{A_j} \frac{\cos \theta_i \cos \theta_j}{\pi r_{ij}^2} dA_j dA_i \quad (4.3)$$

which gives the view factor (F_{ij}) for two finite areas (A_j and A_i) where θ is the angle between the normal of the surface and the direction to the other surface.

Typically in thermal analysis, test-calibrated models are given an 11 • C margin wherein 95% of the temperatures are expected to fall [75]. SINDA has been shown to match an analytical solution of a very simple, warm body radiatively cooled to a heat sink to within 1 • C (which was an absolute error of less than 0.5%) [76]. However, models that are more complex will have a higher degree of uncertainty. Contact resistance is a common reason for the uncertainty. Meshed or perforated surfaces are also known to be extremely difficult to analyze. This is due to the complex shadowing involved when one surface interacts with another through the meshed surface and also the complex radiation

interchange between all these surfaces [75]. The ground screen (screen around the thruster body, which NSTAR nomenclature lists as the plasma screen) temperatures on Oglebay's SINDA model differed by up to 33 • C from experimental values [22]. Since the accuracy of a model is dependent on its complexity, a thermal model is often a balance between being too complex, taking significant modeling and computing time and can result in confusion when interpreting the results, to being too simple and not accurate.

The NSTAR model contains 104 thruster nodes with conductors connecting the nodes for conduction and radiation heat transfer. The thruster is essentially broken up into 4 quadrants. Two of the quadrants are further subdivided in half to accommodate the gimbal pads, which are structural mounting surfaces used to integrate the thruster into a spacecraft. It is the presence of gimbal pads and the neutralizer which prevent the thruster from being modeled as a pure symmetrical body. If it were purely symmetrical, the thruster would only vary in temperature along the axis and not circumferentially. Dividing the thruster into four main quadrants with two of them subdivided for the gimbal pads is the simplest form of modeling which uses the symmetrical nature it does have while accounting for the unsymmetrical elements. Figure 4.1 shows the nodal layout of the thruster. The nodal numbering scheme in this figure for off-axis nodes starts with the lowest number on the bottom (in the quadrant of the neutralizer) and then increases by one for each quadrant in a counterclockwise manner when viewed from the optics end of the thruster. This scheme is true for all the nodes except those on the neutralizer (400's), which are contained only in the one quadrant, and the discharge cathode (1-13), which is divided in half. The discharge cathode and keeper nodes are shown in Figure 4.2.

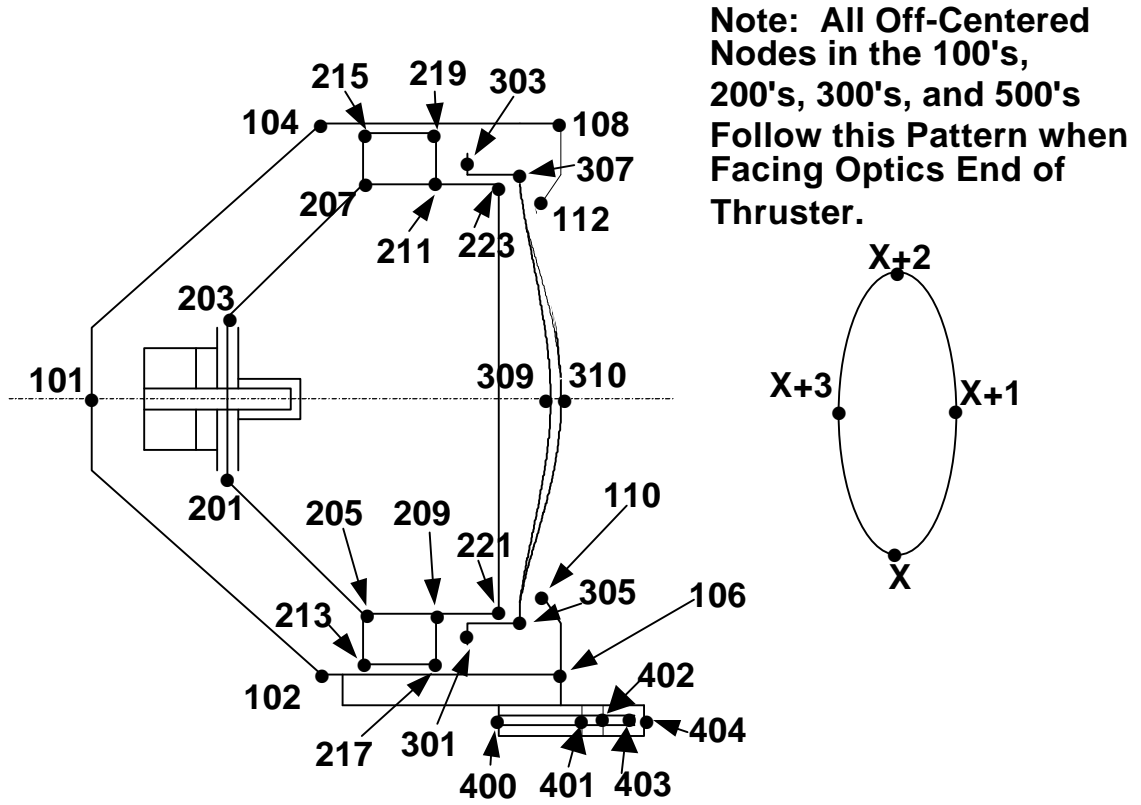


Figure 4.1. NSTAR Ion Thruster Thermal Model Nodal Layout

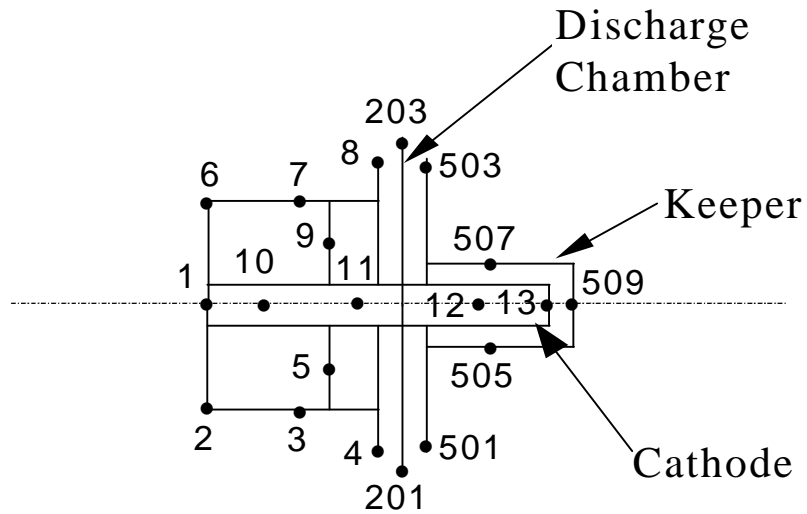


Figure 4.2. NSTAR Cathode Thermal Model Layout

The tests, which were used to calibrate the NSTAR model, took place at the NASA John Glenn Research Center (GRC) (then the Lewis Research Center) [24]. There were two different types of experiments modeled. The first was a cold-soak experiment to subject the thruster to the severe cold conditions of space without any heat source from its operation and the second type was the same cold conditions, but with heat present from its operation. The experimental setup at GRC included the thruster enclosed within a 116-cm-diameter liquid-nitrogen-cooled shroud contained in a 4.6-m-diameter by 19.5-m-long vacuum chamber. Figure 4.3 depicts the setup of the shroud in the vacuum chamber. The tubes carrying the liquid nitrogen snaked circumferentially around the outside of the shroud. The open end of the shroud was closed off by a door that did not have any direct contact with the liquid-nitrogen, but was painted black on the inside and cooled by the rest of the shroud through radiation. In the experiment used for the steady-state analysis, the rear of the shroud was cooled with liquid nitrogen, but not in the transient case. A ring piece was located close to the front (optics end) of the thruster face and was cooled through conduction with the cylindrical part of the shroud. It was used to minimize the interaction between the thruster and the vacuum chamber wall. The shroud was made of stainless steel and painted with a commercial, high-temperature, fireplace flat black paint with a measured emissivity of 0.9.

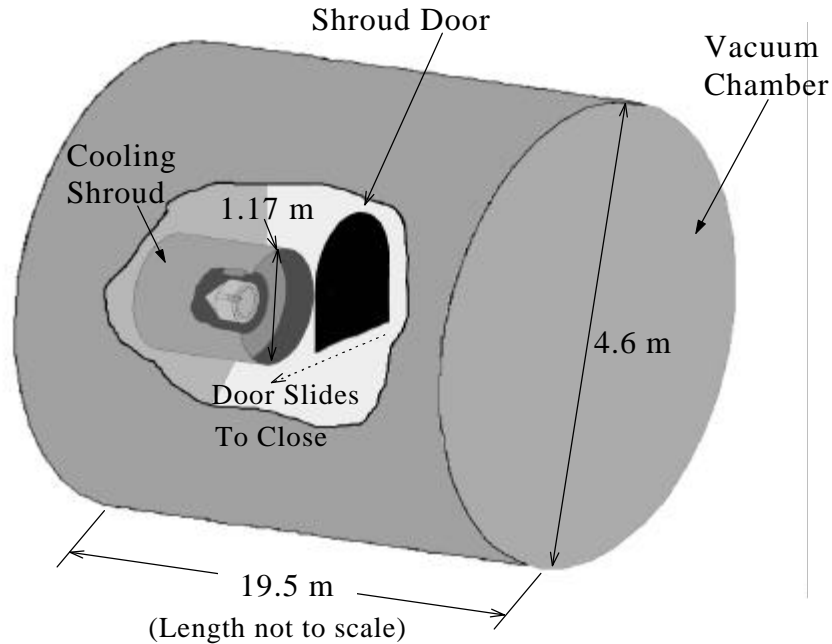


Figure 4.3. Experimental Setup of Cooling Shroud in Vacuum Tank

The model used temperature measurements along the shroud and tank walls to establish boundary conditions. These boundary nodes consisted of 37 nodes making up the shroud and experimental setup, and 6 nodes for the tank wall. There were several thermocouples used to establish these boundary conditions. The vacuum tank had two thermocouples placed on opposite sides of the wall's circumference and about half way from each end. The main thermocouples used on the shroud are depicted in Figure 4.4, which also shows the surfaces used in the TRASYS form factor analysis. The thermocouples were mostly Type K with a few Type R for higher temperature regions. Type K are rated with an accuracy of 2.2 °C or 0.75% and Type R are rated with an accuracy of 1.5 °C or 0.25%. The larger value will determine the accuracy, so for most of the thruster thermocouples the accuracy will be between 2 and 5 °C. The thermocouples, which were on the outside of the discharge chamber, were attached magnetically while the

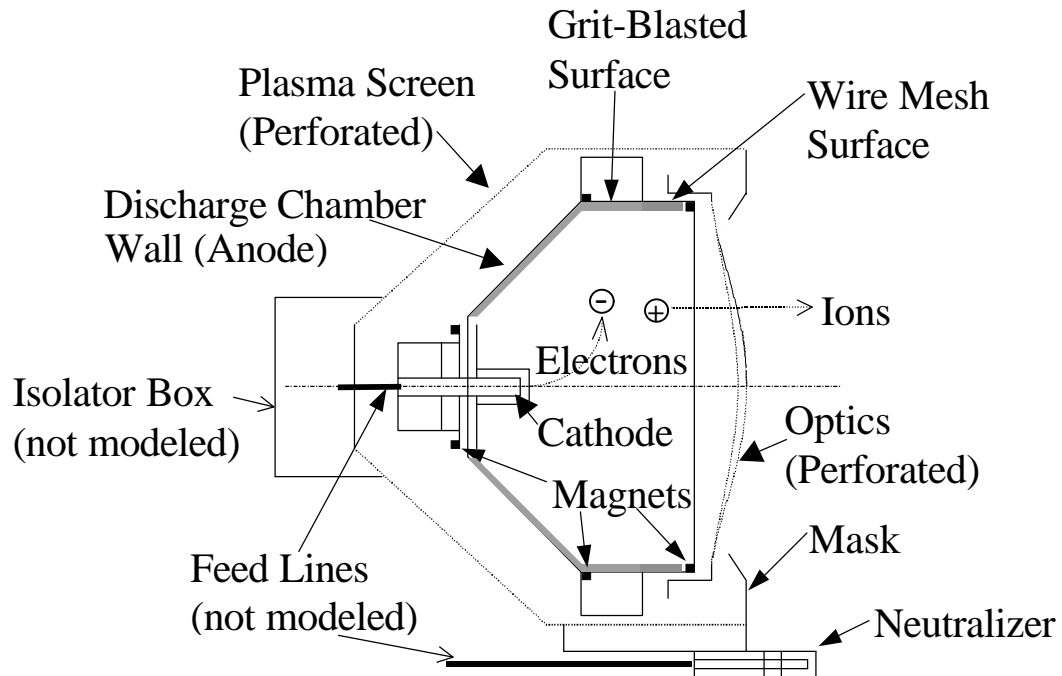


Figure 4.5. NSTAR Thruster Layout

Since radiation is the major form of heat transfer within the thruster, accurate surface property values are very important. Changing materials or surface properties could modify the thermal characteristics of the thruster significantly. These properties could also change over the life of the thruster further complicating matters. For this model the emissivities of materials were assumed constant throughout the temperature range examined; a valid assumption for the conditions experienced by the thruster. Emissivities in the infrared surface temperature regime were obtained from published sources and also from experiments conducted with components of the NSTAR thruster (Table 4-1) [19,49,77,78]. Emissivities that could not be determined were set to Oglebay's value of 0.1 [22]. Joint (contact) conductances were modeled with a constant conductivity of $0.0057 \text{ W/cm}^2 \text{ }^\circ\text{C}$ based on experiments [22]. All other material

properties used in the model are listed in Table 4-1. The grit-blasted surfaces referred to in Table 4-1 are on the inside of the discharge chamber and are shown by the shaded pattern in Figure 4.5. The meshed surface is a stainless steel mesh laid on top of the discharge chamber surface near the optics end and is shown with a grid pattern in Figure 4.5.

Table 4-1 Assumed Physical Properties Of Ion Thruster Materials

Material	Density g/cm ³	Heat Capacity cal/g °C	Conductivity W/cm °C	Emissivity
Aluminum 5052	2.68	0.20	1.37	0.14 0.30 ^a
Pure Titanium	4.43	0.15	0.2	0.23 0.4 ^a
Carbon Steel	7.81	0.13	0.60	Not Needed
304 Stainless	7.92	0.125	0.20	0.11 0.27 ^a 0.5 ^b
Molybdenum	10.19	0.20	1.20	0.2
Tantalum	16.16	0.035	0.60	0.1
Tungsten	19.38	0.035	1.50	0.1
Alumina	3.79	0.20	0.17	0.3
Kovar	8.36	0.105	0.15	0.1
6Al-4V Titanium	4.43	0.15	0.10	0.15

^a Grit blasted surface

^b Meshed surface

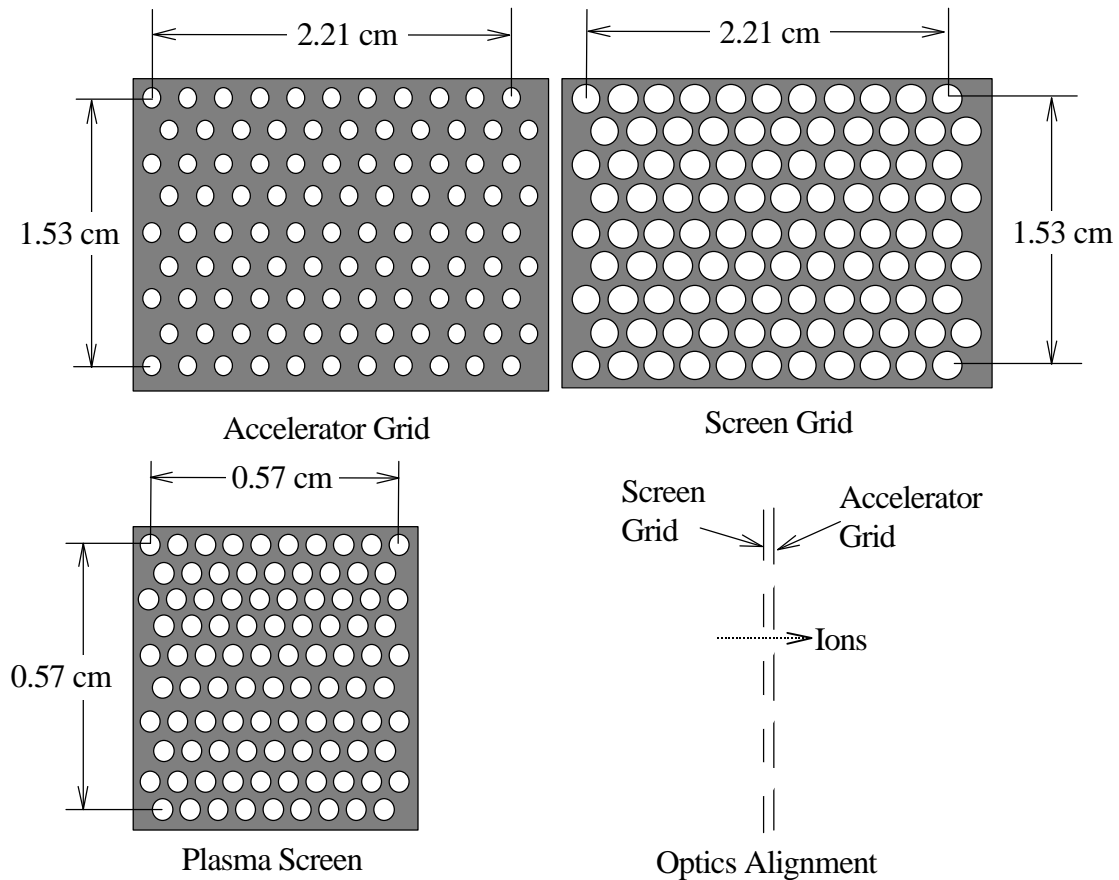


Figure 4.6. Perforated Surfaces on Ion Thruster

Another surface characteristic that had to be modeled was the perforated surface, which TRASYS was not designed to model. These surfaces are shown in Figure 4.5 as dashed lines. Figure 4.6 shows a sampling of these surfaces. The plasma screen is located on the exterior of the thruster and the accelerator and screen grids are part of the ion optics, with the outermost grid being the accelerator grid. To approximate these surfaces, transmissivity values were assigned to allow the appropriate percentage of incident energy to pass through all perforated surfaces. The value used for the transmissivity corresponded to the open area fraction of the perforated surface. However, it is not clear how accurate this assumption is for modeling these surfaces. For example, transmissive

surfaces in series will artificially block radiation that would normally travel through the aligned open areas of two perforated surfaces.

Another approach in treating perforated surfaces is to model them as checkered surfaces. In this approach, the amount of open area in the checkered surface corresponded to the same amount of open area present in the perforated surface. Figure 4.7 shows the checkered surface approximation used to model the grids. The screen grid is depicted as black such that the non-black area corresponds to the same amount of area in the actual screen grid that is open. The accelerator grid is shown as gray, but also includes the area shown by the black screen grid. This then leaves the white area to be the open area that is the same as the actual accelerator grid. This white area is also the aligned open area that allows the appropriate amount of interior thruster radiation to pass through the grids to the exterior without obstruction. The grids of the engine were modeled here both as transmissive surfaces and as coarse checkered surfaces. (Here “coarse” refers to the large checkered sections, “fine” would mean many small sections).

The accuracy of these various thermophysical properties in the model were established using comparisons between the model and cold soak experiments with the non-operating thruster in the shroud.

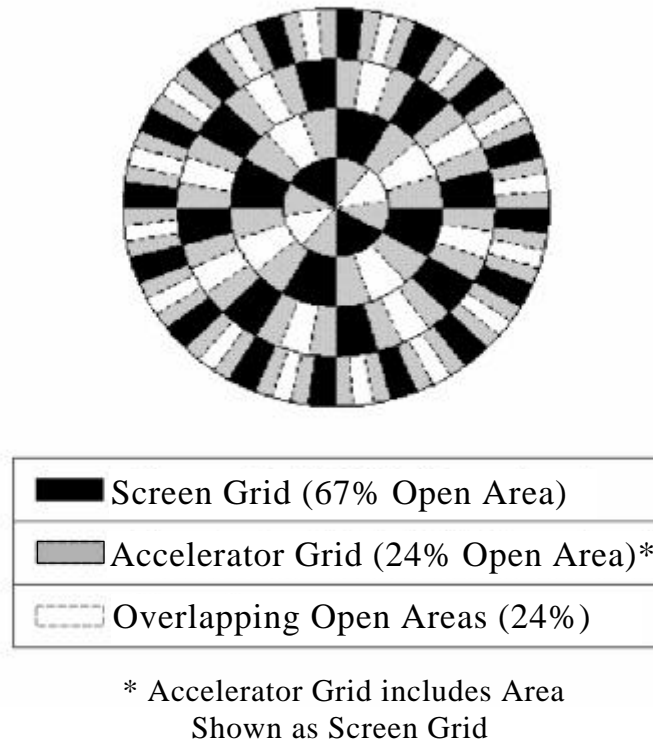


Figure 4.7. Modeling Approximation of Ion Optics used in TRASYS

4.1.2 Self-Heating due to Plasma Interaction

One of the more complex aspects of the thruster model is ascertaining the amount of thruster self-heating from the plasma interaction with surfaces. In order to determine analytically the amount of heat that is produced by the plasma, several characteristics must be well understood. One of these characteristics is the precise location of the deposition of charged particles on the various surfaces (i.e. what parts of the anode are receiving the most electrons). Other characteristics include the particle temperatures and the rate they

are deposited into the surface in the discharge chamber. These were discussed at length in the previous chapters.

The alternative use for the model in this chapter entailed using heat-flux data from past work and then adjusting the values until the temperatures in the model agreed with the experimental data [21,22]. This will enable comparison to the analytically predicted values. However, the previous thrusters were somewhat different from the NSTAR thruster in that they were not ring-cusp thrusters with xenon propellant, but were divergent field thrusters using mercury propellant. This changes the thermal characteristics in several ways.

First, since the magnetic field is a ring cusp, the heating from the plasma will be in different locations. For example, Oglebay and Wen report the power deposited in the front and back portion of the anode [21,22]. However, the electrons will most likely be deposited differently since the two different types of thrusters have different magnetic field lines that the electrons follow.

Second, changing propellants also has a significant effect. The mercury-based thrusters had to have vaporizers to make sure the mercury entered as a vapor. Xenon also has an ionization potential of 12.13 eV compared to Mercury's 10.44 eV. This changes the amount of energy deposited when an ion recombines at a surface.

Third, the physical layout of the thrusters are also different. The NSTAR thruster has a conical rear portion and the anode consists of the entire discharge chamber wall, while the other thrusters have an anode, which is not the entire wall, mounted to the engine body with gaps which cause heating of the engine body.

Although the comparison is useful, values used from Oglebay and Wen for the power deposited on the thruster are only rough starting points and would not be expected to give an accurate description of the NSTAR thruster power deposition since the thrusters have the differences mentioned above.

The initial estimate for power deposited into the NSTAR thruster was determined by considering only the components the previous thrusters had in common with the current thruster; the rest were disregarded (most of which had power deposited from processes unique to using mercury). The values were then interpolated or extrapolated from the previous thruster based on beam current, which is the current used by Oglebay to scale [22]. Table 4-2 gives the final values used by Wen and Ogelbay [21,22]. Several of Wen's final heating values changed 20-67% from his initial estimates [21]. Table 4-3 then contains the *a priori* and final heating power values used for the NSTAR thruster. The final values were arrived at after adjusting the *a priori* values based on the temperature discrepancies between the model and experiment.

Table 4-2 Self-Heating Values used For Wen and Oglebay's Ion Thrusters

Beam Current:	Wen		Oglebay	
	0.5 A	1.0 A	1.0 A	1.9 A
	Power (W)	Power (W)	Power (W)	Power (W)
Main Vaporizer			7.3	7.3
Cathode Vaporizer			4.6	7.6
Neutralizer Vaporizer			3.0	4.9
Neutrailer Tip			2.0	3.4
Cathode Tip	12.6	15.4	13.4	25.6
Accelerator Grid	10.1	11.8	11.6	19.6
Screen Grid	5.9	11.6	11.6	19.6
Anode, rear	14.7	28.8	17.6	35.2
Anode, front	28.1	44.2	35.2	64.6
Engine Body, rear			42.8	70.4
Engine Body, front			9.2	15.6
Baseplate	16.1	36.7	36.8	46.8
Pole	9.9	18.2	14.4	24.0
Keeper Baffle	11.2	20.6		
Pole Piece (side)	14.0	31.1		
Housing	13.1	20.2		
Total	135.7	238.6	209.5	344.6

Table 4-3 A Priori Values Based on Wen and Oglebay's Values and Final Adjusted Values

Nodes	Description	A Priori Values			Final Values		
		0.5 kW 0.56 A	1.3 kW 0.98 A	2.3 kW 1.75 A	0.5 kW 0.56 A	1.3 kW 0.98 A	2.3 kW 1.75 A
		Power (W)	Power (W)	Power (W)	Power (W)	Power (W)	Power (W)
13	Cathode Tip	7.4	13.8	23.6	13.9	18.0	20.0
201-4	Discharge Chamber , rear	20.0	36.0	45.1	20.0	33.0	42.0
205-8	Anode,rear	10.0	28.0	32.3	48.0	44.0	50.0
209-12	Anode,Middle	25.0	25.0	59.7	18.0	38.0	72.0
221-24	Anode Front, (near grids)	16.0	30.4	56.8	32.4	46.0	72.0
309	Screen Grid	8.0	11.5	18.3	5.5	8.7	16.4
310	Accelerator Grid	8.0	11.5	18.3	0.2	0.6	1.3
403	Neutralizer Tip	1.3	2.0	3.2	21.2	21.9	22.6
404	Neut. Keeper				19.0	15.0	13.7
501-4	Main Keeper	12.0	38.0	34.7	3.6	7.0	29.6
Total		107.7	196.2	292.0	181.8	232.2	339.6

4.2 Model Results And Discussion

4.2.1 Cold-Soak Case

The computer model was first compared to the cold-soak test that was done at GRC. The temperatures for the boundary conditions in the model consisted of monitored shroud temperatures.

Figure 4.8 shows a cross sectional view of the NSTAR thruster with the temperatures determined experimentally and by the SINDA computer model for the steady-state case. Steady-state was defined as when the temperature of the thruster was changing less than 3 °C per hour. Steady-state was reached after about 10 hours and then reported values were taken at about 24 hours after the beginning of the test [24]. The two temperatures derived from the computer model correspond to different approaches to modeling the optics (checkered vs. transmissive). The SINDA model accurately predicted all thermocouple values within 5 °C except at six nodes. The neutralizer tip is within 6 °C. Three of the six on the optics support ring are within 8 °C. The last two, on the edge of the mask and front edge of the thruster, are within 10 °C.

The application of the model to the cold-soak experiment is necessary to determine the accuracy of the thermophysical properties of the thruster (radiative and conductive) independent of the plasma self-heating. It is difficult to determine the discrepancy of the temperatures in the mask area. This may reflect the difficulty in determining the contact resistance between the mask and the rest of the thruster.

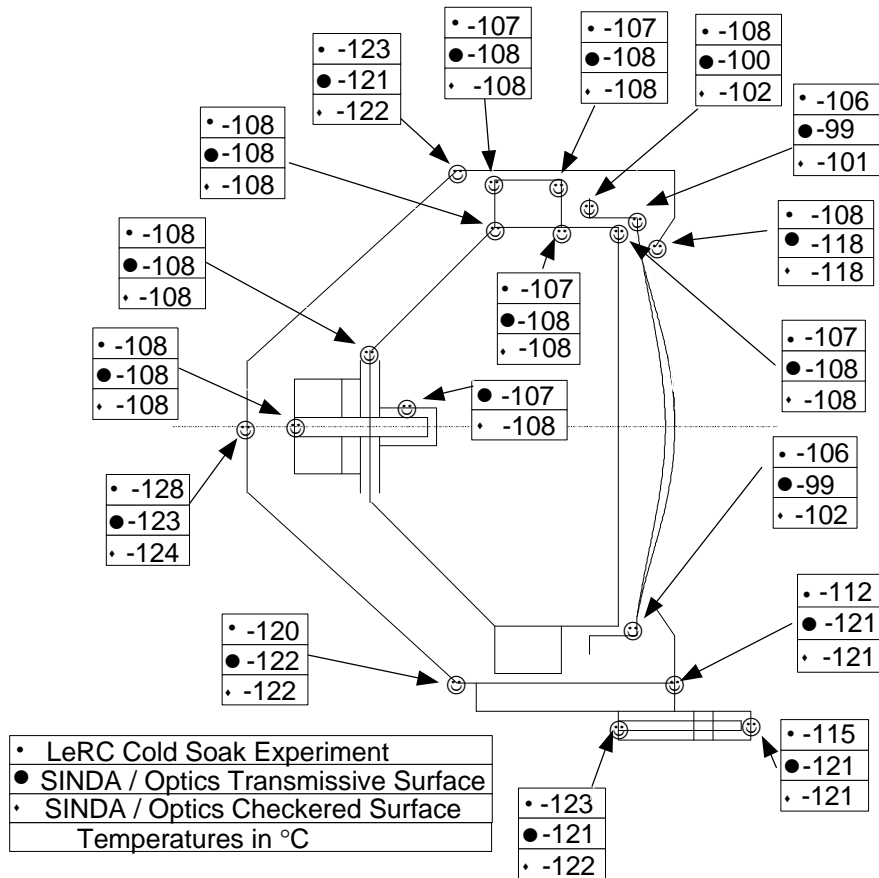


Figure 4.8. NSTAR Thruster Steady State Temperatures under Cold Soak Conditions

The effect of changing the method of modeling the optics appears to be minimal in this case. Most of the temperatures changed by only a degree or two Celsius. The most drastic change in temperature was in the optics, (3 °C). This would indicate that modeling the surface as transmissive is sufficient for the conditions considered in the cold soak test simulation. Using a checkered surface can improve the temperature data slightly, but it comes at the cost of time to setup such surfaces. The transmissive surface can be used and only the transmissivity needs to be declared for a large surface; however, the checkered surfaces require the position and dimensions for each checker to be added separately. Unless an automated setup was designed, a large checkered area could require significant time for a slight improvement in temperatures.

4.2.2 Transient Analysis

The NSTAR thruster has also been modeled in SINDA to predict its transient behavior. The temperatures of the shroud that were used as boundary conditions are shown in Figure 4.9. The experiment obtaining the transient values did not run to steady-state and was performed prior to the experiment which was used for its steady-state values. The transient experiment did not have a door on the shroud, nor was there liquid nitrogen cooling the rear of the shroud, and it only used two thermocouples to measure shroud temperatures. These thermocouples were located on opposite sides of the shroud wall's circumference and about halfway from each end. Figure 4.10, Figure 4.11 and Figure 4.12 show a comparison between experimentally determined data and the SINDA model with the optics modeled as transmissive surfaces.

The predicted results from SINDA agree to within 10 °C for all of the nodes except 112 (mask), 400 (neutralizer rear), 102 and 104 (plasma screen). A major cause of the differences with the neutralizer temperatures is a result of the simple neutralizer model used at the time. The areas of greatest discrepancy tend to be along the plasma screen and mask. Again, this may represent the difficulty in determining some of the contact resistances in the system and in modeling perforated surfaces. In Figure 4.10 the nodes corresponding to the plasma screen (Nodes in the 100's) increase in temperature unexpectedly during 300 to 400 minutes. This is due to an increase in the shroud temperatures shown in Figure 4.9. The modeled plasma screen surfaces in SINDA are more sensitive to the shroud temperatures than the actual plasma screen surfaces in the experiment. This sensitivity could be due to a difference in thermal capacitance between the modeled and the actual plasma screen surfaces and it could also be affected by the method of modeling the perforated surface.

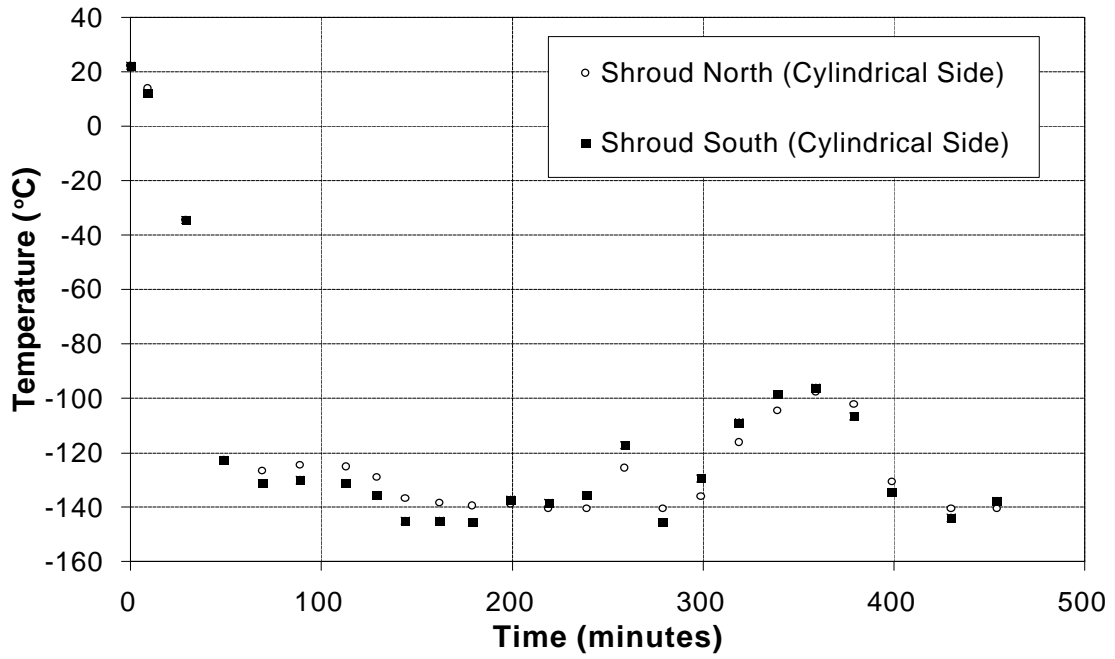


Figure 4.9. Transient Temperatures of Shroud in Cold Soak Experiment (Experiment Temperatures $\pm 5^\circ\text{C}$)

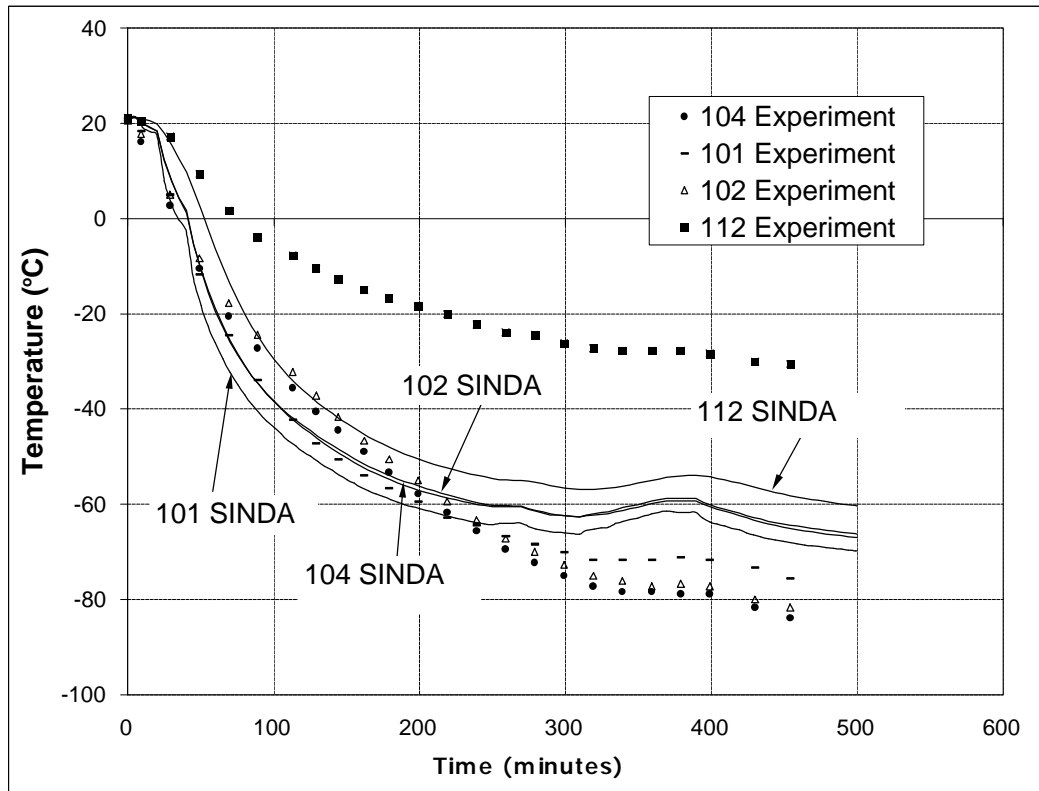


Figure 4.10. Transient Cold Soak Experiment Compared to SINDA model of NSTAR Thruster for Plasma Screen Nodes (Experiment Temperatures $\pm 5^\circ\text{C}$)

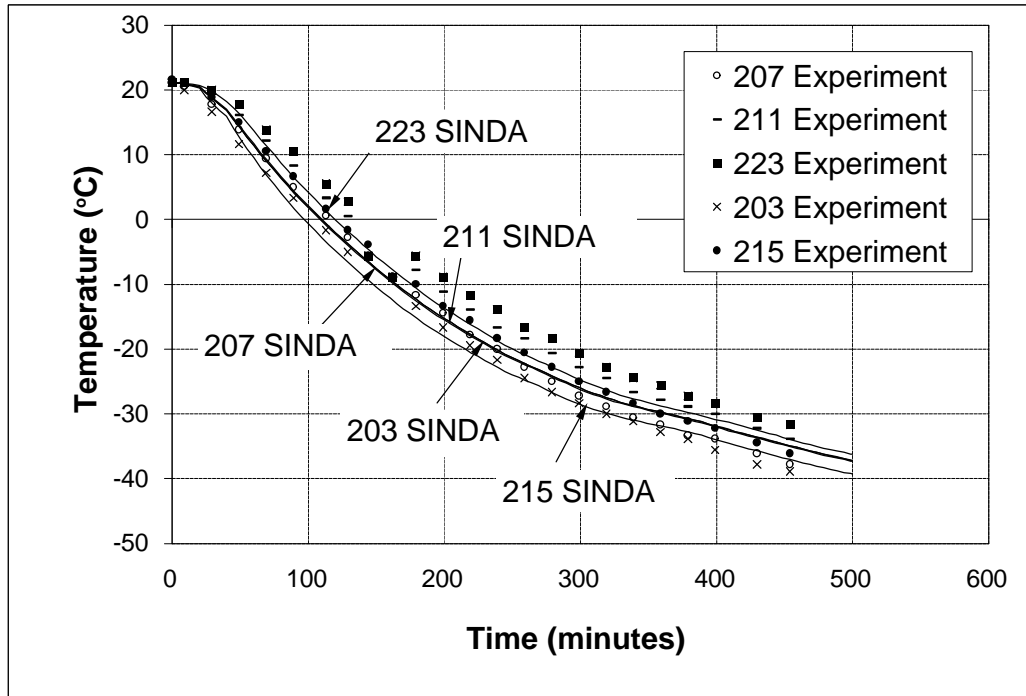


Figure 4.11. Transient Cold Soak Experiment Compared to SINDA model of NSTAR Thruster for Discharge Chamber Nodes (Experiment Temperatures $\pm 5^\circ\text{C}$)

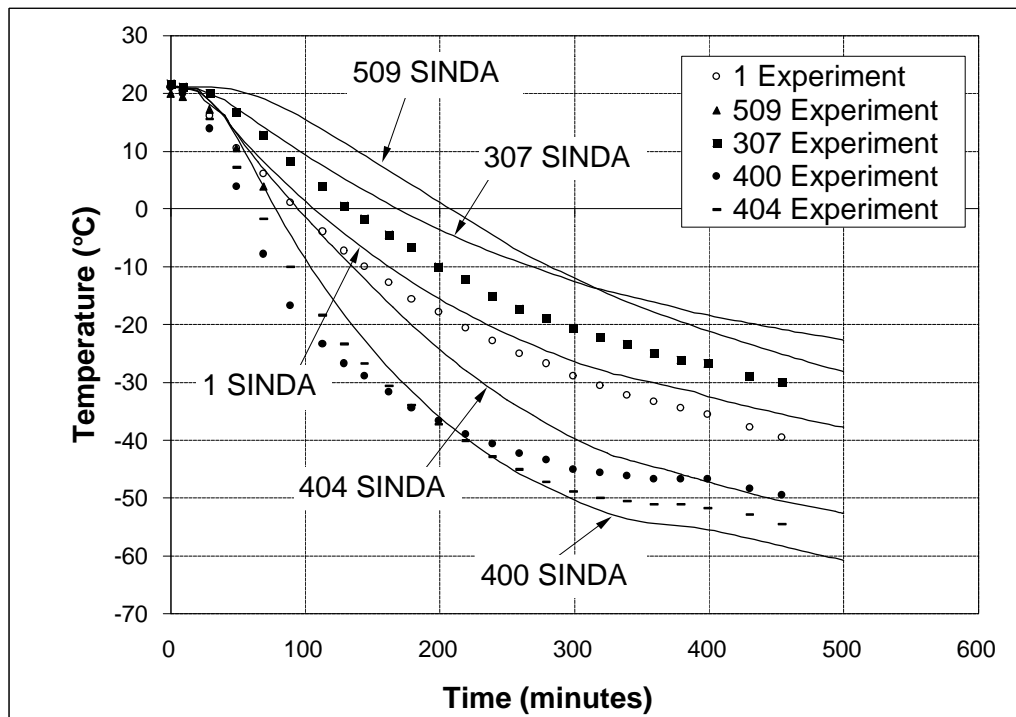


Figure 4.12. Transient Cold-Soak Experiment Compared to SINDA model of NSTAR Thruster (Experiment Temperatures $\pm 5^\circ\text{C}$)

Figure 4.11 shows that the agreement of temperatures in the discharge chamber area is very good. The temperatures follow within 5 °C throughout the test. The accuracy in the discharge chamber surface temperatures is crucial since most of the important components in the thruster are on or near this surface. The model also shows that the discharge chamber is interacting with its surroundings (the shroud) as in the experiment. The energy exchange between the plasma screen and the discharge chamber is of less influence than between the shroud and the discharge chamber since the plasma screen is perforated and hence only a portion of its surface interacts with the discharge chamber, and because the emissivity of the screen (0.1) is considerably lower than that of the shroud (0.9). Table 4-4 shows this interaction for the cold-soak case. The energy exchange for both the plasma screen and the discharge chamber with the shroud is approximately an order of magnitude more than it is with each other. Thus, although the temperatures of some outer components such as the plasma screen may be less accurate, as shown in Figure 4.10 and Figure 4.12, their impact on the discharge chamber is minimal.

Table 4-4 Energy Interchange between Plasma Screen, Discharge Chamber and Environment for the Cold-Soak Experiment

From Node	Transmissive Optics				Checked Optics			
	To Plasma Screen (W)	To Discharge Chamber (W)	To Shroud and Tank (W)	% To Shroud	To Plasma Screen (W)	To Discharge Chamber (W)	To Shroud and Tank (W)	% To Shroud
101		0.011	0.267	96.0		0.011	0.268	96.1
102		0.051	0.234	82.1		0.055	0.235	81.0
104		0.011	0.200	94.8		0.012	0.201	94.4
108		0.008	0.283	97.3		0.009	0.285	96.9
112		0.0004	0.057	98.6		0.0005	0.058	99.1
203	0.003		0.042	93.3	0.003		0.047	94.0
207	0.005		0.088	94.6	0.006		0.099	94.3
211	0.004		0.039	90.7	0.004		0.049	92.5
215	0.004		0.035	89.7	0.004		0.036	90.0
219	0.005		0.030	85.7	0.005		0.030	85.7
223	0.001		0.022	95.7	0.001		0.030	96.8

4.2.3 Thruster Operating at Throttling Points of 0.5, 1.3 and 2.3 kW

The next step was to examine an operating thruster. Figure 4.13 - Figure 4.15 give the temperatures on the NSTAR thruster when it was operating at the levels of 2.3 kW, 1.3 kW, and 0.5 kW as well as the temperatures for the SINDA model for both types of optic surface representations. A few of the thermocouples were not operating for some of the experiments, so the figures will not have data for certain nodes.

As mentioned, *a priori* values of self-heating were used and then adjusted to correspond to the experimental data (Table 4-3). The temperatures of the discharge chamber were 30-40 °C cooler than the experiment using the *a priori* self-heating values prior to adjusting. The self-heating values determined after adjusting are given in Table 4-3.

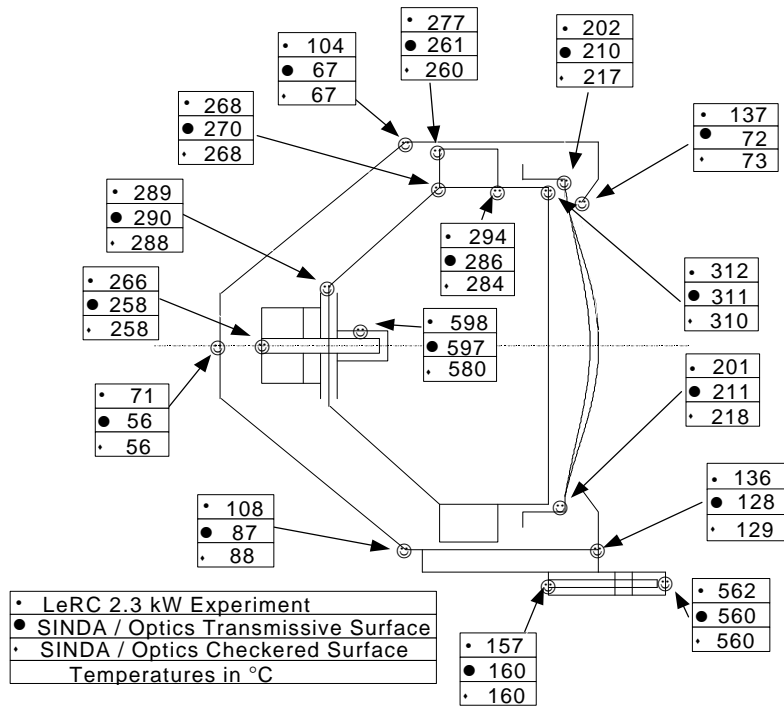


Figure 4.13. NSTAR Thruster Steady State Temperatures for Throttling at 2.3 kW

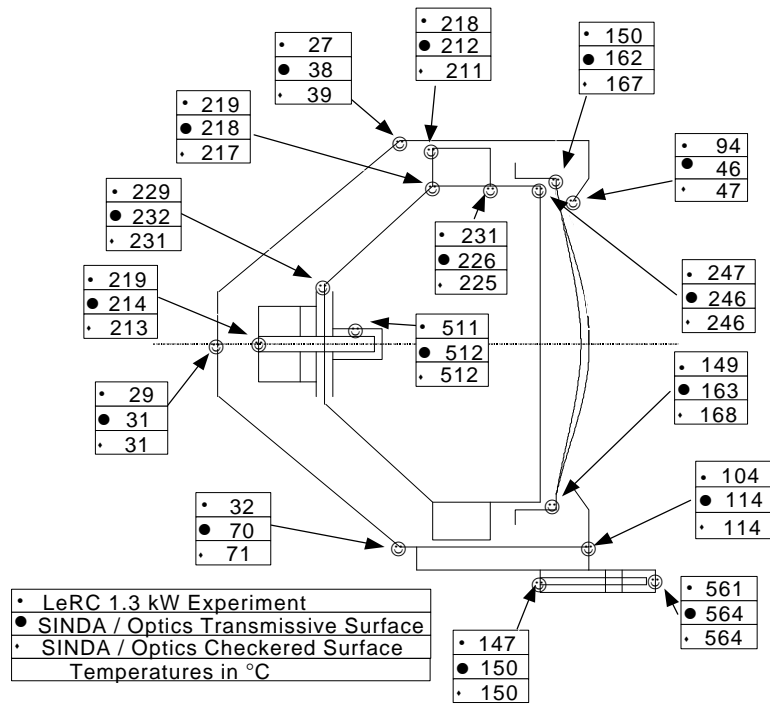


Figure 4.14. NSTAR Thruster Steady State Temperatures for Throttling at 1.3 kW

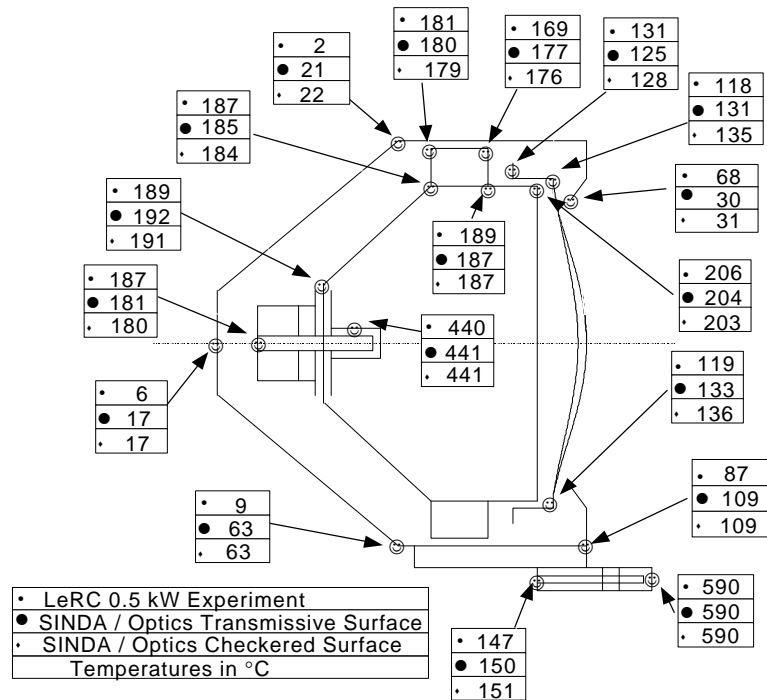


Figure 4.15. NSTAR Thruster Steady State Temperatures for Throttling at 0.5 kW

The temperatures of the anode in the discharge chamber are within 5 °C of the experimental data for all the throttling points except for the node 211 in the 2.3 kW case, which is 8-10 °C different. The nodes on the support ring (215 and 219) are within 8 °C for the 0.5 kW and 1.3 kW throttling points; however, node 215 is 17 °C different for the 2.3 kW case. The optics support is within 19 °C for all throttling points. The base of the main cathode assembly is within 8 °C for all cases. The plasma screen has some of the worst temperature fits varying from the experimental data by a few degrees to 50 °C. The mask is as much as 65 °C cooler than experimentally determined.

The discrepancy of the plasma screen, mask, and optics assembly again is likely caused by the difficulty in modeling a finely perforated surface and modeling contact resistances. The coupling between the discharge chamber and the plasma screen is

through isolators that have a high number of contact points. It is also important to note that the thermocouple on the optics support ring where it connects with the dished optics is on the ring connected to the accelerator grid. The SINDA model shows that the screen grid is hotter than the accelerator grid by 30-60 °C. However, the SINDA model depicts this node as a combination of the two support rings (one for each grid). This could account for the SINDA model predicting this node 12-15 °C warmer than the experiment.

Similar to the cold-soak case, the interaction between the discharge chamber and the environment is accurate. Table 4-5 shows the energy exchange between the plasma screen, discharge chamber and shroud for the 2.3 kW case. The percentage of energy exchange between the discharge chamber and the shroud is lower than the cold-soak case, but still 67-85% of the energy exchange is with the shroud. The temperature of the plasma screen has a larger influence than in the cold-soak case, but it is still the outer environment that has the greatest impact on the discharge chamber. Therefore, this model should give an accurate prediction of the temperatures of the discharge chamber and its components under varying conditions.

4.2.4 Model Prediction for Directional Heat Dissipation

Once the model is calibrated, it can be used to predict various thruster-operating scenarios. One of the major concerns is to know the direction heat is flowing out of the thruster and in particular, the amount of heat which will be directed toward a spacecraft. To estimate the directional heat fluxes, the thruster was modeled in a box maintained at a temperature of -273 °C and an emissivity of 1.0 (Figure 4.16). The thruster was then given the heat distribution corresponding to the 2.3 kW throttle point.

Table 4-5 Energy Interchange Between Plasma Screen, Discharge Chamber and Environment for the 2.3 kW Throttling Level

From Node	Transmissive Optics				Checked Optics			
	To Plasma Screen (W)	To Discharge Chamber (W)	To Shroud and Tank (W)	% To Shroud	To Plasma Screen (W)	To Discharge Chamber (W)	To Shroud and Tank (W)	% To Shroud
101		3.72	7.07	65.5		3.71	7.12	65.7
102		4.06	6.68	62.2		4.04	6.73	62.5
104		4.00	5.00	55.6		4.01	5.06	55.8
108		3.27	4.13	55.8		3.60	4.25	54.1
112		0.19	0.51	72.9		0.24	0.53	68.8
203	0.99		5.58	84.9	1.03		5.94	85.2
207	1.83		10.00	84.5	1.95		11.00	84.9
211	1.67		4.55	73.2	1.78		5.47	75.4
215	1.36		4.23	75.7	1.36		4.22	75.6
219	1.58		3.20	66.9	1.57		3.19	67.0
223	0.58		3.03	83.9	0.73		4.12	84.9

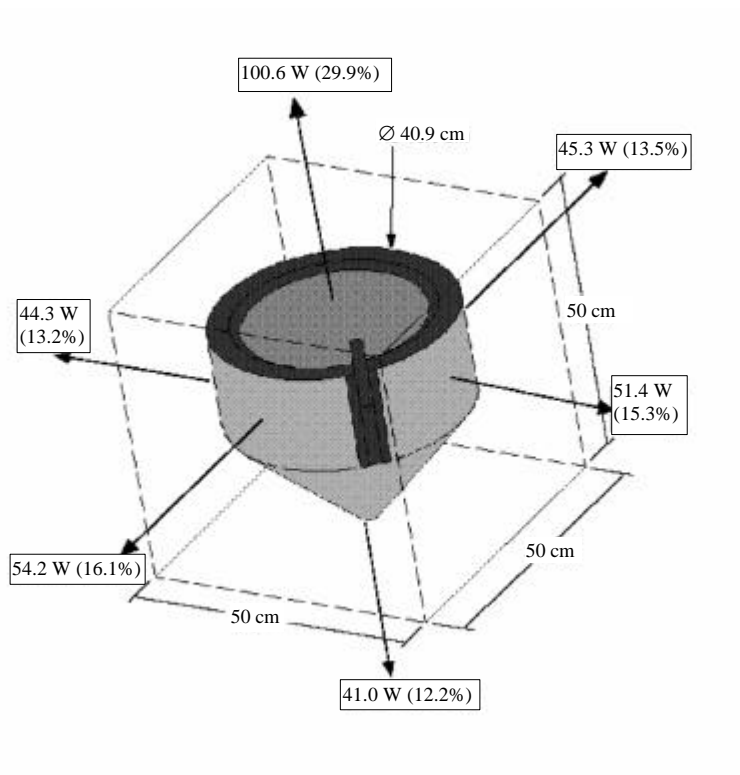


Figure 4.16. Heat Flux from NSTAR Thruster to Box Sides with Space Conditions

It can be seen on Figure 4.16 that a majority of the heat is expelled through the optics of the engine. It should be noted that the effect of the plasma is only included as the heat applied to thruster components and the power through the grids does not include the ion beam power. The sides of the thruster are uniform in power distribution with a slight variation caused by the neutralizer with the rear having the lowest amount of power lost thermally. However, these values would change if an object of finite temperature was on any side of the thruster. If a large spacecraft surface was behind the thruster at a much higher temperature than absolute zero, the amount of heat flux in that direction would be drastically reduced. So thermally, it appears that the thruster will have only a small impact on the spacecraft located behind it.

Since a majority of the heat transfer away from the thruster is through the optics, the direction the optics face will have the most effect on the thruster temperatures. If the thruster optics were facing the sun the thruster temperatures would be increased more than when facing other directions (if the sun exposed areas were similar in dimensions). However, the thruster will be cooled the most when the optics are facing towards the cold of space. What the thruster optics will be facing will determine what the emissivity should be for the surface. If the thruster needs to be cooled and it's optics are facing space, increasing the emissivity of the discharge chamber surface through a process such as grit-blasting would be desired. However, if the thruster was going to be positioned with the optics towards the sun a majority of the time, it would be desired to have the inside of the discharge chamber as polished as possible to minimize solar heating.

4.3 Computer Model Conclusions

The SINDA thermal model developed accurately models the NSTAR thruster discharge chamber and components to within 10 °C for several different throttling levels and conditions. There is a larger discrepancy with the temperatures on the plasma screen and mask. However, it has been shown that this has minimal effect on the temperatures of the discharge chamber and its components. There is still an accurate representation of the interaction between the inner surfaces and the environment. Changing the discharge chamber whether by a material change or a change in its layout will have the greatest effect on the thruster temperatures. The plasma screen and neutralizer were shown to be of lesser importance to the thruster thermal environment.

Limitations of the model include approximating perforated surfaces and modeling of contact resistance. There are no thermal tools currently available to model finely perforated surfaces. Not only is the determination of radiation view factors more difficult, calculating the conduction along the material is also more challenging. Some work has been done to further approximate the perforated surface. The methods used here included modeling the surface as having a transmissivity equal to the open area fraction, and creating a coarse checkered pattern of appropriate open area. While the dominant form of heat transfer is radiation, it was shown that contact resistance plays a significant role in the connection of the discharge chamber to the plasma screen via conduction. Currently, the best way to model contact resistance for a particular case is to estimate it using published data and then adjust the model at those points to the temperatures found experimentally.

The self-heating terms were developed from experimental temperature data. The model is now capable of being integrated into various environments. It can be used to

investigate spacecraft integration issues and evaluate proposed design changes from a thermal impact point-of-view.

CHAPTER V

EVALUATING THE NSTAR Ion thrUSTER WITH Various Models

The two types of models were presented in the previous chapters. One modeled the power deposition into the thruster from the plasma. The other model predicted the temperatures in the NSTAR thruster. This model relied on using power deposition values that would result in a good temperature fit.

This chapter presents how the power deposition determined for a temperature fit compares to the power deposition predicted from the analytical model described in Chapter 2. It will also present the temperature results from using the thruster thermal code and the predicted power deposition values. When used in tandem, the thermal code and predicted power deposition values provide a method for analyzing existing thrusters and the effect of changes to a thruster.

5.1 Independent Variables Used for Thruster Test Cases

Three throttling points were used to evaluate the model of power deposition on the NSTAR ion thruster. These throttling points were at 0.5 kW, 1.3 kW, and 2.3 kW. A discharge chamber analytical model was run for each of these throttling points. The corresponding values used as inputs for the discharge chamber are shown in Table 5-1. Since several of these values have a degree of uncertainty, the same method used in Chapter 3 was employed here. The values were estimated and then adjusted until the ion flux to the main keeper and the anode were positive. Most of these parameters should remain fairly constant for a particular ion thruster. However, as can be seen, the values used for the 2.3 kW case varied slightly from the other two cases. It is uncertain why this might be. One thought is that with the change in density and energy of the plasma, the

other factors may also change. For example, with a greater plasma density and neutral density, the volume of the ion production region may expand slightly in the outer regions.

The main and neutralizer cathodes were then modeled using an iterative method and based on the discharge chamber model's prediction of the emission current from the main cathode. For both cathodes, their emission current was determined by the current of electrons flowing through the keeper orifice and the current of electrons impinging on the keeper. The temperature at the base of each cathode was determined with the assistance of the SINDA thermal code. The predicted power deposition was used from the analytical models in SINDA and then SINDA gave the resulting base temperature. SINDA was used since it gave a more complete picture of the thermal environment outside of the cathode and since no temperatures were taken at the base location. Table 5-2 lists the values used for the main and neutralizer cathodes.

Table 5-1 Discharge Chamber Independent Variables

	0.5 kW	1.3 kW	2.3 kW
Discharge Voltage (V)	29.4	26.0	27.2
Keeper Voltage (V)	2.5	3.4	5.4
Discharge Current (A)	4.63	7.34	11.8
Beam Current (A)	0.56	0.984	1.75
Accelerator Grid Current (A)	0.0011	0.036	0.082
Anode Work Function (eV)	4.33	4.33	4.33
Keeper Work Function (eV)	4.25	4.25	4.25
Optics Work Function (eV)	4.5	4.5	4.5
V_{IPR} (m ³)	1.0×10^{-3}	1.0×10^{-3}	1.4×10^{-3}
Neutral Flow Rate (sccm)	9.05	15.6	27.1
Effective Neutral Grid Transparency	0.24	0.24	0.24
Screen Grid Ion Transparency	0.8	0.8	0.8
A_g (m ²)	0.01792	0.01792	0.01792
Anode Fall (V)	1.0	1.0	2.0
Accelerator Grid Fall (V)	150.0	150.0	150.0
Extracted Ion Fraction	0.67	0.67	0.6
Primary Electron Length (m)	1.4	1.4	1.4

Table 5-2 Main and Neutralizer Independent Variables

	0.5 kW	1.3 kW	2.3 kW
--	--------	--------	--------

<u>Main Cathode</u>			
Modeled Cathode Length (cm)	5.08	5.08	5.08
Emission Current (A)	3.95	6.14	9.64
Entrance Temperature (°C)	282.3	303.8	343.8
Tip Flux (°C/m)	0.0	0.0	0.0
Inlet Gas Temperature (°C)	27	77	77
Surrounding Environment Temperature (°C)	427	427	427
<u>Neutralizer</u>			
Modeled Cathode Length (cm)	3.18	3.18	3.18
Emission Current (A)	2.06	2.49	3.22
Neutralizer Keeper Current (A)	1.5	1.5	1.5
Entrance Temperature (°C)	518.8	525.9	536.2
Tip Flux (°C/m)	0.0	0.0	0.0
Inlet Gas Temperature (°C)	127	127	127
Surrounding Environment Temperature (°C)	427	427	427
<u>Both Neutralizer and Main Cathode</u>			
Inner Diameter in the 2.54 cm Insert Region (mm)	3.81	3.81	3.81
Inner Diameter Outside the Insert Region (mm)	5.59	5.59	5.59
Outer Diameter (mm)	6.35	6.35	6.35
Shield Length (cm)	1.9	1.9	1.9
Inner Emissivity	0.3	0.3	0.3
Outer Emissivity	0.2	0.2	0.2
Conductivity (W/m °C)	90.0	90.0	90.0
Stanton Number	1.84	1.84	1.84
Convection Coefficient (W/m ² °C)	5.95	5.95	5.95
Ohmic Heating (W/m ²)	100.0	100.0	100.0
Emissivity of Environment	0.2	0.2	0.2
Cathode Work Function (eV)	2.0	2.0	2.0

5.2 Comparison of Results

5.2.1 Discharge Chamber Particle Parameters

In order for currents and power deposition to the thruster to be determined, several other parameters are also derived. Table 5-3 lists some of these parameters. The densities in this ring-cusped ion thruster have been found to be in the 10^{18} - 10^{19} m^{-3} for the neutrals and 10^{17} m^{-3} range for the ion and electron density [41]. The densities predicted by the model fall in this range. The change in the neutral density parameter also explains why different extracted ion fractions were needed for the different cases. Brophy showed that for his thruster the f_B 's dropped by one-tenth as the neutral density parameter increased to 0.2 from about 0.05 [41]. The Maxwellian electron temperatures are expected to range from 1-10 eV. The temperatures determined here also follow the trend which Brophy found and predicted [41]. The primary electron energies varied due to a change in discharge voltage and keeper voltage.

Table 5-3 Predicted Discharge Chamber Particle Parameters

	0.5 kW	1.3 kW	2.3 kW
Maxwellian Electron Temperature (eV)	3.8	3.2	2.5
MDOT(1- η) (A)	0.0897	0.136	0.195
Primary Electron Energy (eV)	29.2	25.3	26.5
Screen Fall (V)	30.4	27	29.2
<u>Densities</u>			
Neutrals (m^{-3})	3.28E+18	4.96E+18	7.14E+18
Maxwellian Electrons (m^{-3})	2.30E+17	4.47E+17	9.20E+17
Primary Electrons (m^{-3})	1.26E+16	1.95E+16	1.85E+16
Total Ion (m^{-3})	2.43E+17	4.66E+17	9.38E+17

5.2.2 Analytical Prediction of Particle Currents and Power Depositions

The main result of the analytical model is to use measured and predicted currents and voltages to determine the power deposited into the thruster. As mentioned, the

cathode results were determined through an iterative technique and from the emission current specified by the discharge chamber model. Table 5-4 and Table 5-5 contain the currents and power deposition for the main and neutralizer cathodes.

The emission current for the cathodes is determined from the electrons leaving the cathode surface thermionically and ionic recombination, with a few energetic electrons making it back to the surface. The power deposition is determined by the heating from the ions and energetic electrons and the cooling of the thermionic electrons. The amount of heating necessary to sustain the thermionic emission is highly dependent on how thermally efficient the cathodes are. It is interesting that the net cathode heating changes only about 1 W for all three cases while the individual heating and cooling components change by up to an order of magnitude more. The different power deposition values between the main cathode with 3.96 A emission and the neutralizer cathode with an emission current of 3.26 A is reflective of the different thermal environments each cathode is in. The main cathode is in the hotter discharge chamber and the neutralizer cathode is in the cooler outer environment.

Table 5-4 Main Cathode Particle Currents and Powers

	0.5 kW	1.3 kW	2.3 kW
Ion Current (A)	1.21	1.43	1.78
Thermionic Electron Current (A)	2.80	4.77	7.92
Energetic Electron Current (A)	0.05	0.06	0.07
Emission Current (net) (A)	3.96	6.14	9.63
Ion and Electron Heating (W)	25.4	30.1	37.5
Thermionic Cooling (W)	6.2	10.6	17.6
Net Cathode Heating (W)	19.2	19.5	19.9

Table 5-5 Neutralizer Cathode Particle Currents and Powers

	0.5 kW	1.3 kW	2.3 kW
Ion Current (A)	1.11	1.18	1.28
Thermionic Electron Current (A)	0.96	1.36	2.03
Energetic Electron Current (A)	0.04	0.05	0.05
Emission Current (net) (A)	2.03	2.49	3.26

Ion and Electron Heating (W)	23.3	24.9	27.0
Thermionic Cooling (W)	2.1	3.0	4.5
Net Cathode Heating (W)	21.2	21.9	22.5

Table 5-6 Predicted Discharge Chamber Currents and Power Depositions

<u>Currents</u>	0.5 kW	1.3 kW	2.3 kW
Total Ion Current Produced (A)	0.84	1.47	2.92
Electrons Emitted through Main Keeper (A)	3.85	5.95	8.95
Discharge Current (A)	4.63	7.34	11.8
Ion Current To Anode (A)	0.06	0.08	0.07
Maxwellian Electron Current To Anode (A)	1.94	3.79	7.52
Primary Electron Current To Anode (A)	2.75	3.62	4.35
Ion Current To Screen Grid (A)	0.14	0.25	0.44
Ion Current To Accelerator Grid (A)	0.001	0.04	0.08
Ion Current To Keeper (A)	0.08	0.16	0.66
Electron Current To Keeper (A)	0.1	0.19	0.68
<u>Power</u>			
to Anode from Primary electrons(W)	91.92	107.47	134.04
to Anode from Maxwellian electrons (W)	27.05	46.77	80.29
to Anode from ions (W)	0.57	0.72	0.75
to Screen Grid from ions (W)	5.46	8.72	16.39
To Accelerator Grid from ions (W)	0.17	5.7	12.98
to Cathode Keeper from ions (W)	2.92	5.55	23.03
to Cathode Keeper from electrons (W)	0.7	1.41	6.56

Table 5-6 contains the predicted currents and power depositions for the discharge chamber. The emitted current from the cathode is equal to the current of electrons emitted through the keeper and the electron current to the keeper. Therefore, the primary electrons available are less than those emitted from the cathode.

The greatest power deposition is from the primary electrons to the anode. There are 2.75-4.35 A of these energetic primary electrons being collected by the anode. The ions contribute only a small amount to the heating of the anode. However, there is an inverse relationship between the ion current to the keeper and to the anode in the region where both are predicted to be positive in the analysis (i.e. Figure 3.14). Chapter 3 explored this relationship further. The power from the ion current to the keeper changed much faster than the ion current to the anode. The peak possible for the power from the

ions to the anode is on the order of a 7 W, while the peak possible for the power from the ions to the keeper is on the order of 25 W for the 2.3 kW case. The values picked favoring the keeper peak were used in the 2.3 kW case since the main keeper temperatures using these predicted power deposition values in SINDA were 20+ °C lower than the experimental main keeper temperatures.

At lower throttling points there is not much heating of the accelerator grid. However, as the throttling points increase, the power to the accelerator grid increases dramatically. The ions that impact the accelerator grid are very energetic, so for very small current changes a substantial increase in heating occurs.

5.2.3 Comparison between SINDA model and Analytical Prediction

SINDA was used in Chapter 4 to model the NSTAR thermal characteristics. Table 5-7 lists the SINDA power deposition results for a temperature fit to experimental data along with the power deposition predicted from the analytical model. The total power deposited to the thruster varies within 6% for all the cases examined. The most noticeable difference between the analytical predictions and SINDA is in the cathode tip. However, the neutralizer cathode and keeper power depositions are all within 2 W except for the lowest throttling point case.

Figure 5.1-Figure 5.2 show the temperatures from the experiment and the SINDA model prediction based on the analytically derived power depositions and the power depositions derived for a temperature fit. As mentioned, the neutralizer keeper power deposition adjusted for a temperature fit is significantly higher than the analytically predicted value. However, if the neutralizer experimental temperatures were evaluated for all three cases, the 1.3 kW and 2.3 kW neutralizer temperatures are very similar, while the 0.5 kW neutralizer tip temperature is 30 °C higher than the other two cases. Table 5-2 shows that the neutralizer emission current drops for the lower throttling points and the

current to the neutralizer keeper remains the same. Since the voltages remain constant, it is not consistent that the lower throttling point has a temperature higher than the other cases. Further investigation of other experimental data not presented here suggests that this temperature is an anomaly of this experiment. This data supports that the temperatures are not much different.

The temperatures for the 0.5 kW and 1.3 kW cases in Figure 5.1 and Figure 5.2 show a good temperature fit for the analytical power deposition predictions. The main cathode keeper is significantly hotter on the analytically predicted 0.5 kW throttling case than the experiment. The analytically predicted temperatures for the 2.3 kW case are generally less than the experimental temperatures, but within 5-10 °C of the purely SINDA derived model. The main cathode keeper is about 20 °C too cool in the analytically predicted model. The main cathode keeper has a large temperature gradient and the SINDA model treats this surface as only a few constant temperature surfaces. It would require further modeling to address these temperature differences in more detail. The neutralizer cathode shows a good fit for the predicted power deposition values.

Table 5-7 Comparisons of Power Deposition Based on SINDA Model and Analytical Predictions

		0.5 kW $I_B = 0.56$ A		1.3 kW $I_B = 0.98$ A		2.3 kW $I_B = 1.75$ A	
Nodes	Description	SINDA Power (W)	Analytic Power (W)	SINDA Power (W)	Analytic Power (W)	SINDA Power (W)	Analytic Power (W)
13	Cathode Tip	13.9	19.2	18.0	19.6	20.0	20.0

201-4	Discharge Chamber , rear	20.0	25.1	33.0	33.0	42.0	38.0
205-8	Anode,rear	48.0	44.0	44.0	42.0	50.0	50.0
209-12	Anode,Middle	18.0	18.0	38.0	38.0	72.0	64.0
221-24	Anode Front, (near grids)	32.4	32.4	46.0	42.0	72.0	64.0
309	Screen Grid	5.5	5.46	8.7	8.72	16.4	16.4
310	Acclerator Grid	0.2	0.17	0.6	0.57	1.3	1.3
403	Neutralizer Tip	21.2	21.2	21.9	21.9	22.6	22.6
404	Neutralizer Keeper	19.0	13.0	15.0	13.0	13.7	13.0
501-4	Keeper	3.6	3.62	7.0	6.96	29.6	29.6
Total		181.8	182.15	232.2	225.75	339.6	318.9

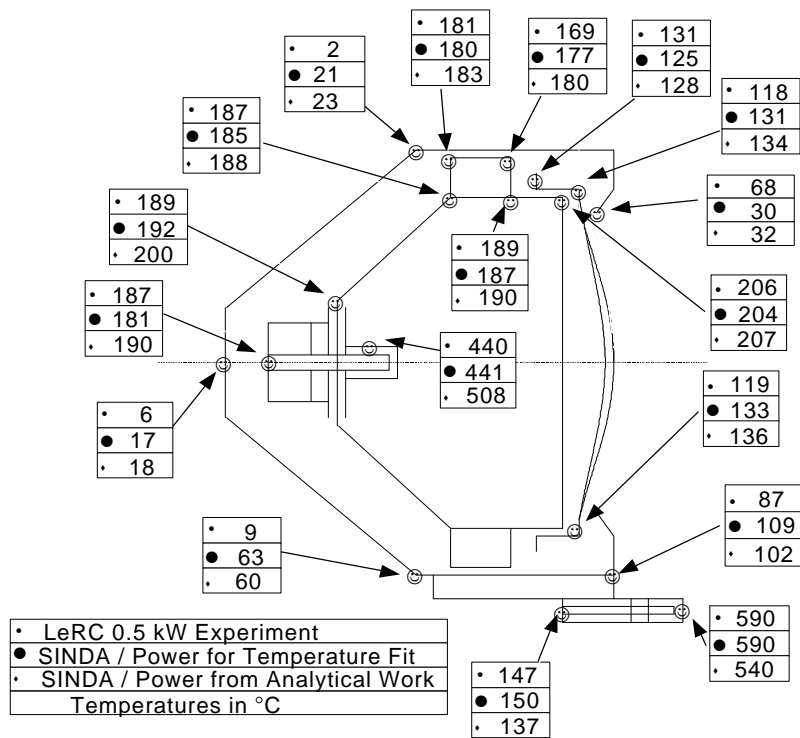


Figure 5.1. NSTAR Thruster Steady State Temperatures for Throttling at 0.5 kW

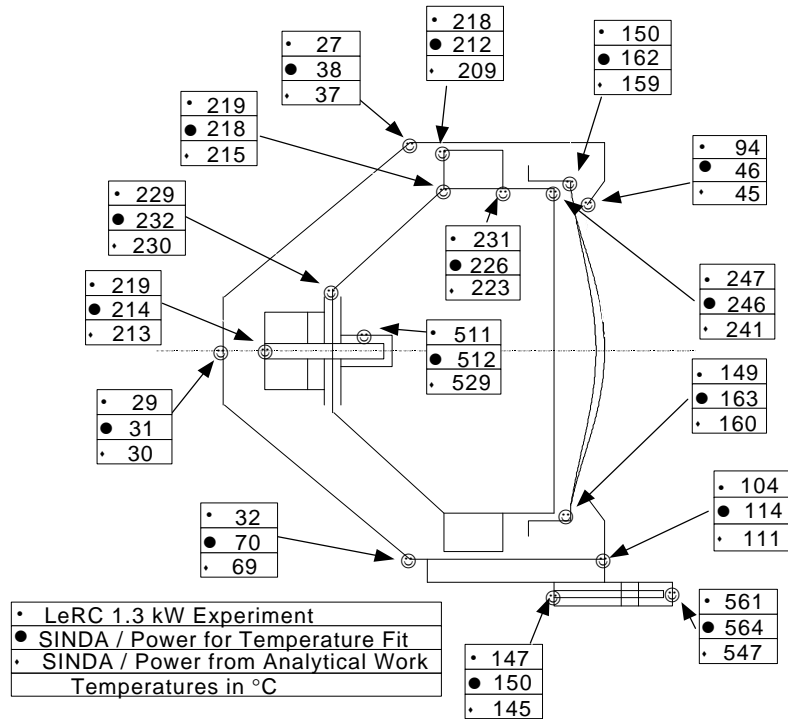


Figure 5.2. NSTAR Thruster Steady State Temperatures for Throttling at 1.3 kW

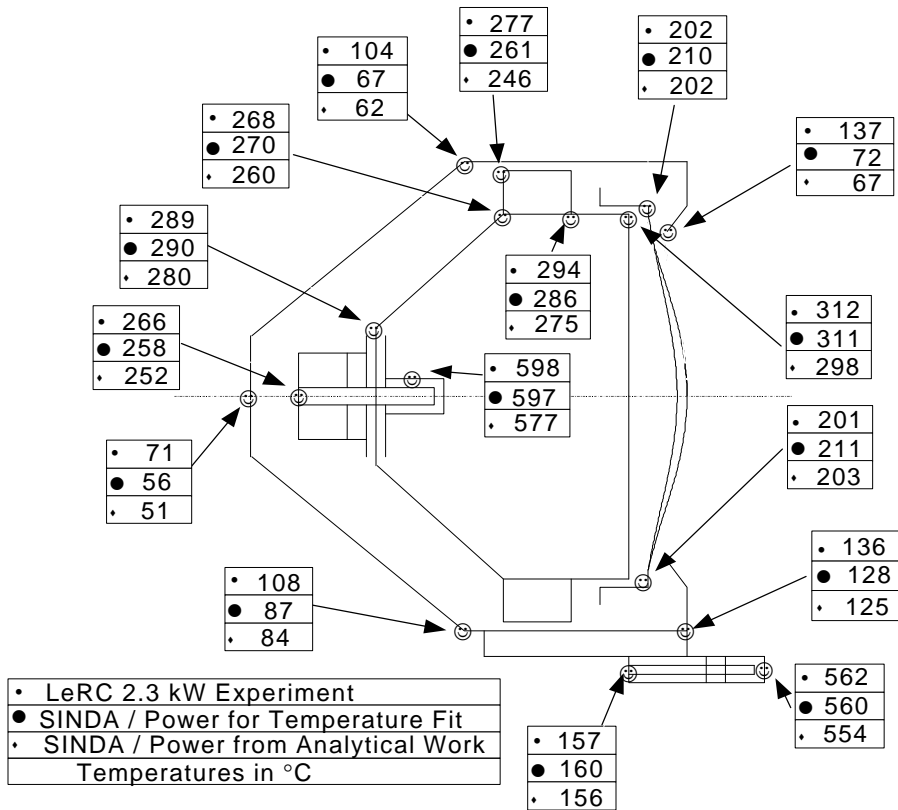


Figure 5.3. NSTAR Thruster Steady State Temperatures for Throttling at 2.3 kW

5.2.4 Temperature Profiles Predicted from Analytical Model

Figure 5.4 and Figure 5.5 show the temperature profile predicted by the analytical model for the main and neutralizer cathode. The base temperatures were estimated using SINDA. The temperatures depicted are along the insert region and inner wall of the cathodes. The change in slope occurs where the insert region ends. These hollow cathodes usually operate in the peak temperature range of 900-1200 °C [28, 29, 64]. Both the main and neutralizer cathode predictions presented here fall within that range.

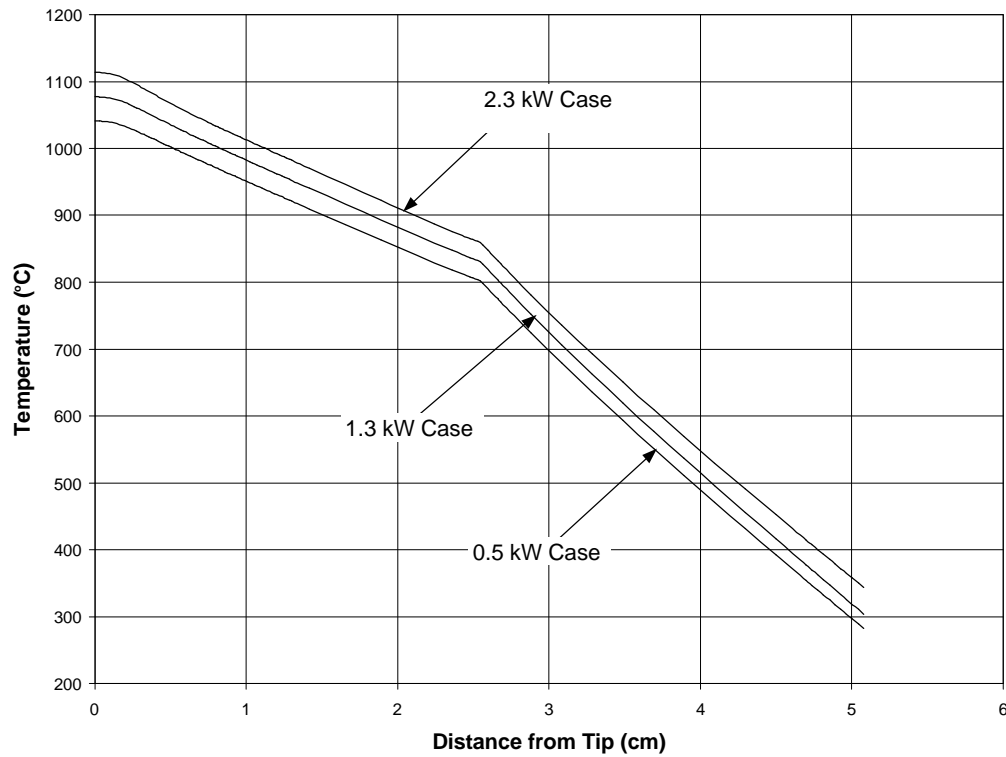


Figure 5.4. NSTAR Main Cathode Temperatures Predicted from Analytical Model

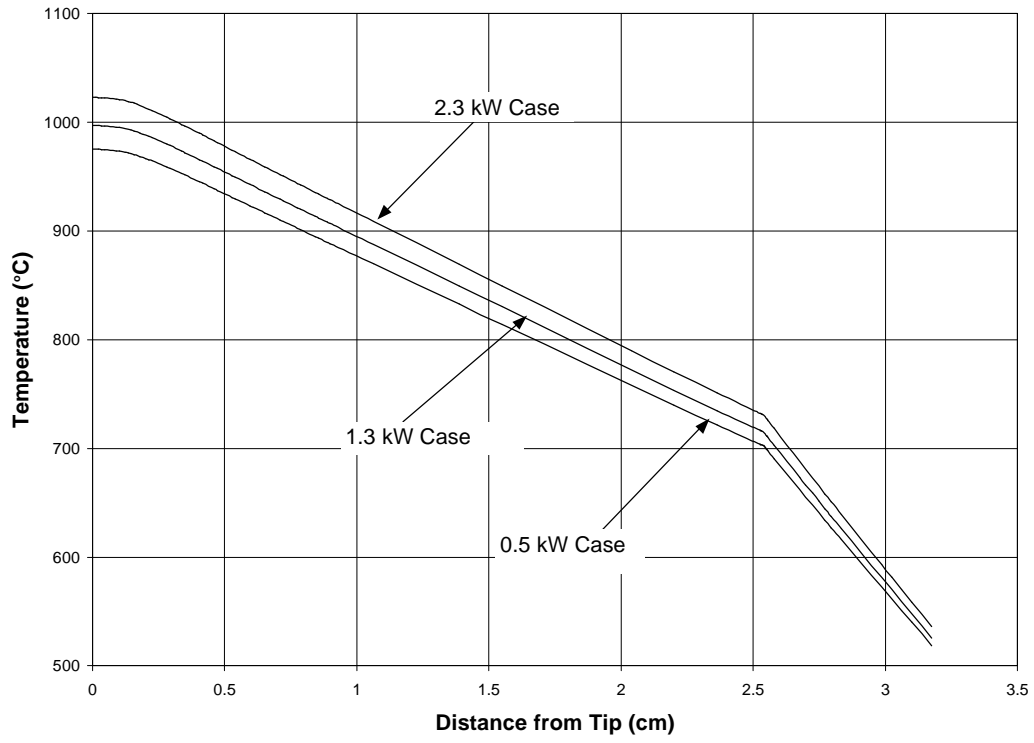


Figure 5.5. NSTAR Neutralizer Cathode Temperatures Predicted from Analytical Model

CHAPTER VI

CONCLUSION and future work recommendations

6.1 Conclusion

A thermal model of an ion thruster was developed in this dissertation. This model consisted of two parts. One part of the model developed the equations and relationships needed to predict the power deposition into the ion thruster from the plasma. The second part used the thermal codes SINDA and TRASYS to predict the temperatures of the NSTAR ion thruster. The thermal codes were able to predict the temperatures in the discharge chamber region to within 10 °C for many different operation conditions.

The power deposited on the ion thruster can be divided into two areas: the cathodes and the discharge chamber region. For the cathodes, a heat transfer equation was developed that took into account gray body radiation heat transfer, conduction heat transfer, convection heat transfer, ohmic heating of the cathode wall from the emission current, cooling from field-enhanced thermionic emission, heating from ionic recombination, and heating from backstreaming energetic electrons. The temperature profile of the cathode, the emission current and the net power deposited were determined from the specified thermophysical characteristics of the cathode and internal plasma characteristics.

A sensitivity study was done using the cathode model with comparisons to previous experiments. This was due in part because of the uncertainty of many values. It was also used to determine the effect of changing many cathode parameters. The work function of the insert had the most significant effect on the temperature profiles and power deposited. Changes of one-tenth of an eV could change the tip temperature by 50 °C and

about 2 watts. Results using reasonable cathode parameters showed good correlation to experimental data. Surprisingly, the model predicted only a small change in net cathode heating of each cathode (less than 6% or about a watt) for different emission currents. The main driver for determining the power to the cathode is the thermal efficiency. The better insulated (both conductively and radiatively) a cathode is, the better it should perform. Currently, around 20 W is lost in heating the cathode.

The other area where a significant amount of power deposition occurs is in the discharge chamber. The power deposition in the discharge chamber region was found using known voltages and currents from experiments, and by predicting plasma parameters and the unknown voltages and currents (such as the primary electron current to the anode, ions produced by primary electrons, or potential fall experienced by accelerator grid ions). The plasma parameters were based on a thruster performance model and the currents were found using continuity. However, several parameters from the performance model have not been published for the NSTAR thruster and have not been determined for other thrusters. These include the volume of the ion production region, the primary electron containment length, and the extracted ion fraction.

Similar to the cathode, a sensitivity study was done on these and other discharge chamber parameters to understand their effect on the power deposition. The driving factor that established the range of acceptable power deposition values was determined by a simultaneous positive ion current to the anode and main keeper. When the currents and power deposition values were compared to the previous work on the Culham thruster, the predicted values fall within most of the error bars previously set. However, it was determined that the primary electrons play a significant role in heating the anode. This comparison also demonstrated the model's ability to analyze a different thruster configuration with a different propellant.

The other part of the model presented here used the thermal codes SINDA and TRASYS. TRASYS predicted shape factors used for radiation heat transfer and SINDA

accomplished the heat transfer model including conduction and radiation heat transfer. This analysis was done on a NASA NSTAR ion thruster. Initially the power deposition values were adjusted from values used on previous thrusters. This gave a temperature fit to experiment of 10 °C for the discharge chamber region. However, there was much difficulty in modeling perforated surfaces and contact resistances. This led to temperatures of perforated surfaces varying greater from the experimental values. To handle the perforated surfaces, they were modeled using transmissive surfaces and checkerboard-type surfaces. These allowed the influence of the environment to remain accurate on the discharge chamber. This model could also be used to determine the influence of changing various components on the thruster.

This thermal model was also used to determine the feasibility of the power deposition model. The total power deposited predicted by the analytical model varied only within 6% of the total power used to attain a temperature fit to experiment. The overall thermal model provides a means for predicting the power deposition and temperatures of an ion thruster.

6.2 Future Work Recommendations

In the cathode model, it was seen that most of the significant plasma interaction is in the first few millimeters near the tip of the cathode. Unfortunately, this region is among the most difficult to characterize experimentally and little is known about the plasma in this region. It would be important to design experiments to document the plasma characteristics in that region. The cathode modeling could also examine different velocity profiles that might exist [79]; however, this should have minimal impact on the results from the cathode model presented here.

With the discharge chamber model, further work needs to be done on local particle fluxes. For example, the anode has electrons that impact it, but their location is estimated

by the intersection of magnetic field lines. Therefore, a majority of the electrons impact near the magnets. However, there is little published data to indicate how much current each magnet region acquires. Some work has begun recently on an 8 cm diameter ion thruster [80]. The same type of experimental survey could indicate the ion flux to the various surfaces also.

Further work also needs to be done to determine how to predict the extracted ion fraction, volume of the ion production region and primary electron containment length. This work could also be aided by knowing how the local plasma parameters relate to the global parameters.

The SINDA model could be improved by a better modeling technique of perforated surfaces and contact resistance. There is not much information currently available for modeling perforated surfaces and these type of surfaces are on a significant number of spacecrafts.

There are a few suggestions that might help improve the hollow cathode design. More effort to minimize heat loss around the insert should help the cathode; therefore, insulating the insert better both conductively and radiatively should be advantageous. It might also be beneficial to extend the radiation shield to cover more of the cathode tube. The insert region could also be minimized since only the first few millimeters are significant. It might be beneficial to create an insert “ring” near the tip of the cathode. This could be the part of the insert near the tip with an inner diameter close in size to the orifice diameter. This could take advantage of the electric field enhancement on thermionic emission.

One possible increase in discharge chamber efficiency would be to choose a lower work function material where the electrons are collected on the anode. The work function of the material plays a dramatic effect with Maxwellian electrons. Also, if there was any way to reduce the amount of primary electrons impacting the surface, there would be a dramatic decrease in power deposited.

However, the power loss could be minimized in a reverse fashion for surfaces that receive a predominant ion flux. When an ion contacts a surface and takes an electron to neutralize it, it deposits considerable energy into the surface, but the electron leaving the surface is a cooling factor (see Equation 2.38). Therefore, increasing the work function of the surfaces that collect ions predominantly increases the amount of energy it takes to extract the electron and the net result is less energy deposited to that surface.

BIBLIOGRAPHY

- [1] Stuhlinger, E., *Ion Propulsion For Spaceflight*, McGraw-Hill Book Co., New York, NY, 1964, p. vii.
- [2] Goddard, R. H., "R. H. Goddard: an Autobiography," Robert H. Goddard Notebook dated September 6, 1906, *Astronautics*, vol. 4, p. 24, 1959.
- [3] Sankovic, J. M., Hamley, J. A., Haag, T. W., Sarmiento, C. J., Curran, F. M., "Hydrogen Arcjet Technology," IEPC-91-018, 22nd International Electric Propulsion Conference, Viareggio, Italy, October 1991.
- [4] Welker, D., "Overview of Electric Propulsion Devices and Power Systems," NASA Glen Research Center Electric Propulsion Homepage, Donald.S.Welker@grc.nasa.gov, <http://trajectory.lerc.nasa.gov>, Mar. 15, 1999.
- [5] Frisbee, R. H., Blandino, J. J., Sercel, J. C., Sargent, M. G., Gowda, N., "Advanced Propulsion Options for the Mars Cargo Mission," AIAA 90-1997, 26th Joint Propulsion Conference, Orlando, FL, July 1990.
- [6] Patterson, M. J., Oleson, S. R., "Low-Power Ion Propulsion for Small Spacecraft," AIAA 97-3060, 33rd Joint Propulsion Conference, Seattle, WA, July 1997.
- [7] Brophy, J. R., "Advanced Ion Propulsion Technology for Solar System Exploration," AIAA 97-2782, 33rd Joint Propulsion Conference, Seattle, WA, July 1997.
- [8] Rudolph, L. K., King, D. Q., "Electromagnetic Thrusters for Spacecraft Prime Propulsion," AIAA 84-1446, 20th Joint Propulsion Conference, Cincinnati, OH, June 1984.
- [9] Tverdokhlebov, S. O., "Study of Double-Stage Anode Layer Thruster Using Inert Gases," IEPC-93-232, 23rd International Electric Propulsion Conference, Seattle, WA, September 1993.
- [10] Oleson, S. R., Myers, R. M., Kluever, C., Riehl, J. P., Curran, F. M., "Advanced Propulsion for Geostationary Orbit Insertion and North-South Station Keeping," AIAA 95-2513, 31st Joint Propulsion Conference, San Diego, CA, July 1995.
- [11] Gray, H., Smith, P., Fearn, D. G., "Design and Development of the UK-10 Ion Propulsion System," AIAA 96-3084, 32nd Joint Propulsion Conference, Lake Buena Vista, FL, July 1996.

-
- [12] Fearn, D. G., Mundy, D. H., "Orbital Control of the Gravity Explorer Spacecraft: the Ion Propulsion Option," AIAA 97-2781, 33rd Joint Propulsion Conference, Seattle, WA, July 1997.
- [13] Matticari, G., Noci, G., Perrotta, G., Sabbagh, J., "Present and In Perspective Applications of Low Thrust Ion Propulsion on Small Satellites," AIAA 95-2510, 31st Joint Propulsion Conference, San Diego, CA, July 1995.
- [14] Polk, J.E., Anderson, J.R., Brophy, J. R., Rawlin, V. K., Patterson, M. J., Sovey, J. S., "The Effect of Engine Wear on Performance in the NSTAR 8000 Hour Ion Engine Endurance Test," AIAA Paper 97-3387, 33rd Joint Propulsion Conference, Seattle, WA, July 1997.
- [15] Leifer, S. D., Anderson, J. R., Anderson, M. S., Mueller, J., Goodwin, D. G., "Developments in Fullerene Ion Propulsion Research," AIAA 94-3241, 30th Joint Propulsion Conference, Indianapolis, IN, June 1994.
- [16] Clark, K. E., "Survey of Electric Propulsion Capability," *Journal of Spacecraft and Rockets*, Vol. 12, No. 11, Nov. 1975, pp. 641-654.
- [17] Kaufman, H. R., "Technology of Electron-Bombardment Ion Thrusters," *Advances in Electronics and Electron Physics*, Vol. 36, Academic Press, Inc., New York, 1974, pp. 265-373.
- [18] Gatsonis, N.A., Samanta Roy, R.I., and Hastings, D.E., "Numerical Investigation of Ion Thruster Plume BackFlow," AIAA Paper 94-3140, June 1994.
- [19] Lide, D.R., "CRC Handbook of Chemistry and Physics," 71st ed., CRC Press Inc., Boca Raton, 1990, p4-37.
- [20] MacRae, G.S., Zavesky, R.J., Gooder, S.T., "Structural and Thermal Response of 30-cm Diameter Ion Thruster Optics," AIAA Paper 89-2719, 25th Joint Propulsion Conference, Monterey, CA, July 1989.
- [21] Wen, L., Crotty, J. D., Pawlik, E. V., "Ion Thruster Thermal Characteristics and Performance," *Journal of Spacecraft and Rockets*, Vol 10, No. 1, Jan. 1973., pp 35-41.
- [22] Oglebay, J. C., "Thermal Analytic Model of a 30 cm Engineering Model Mercury Ion Thruster," *NASA Technical Memorandum*, NASA TM X-71680, March 1975.
- [23] Van Noord, J. L., Gallimore, A. D., Rawlin, V., "Numerical Thermal Model of a 30-cm NSTAR Ion Thruster," IEPC 97-185, 25th International Electric Propulsion Conference, Cleveland, OH, August 1997.

-
- [24] Rawlin, V., Patterson, M., Becker, R., "Thermal Environment Testing of NSTAR Engineering Model Ion Thrusters," IEPC paper 97-051, August 1997.
- [25] Mirtich, M. J., "The Effects of Exposure to LN₂ Temperatures and 2.5 Suns Solar Radiation on 30-cm Ion Thruster Performance," *NASA Technical Memorandum*, NASA TM X-71652, March 1975.
- [26] Mirtich, M. J., "Thermal-Environment Testing of a 30-cm Engineering Model Thruster," *NASA Technical Memorandum*, NASA TM X-73522, Nov. 1976.
- [27] Bechtel, R. T., Dulgeroff, C. R., "J Series Thruster Thermal Test Results," AIAA 82-1906, *16th International Electric Propulsion Conference*, New Orleans, LA, Nov. 1982.
- [28] Domonkos, M.T., Gallimore, A.D., Patterson, M.J., "Thermographic Investigation of 3.2-mm-diameter Orificed Hollow Cathodes," AIAA 98-3798, *34th Joint Propulsion Conference*, Cleveland, OH, July 1998.
- [29] Salhi, A., Theoretical and Experimental Studies of Orificed, Hollow Cathode Operation, Ph. D. Dissertation, Ohio State University, 1993.
- [30] Siegfried, D.E., Wilbur, P.J., "Studies on an Experimental Quartz Tube Hollow Cathode," AIAA 79-2056, *Princeton/AIAA/DGLR 14th International Electric Propulsion Conference*, Princeton, N.J., Oct.-Nov. 1979.
- [31] Capacci, M., Minucci, M., Severi, A., "Simple Numerical Model Describing Discharge Parameters in Orificed Hollow Cathode Devices," AIAA 97-2791, *33rd Joint Propulsion Conference*, Seattle, WA, July 1997.
- [32] Mirtich, M.J., Kerslake, W.R., "Long Lifetime Hollow Cathodes for 30-cm Mercury Ion Thrusters," AIAA 76-985, *AIAA International Electric Propulsion Conference*, Key Biscayne FF, Nov. 1976.
- [33] Wilbur, P.J., Siegfried, D. E., "Advanced Ion Thruster Research," *NASA Contractor Report*, NASA CR-168340, Jan. 1984, pp 127ff.
- [34] Siegel, R., Keshock, E.G., "Wall Temperatures in a Tube with Forced Convection, Internal Radiation Exchange, and Axial Wall Heat Conduction," *NASA Technical Notes*, NASA TN D-2116, March 1964.
- [35] Siegel, R., Howell, J. R., *Thermal Radiation Heat Transfer*, Hemisphere Publishing Corp., Washington D.C., 1992.

-
- [36] Siegel, R., Perlmutter, M., "Convective and Radiant Heat Transfer for Flow of a Transparent Gas in a Tube with a Gray Wall," *Int. J. Heat Mass Transfer*, Vol. 5, 1962, pp.639-660.
- [37] Mehta, R.C., Kumar, P., "Numerical Analysis of a Tube with Heat Generation, Thermal Radiation, Convection and Axial Conduction," *Int. J. Heat Mass Transfer*, Vol. 28, No. 11, 1985, pp. 2169-2171.
- [38] Wells, A. A., Harrison, M. F. A., Eden, M. J., "Experimental Studies of Ion Extraction, Ion Loss and Energy Balance in a SERT II Type Ion Thruster," AIAA 70-1091, 8th *Electric Propulsion Conference*, Stanford, CA, Aug. 1970.
- [39] Masek, T. D., "Plasma Properties and Performance of Mercury Ion Thrusters," *AIAA Journal*, Vol. 9, No. 2, Feb. 1971, pp. 205-212.
- [40] Masek, T. D., "Plasma Properties and Performance of Mercury Ion Thrusters," AIAA 69-256, 7th *Electric Propulsion Conference*, Williamsburg, VA, March 1969.
- [41] Brophy, J.R., and Wilbur, P. J., *Ion Thruster Performance Model*, Ph.D. Dissertation, Colorado State Univ., Fort Collins, CO, also NASA CR-174810, Dec. 1984.
- [42] Polk, J. E., Brophy, J. R., Wang, J., "Spatial and Temporal Distribution of Ion Engine Accelerator Grid Erosion," AIAA 95-2924, 31st *Joint Propulsion Conference*, San Diego, CA, July 1995.
- [43] Rawlin, V. K., Banks, B. A., Byers, D. C., "Dished Accelerator Grids on a 30-cm Ion Thruster," *Journal of Spacecraft and Rockets*, Vol. 10, No. 1, Jan. 1973, pp. 29-35.
- [44] Brophy, J. R., Mueller, J., Brown, D. K., "Carbon-Carbon Ion Engine Grids with Non-Circular Apertures," AIAA 95-2662, 31st *Joint Propulsion Conference*, San Diego, CA, July 1995.
- [45] Mueller, J., Brophy, J. R., Brown, D. K., "Endurance Testing and Fabrication of Advanced 15-cm and 30-cm Carbon-Carbon Composite Grids," AIAA 95-2660, 31st *Joint Propulsion Conference*, San Diego, CA, July 1995.
- [46] Monheiser, J. M., *Development and Verification of a Model to Predict Impingement Currents for Ion Thrusters*, Ph. D. Dissertation, Colorado State Univ., Fort Collins, CO, also NASA CR-195322, April 1994.

-
- [47] Krall, N.A., Trivelpiece, A.W., *Principles of Plasma Physics*, McGraw-Hill Book Co., New York, NY, 1973, pp 24-25.
- [48] Huba, J.D. *Naval Research Laboratory Plasma Formulary*, Naval Research Laboratory, Washington, DC, Revised 1998.
- [49] Incropera, F.P., DeWitt, D.P., *Fundamentals of Heat and Mass Transfer*, John Wiley & Sons, New York, NY, 1990.
- [50] Goldstein, R., Pawlik, E.V., Wen, L., "Preliminary Investigation of Ion Thruster Cathodes," *NASA Technical Report*, NASA TR 32-1536, Aug. 1971
- [51] Fomenko, V.S., Samsonov, G.V., *HANDBOOK OF THERMIONIC PROPERTIES - Electronic Work Functions and Richardson Constants of Elements and Compounds*, Plenum Press Division, New York, NY, 1966, pp 53-56.
- [52] Goodfellow, K.D., *A Theoretical and Experimental Investigation of Cathode Processes in Electric Thrusters*, Ph. D. Dissertation, University of Southern California, May 1996, pp27-28.
- [53] Wagener, P.S., Herrmann, I.G., *The Oxide-Coated Cathode*, Vol. 2, Chapman & Hall Ltd., London, England, 1951, p77.
- [54] Ecker, G., "Electrode Components of the Arc Discharge," *Springer Tracts in Modern Physics*, (Ergebnisse der Exakten Naturwissenschaften), 1961, pp 1-104.
- [55] Gallimore, A.D., *Anode Power Deposition in Co-axial MPD Thrusters*, Ph. D. Dissertation, MAE Dept., Princeton University, Oct 1992.
- [56] Myers, R.M., *Energy Deposition in Low Power Coaxial Plasma Thrusters*, Ph. D. Dissertation, MAE Dept., Princeton University, June 1989.
- [57] Oberth, R.C., *Anode Phenomena in High-Current Discharges*, Ph. D. Dissertation, Department of Aerospace and Mechanical Sciences, Princeton University, Dec. 1970.
- [58] Siegfried, D.E., Wilbur, P.J., "Phenomenological Model Describing Orificed, Hollow Cathode Operation," *AIAA Journal*, Vol. 21, No.1, Jan. 1983.
- [59] Chen, F.F., *Introduction to Plasma Physics and Controlled Fusion Vol. 1 Plasma Physics*, Plenum Press, New York NY, 1984, p296.
- [60] Matossian, J. N., Beattie, J. R., "Model for Computing Volume-Averaged Plasma Properties in Electron-Bombardment Ion Thrusters," *Journal of Propulsion*, Vol. 5, No. 2, March-April 1989.

-
- [61] Vaughn, J. A., *Characterization of Hollow Cathode, Ring Cusp Discharge Chambers*, M. S. Thesis, Colorado State University, Fort Collins, CO, also NASA CR-182255, Jan. 1989.
- [62] Lee, J. F., Sears, F. W., and Turcotte, D. L., *Statistical Thermodynamics*, Addison-Wesley, 1973.
- [63] *Rhenium and Rhenium Alloys*, Information given by Rhenium Alloys, Inc., Elyria, OH.
- [64] Sarver-Verhey, T.R., "Extended-Testing of Xenon Ion Thruster Hollow Cathodes," AIAA-92-3204, also *NASA Contractor Report*, NASA CR-189227, July 1992.
- [65] Nakazaki, S., Berrington, K. A., Eissner, W. B., Itikawa, Y., "Theory and Practice in Low-Energy Electron Excitation of the $5p^56s$ levels of Xenon," *Journal of Physics B: At. Mol. Opt. Phys.*, Vol. 30, 1997, pp. L59-L66.
- [66] Rapp, D. and Englander-Golden, P., "Total Cross Sections for Ionization and Attachment in Gases by Electron Impact. I. Positive Ionization," *Journal of Chemical Physics*, Vol. 34, No. 5, 1965, pp. 1464-1479.
- [67] Hayashi, M., "Determination of Electron-Xenon Total Excitation Cross Section, from Threshold to 100 eV, from Experimental Values of Townsend's α ," *Journal of Physics D: Applied Physics*, Vol. 16, 1983, pp. 581-589.
- [68] Kieffer, L. J., Dunn, G. H., "Electron Impact Ionization Cross-Section Data for Atoms, Atomic Ions, and Diatomic Molecules: I. Experimental Data," *Reviews of Modern Physics*, Vol. 38, No. 1, January 1966, pp. 1-35.
- [69] Walker, D. W., "The Effect of Atomic Distortion on Electron Scattering from Mercury," *Journal of Physics B: Atom. Molec. Phys.*, Vol. 3, 1970, pp. 788-797.
- [70] Beattie, J. R., *Cusped Magnetic Field Mercury Ion Thruster*, Ph. D. Dissertation, Dept. of Mechanical Engineering, Colorado State University, July 1976.
- [71] Beattie, J. R., Matossian, J. N., *Inert-Gas Ion Thruster Technology*, NASA CR-191093, Hughes Research Laboratories, Malibu, CA, March 1993.
- [72] Foster, J., Private Communication, NASA John Glenn Research Center, Cleveland, April 1999.
- [73] Cullimore, B. A., Goble, R. G., Jensen, C. L., Ring, S. G., "Systems Improved Numerical Differencing Analyzer and Fluid Integrator; User's Manual," Contract NAS9-17448, March 1990, Martin Marietta Corporation, Denver, Colorado; also MCR-90-512, 1990, NASA.

-
- [74] Anderson, G. E., Garcia, D., "Thermal Radiation Analyzer System (TRASYS); User's Manual," Contract NAS9-17900, April 1988, Lockheed Engineering and Management Services Company, Houston, Texas; also JSC-22964, 1988, NASA.
- [75] Gilmore, D.G., *Satellite Thermal Control Handbook*, The Aerospace Corporation Press, El Segundo, CA, 1994, pp. 3-14, 5-61 - 5-65.
- [76] Keller, J.R., "Validation of the SINDA/FLUINT Code Using Several Analytical Solutions," *Sixth Annual Thermal and Fluids Analysis Workshop*, NASA Conference Publication 10161, Aug. 1994, pp. 69-84.
- [77] Holman, J.P., *Heat Transfer*, 7th ed., McGraw-Hill, Inc., New York, 1990, pp 666-667.
- [78] Stevens, P., Engineering Support Request # 96171-PS, JPL Pasadena CA, Aug. 1996.
- [79] Domonkos, M. T., *Evaluation of Low Current Orificed Hollow Cathode*, Ph.D. Dissertation, Aerospace Engineering Department, University of Michigan, Ann Arbor, October 1999.
- [80] Foster, J., "Internal Discharge Properties and Enhanced Discharge Performance of a Magnetically Confined DC Plasma Source," NASA TM-1999-209386, NASA John Glenn Research Center, Cleveland, August 1999.